NTNU

Norwegian University of
Science and Technology

Wear of Carbon Refractory Materials in Silicon Furnaces

Sofie Aursjø

Materials Technology
Submission date: June 2016
Supervisor: Merete Tangstad, IMTE
Co-supervisor: Lars Lindstad, Elkem Carbon

Norwegian University of Science and Technology
Department of Materials Science and Engineering

I hereby declare that this work has been carried out independently and in compliance with the examination regulations of the Norwegian University of Science and Technology, NTNU.

Sofie Aursjø
Trondheim, June 2016

Preface

This report describes an investigation of carbon lining wear in silicon producing furnaces, and is the evaluation basis for the course TMT9000 at the Norwegian University of Science and Technology, NTNU.

This work has been a collaboration between the Norwegian University of Science and Technology and Elkem Carbon AS, and both parties have contributed to the project with both guidance and financial support. Most of the work and experiments have been executed at the Department of Materials Science at NTNU, with the exception of sample preparation and characterization tests performed at Elkem Carbon AS, Fiskaa Kristiansand.

I would first of all like to thank my supervisor from NTNU, Professor Merete Tangstad for the opportunity to work with this topic. She has provided much needed and uplifting advice, encouragement and guidance in the last year. I would also like to thank dr.ing. Lars Holger Lindstad at Elkem Carbon AS for much appreciated advice and discussions, which has helped me gain insight into the world of carbon materials.

I am also very grateful to Ole Tore Buset (NTNU) for the help he has given me with the CT scanning, Pål Tetlie for his help with the Entech resistance furnace, Tone Anzjøn (SINTEF) for performing the wettability experiments in the sessile drop furnace and Morten Raanes for performing the electron probe micro-analysis. A special thanks is given to Karin Fjeldstad Jusnes, for being my partner in crime when using the IF-75 furnace.

Finally, I would like to thank all the members of the SiManTi group for both academic advice and a lot of fun in the past year, and last but not least my "material girls" for making the last five years truly unforgettable.

Trondheim, June 2016
Sofie Aursjø

Abstract

The goal of this thesis was to investigate the internal morphology of different types of lining prepared with different installation techniques, and to see how the internal morphology affects the different wear mechanisms of the carbon lining. Part of the thesis was also to evaluate how differences in the experimental setup such as choice of furnace, temperature profile and addition of slag influenced the amount of silicon intrusion into the sample, and to compare the experimental setups with conditions found in industrial furnaces.

Three different types of carbon linings were used, all provided by Elkem Carbon Fiskaa, and each type with a different binder phase. From the three different pastes, four different types of samples were prepared:

- Layered samples using eco binder and addition of silicon particles, with a layer thickness of approximately 2 cm.
- Layered samples using coal tar pitch binder, layer thickness of approximately 6 cm.
- Layered samples using resin binder, layer thickness of approximately 8 cm.
- Fischer-Sandrammer (FS) samples with coal tar pitch binder, produced with a solid, unlayered structure.

After sample preparation, the different samples were investigated using X-ray computed tomography (CT), and from this it was determined that the sample preparation had influenced the internal morphology of the samples. While the solid FS samples showed no significant density variation across the height of the sample, all of the layered samples had increased densities at the top of each layer and decreased density towards the bottom of each layer. This was due to the ramming procedure, which compacted the paste more in the top of the layers and less towards the bottom of the layers. This density variation increased as the layer thickness increased. It was also determined that the ramming tool influenced the amount of grain crushing, as the star shaped ramming tool crushed all the grains in the top 2 mm of each layer while the flat ramming tool left the vast majority of the grains unaffected. Cracks could be detected in all of the samples, but the amounts varied between the different types of binder; the tar pitch binder samples (layered and solid alike) had the most cracks, while the eco binder had fewer and shorter cracks than the tar pitch samples. The resin binder sample hardly contained any cracks.

All samples were exposed to metallurgical grade silicon, while a slag consisting of SiO_2 - Al_2O_3 - CaO was added for five of the experiments. Two different furnaces, induction and resistance heated, were used in the experiments, and the temperature followed three different temperature profiles: heating to 1500°C before holding at this temperature, cycling from 1600°C-1450°C (above the solidification temperature of silicon) and cycling from 1600°C-1350°C (around the solidification temperature of silicon).

CT investigations performed after exposure to silicon showed that the maximum heating rate of the resistance furnace used in the experimental work was way to slow, and that all of the silicon had oxidized before it had time to melt. This was the case even when slag was added to protect the silicon from oxygen in the furnace, and no intrusion could be observed in the samples from the resistance heated furnace.

The CT results also showed that no intrusion occurred in the experiment performed in the induction furnace without temperature cycling. Some intrusion occurred as the temperature was cycled above the solidification temperature, while heavy intrusion occurred in the samples cycled around the solidification temperature.

Investigations using electron probe micro-analysis (EPMA) showed that reaction had occurred as a result of the silicon intrusion, where intruded silicon had reacted with the carbon lining to form silicon carbide, SiC. It also showed that slag had intruded into the outer 0.5-0.6 mm of the sample, but that no reaction between slag and lining seemed to occur. Conversion to SiC was also observed in some of the unintruded samples, and this conversion is assumed to have occurred as a reaction between SiO(g) formed in the furnace during heating, and carbon from the carbon lining.

It was observed that the conversion to silicon carbide could be detrimental for the lining, as strings and pieces of silicon carbide was found in the slag surrounding the surface, detached from the rest of the lining. This means that converted lining could be eaten away by the slag over time, which would alter the lining properties and possibly ruin the lining performance.

Sammendrag

Formålet med dette arbeidet har vært å undersøke den indre strukturen til karbonforingsprøver tillaget med ulik stampemasse, stampeverktøy og lagtykkelse, og å se om forskjeller i indre struktur påvirker slitasje av karbonforingen ved utsettelse for flytende silisium. Det har også blitt foretatt undersøkelser om mengden inntrengt silisium påvirkes av ovnstype, temperaturprofil og tilsats av slagg.

Tre ulike stampemasser fra Elkem Carbon ble brukt i forsøkene, og av disse massene ble det preparert fire ulike typer prøver:

- Lagdelt prøve med ecobinder og tilsats av finmalt silisium, med lagtykkelse på cirka 2 cm.
- Lagdelt prøve med kulltjærebekbinder, med lagtykkelse på cirka 6 cm.
- Lagdelt prøve med resinbinder, med lagtykkelse på cirka 8 cm.
- Fischer-Sandrammer (FS) prøver med en solid struktur uten lagdeling.

Etter prøvepreparering ble alle prøvene scannet ved bruk av computertomografi (CT), og fra disse undersøkelsene ble det bestemt at prøvepreparereingsmetodene hadde påvirket den indre strukturen til de ulike prøvene. FS-prøvene hadde ingen betydelige tetthetsvariasjoner i høyderetning, mens det i alle de lagdelte prøvene ble observert økt tetthet i toppen av stampelagene og redusert tetthet i bunnen av stampelagene. Dette kom både av at stampingen hadde ført til noe opphopning av store korn i bunnen av stampelagene som igjen har ført til porer i dette området, men også av at massen har blitt mer kompaktert i toppen av stampelagene kontra i bunnen. Tetthetsforskjellen mellom topp og bunn av stampelagene økte med økt lagtykkelse. Det ble også observert at stampeverktøyet påvirket prøvens indre, da prøvene stampet med et kantete, stjerneformet stampehode hadde en betydelig mengde knuste korn i de øverste 2 mm av hvert stampelag, mens kornene i prøvene stampet med et flatt stampehode var tilnærmet upåvirkede av stampingen. Sprekker ble funnet i alle prøvene, men sprekkdannelsen synes å variere utifra hvilken binderfase som er blitt brukt; i prøvene med bekbinder (både lagdelt og FS) ble det funnet flere sprekker enn i prøvene med ecobinder. Det ble nesten ikke funnet noen sprekker i prøven med resinbinder.

Alle prøvene ble eksponert for silisium, og en slagg bestående av SiO_2 - Al_2O_3 - CaO ble tilsatt i fem av forsøkene. To ulike ovner, en induksjonsovn og en

motstandsovn, ble brukt i forsøkene, og tre ulike profiler ble brukt for temperaturen: oppvarming til 1500°C+holdetid, sykling av temperaturen fra 1600°C-1450°C (høyere enn størkningspunktet til silisium) og sykling fra 1600°C-1350°C (rundt størkningspunktet til silisium).

CT-undersøkelser som ble foretatt av karbonforingsprøvene etter eksponering for flytende silisium viste at oppvarmingshastigheten i motstandsovnen hadde vært så lav at silisiumet hadde oksidert før det rakk å smelte. Dette var tilfellet også etter tilsats av slagg, og ingen inntrengning av hverken slagg eller silisium kunne observeres i prøvene fra motstandsovnen.

Bildene fra CT viste ingen inntrengning av silisium fra eksperimentet uten temperatursykling i induksjonsovnen. Moderat inntrengning hadde skjedd i prøven som ble syklet høyere enn størkningspunktet til silisium, mens betydelig inntrengning hadde skjedd i prøven syklet rundt størkningspunktet.

Undersøkelser ble foretatt med elektronmikrosonde (EPMA), og det ble da påvist reaksjon mellom det inntrengte silisiumet og karbonforingen, med silisiumkarbid (SiC) som produkt. Undersøkelsene viste også at slagg hadde trengt 0.5-0.6 mm inn i prøven, men at ingen reaksjon kunne påvises mellom foringen og inntrengt slagg. Det ble forøvrig observert at omdannelse av foringen til SiC kunne påvises også i prøvene uten noe silisiuminntrengning, og det ble her antatt at reaksjonen skjedde mellom foringen og SiO(g) som har blitt dannet i ovnen.

Tråder og biter av silisiumkarbid ble funnet i slaggen, totalt løsrevet fra resten av karbonforingen. Dette kan bety at omdannet foring fjernes av slaggen, noe som kan spise vekk store deler av foringen over lengre tid. Dette kan derfor være skadelig for foringen og dens egenskaper.

Contents

Chapter 1

Introduction

Silicon is a highly abundant element with a wide range of applications. Metallurgical grade silicon is used to make silicon resins, seals and oils, for alloying with i.e. steel or aluminium, or could be refined and used in electrical applications such as semiconductors and solar cells. The need for silicon is increasing, and will probably keep this trend in the foreseeable future. Figure 1.1 shows the annual silicon metal consumption by end-use from 2000 to 2013, as well as a prediction made by Roskill in their silicon and ferrosilicon industry markets and outlook report from 2014.

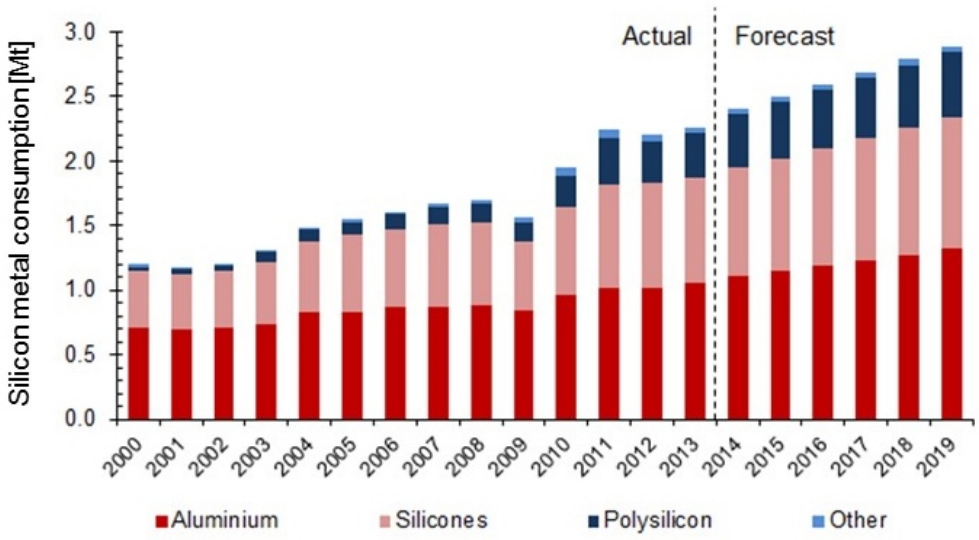

Figure 1.1: Annual silicon metal consumption by end-use from 2000 to 2019, after Roskill[1].

All silicon is produced by reducing oxide raw materials in large submerged arc furnaces, a high temperature process with high energy consumption. Energy for the reduction reactions is supplied into the furnace by the use of carbon based electrodes, and submerged arc furnaces for silicon production are usually designed with three electrodes in a circular furnace. Figure 1.2 shows the partial cross section of a silicon submerged arc furnace.

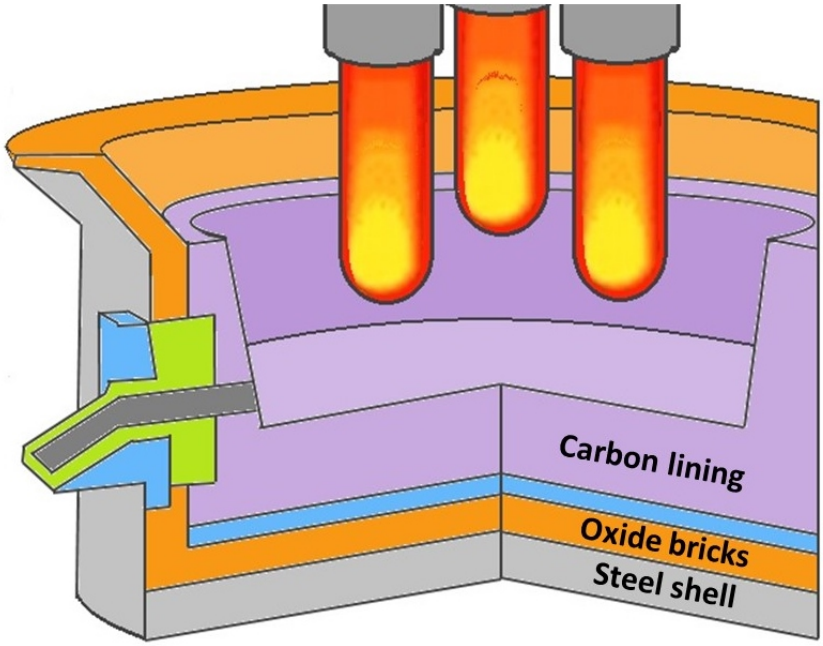

Figure 1.2: Partial cross section of a submerged arc furnace, after SNE research [2].

The furnace wall usually consists of three main structures. The outermost layer is a steel shell. This keeps the furnace structure in place and prevents air from entering the furnace and furnace gases from escaping into the environment, but is unable to withstand very high temperatures. The middle layer consists of refractory bricks made of various oxides, e.g. Al_2O_3, MgO or SiO_2, and is illustrated by the orange layer in figure 1.2. The oxides can withstand the temperatures in the furnace, but are not necessarily chemically resistant towards the furnace content. The innermost layer of the furnace wall is a carbon lining, which is made to withstand high temperatures and wear from the furnace content [3].

One of the factors influencing how long a silicon producing furnace can operate without prolonged shut downs, is the lifespan of the furnace lining. Allthough carbon has been established as the best material both in respect to temperature and wear resistance, it is still subject to wear. Extended wear of the furnace

lining could be detrimental and the worst case scenario is leakage of furnace content from the furnace and bottom breakouts [4]. This could lead to long term shut downs of the furnace, facility damage and endanger personnel. Shut downs give significant costs with respect to repairing/rebuilding the lining, but also in terms of production loss. Wear of the lining should be avoided as much as possible.

* * *

This report is a continuation of the preliminary work performed by Aursjø [5] in the project report *Wear of Carbon Refractory Materials in Silicon Furnaces*, where the purpose was to investigate the internal morphology of carbon linings, as well as the carbon lining wear mechanisms. X-ray computed tomography (CT) was used to analyze the samples, and to induce wear on the lining, the samples were subjected to liquid silicon in an induction furnace.

In the preliminary project work, it was discussed whether the lining installation procedures were affecting the morphology. It was hence decided to investigate how different lining installation procedures could be affecting the carbon lining wear mechanisms in silicon furnaces. For this report, carbon linings with different structure and morpholohy will be investigated both before and after exposure to silicon to determine whether different wear mechanisms depend on the internal morphology of the lining.

For this experimental work, the samples will be exposed to liquid silicon using an electric resistance heated furnace and a sessile drop furnace, as well as further experiments in the induction furnace. Each of these furnaces has factors that might influence the intrusion and wear of the lining. While induction furnaces heat the furnace content quickly and prevents oxidation of the silicon, induction forces might influence the furnace content in unwanted ways. On the other hand, resistance heated furnaces are free of influencing forces, but these furnaces usually work slower than induction furnaces. The sessile drop furnace has the fastest heating rate and does not have forces influencing the furnace content. However, only small samples can be investigated in this furnace, and the use of shielding gas might influence wetting of, and intrusion into, the sample.

In the preliminary work, all samples were heated as quickly as possible to 1600°C and held at this temperature for 30-40 minutes. This only represents part of the conditions furnace linings have to endure, as the temperature might occasionally drop below the solidification temperature of silicon in industrial furnaces. To investigate if the solidification of silicon affects the intrusion and wear, some of the

experiments will be conducted with temperature cycling around the solidification temperature of silicon. In addition, a slag will be added to the silicon in some of the experiments, to determine if slag influence the wear mechanisms. The slag will consist of alumina, lime and silica, which are the most common slag constituents in silicon producing furnaces [6].

* * *

The purpose of this report may be summed up in three main parts;

- Determine whether silicon and/or slag intrudes into carbon linings at elevated temperatures, and investigate whether any intrusion is affected by the internal morphology of the samples.
- See if intrusion of liquid silicon and/or slag leads to chemical reactions between the carbon lining and the intruded elements.
- Investigate if any potential intrusion and/or reaction leads to degradation of the carbon lining, in the form of e.g. spalling or consumption.

The linings used in the experimental work are anthracite based linings provided by Elkem Carbon AS Fiskaa, and the silicon is provided by Elkem Thamshavn. After sample preparation, the samples will be characterized with respect to density, grain crushing and crack distribution using X-ray computed tomography (CT). The samples will, after initial characterization, be heated with MG silicon, and in some experiments slag, from room temperature to 1500-1600°C using different furnaces. Some of the samples will undergo temperature cycling at elevated temperatures. After exposure to silicon, the samples will be scanned in CT again, and the set of scans acquired after the experiments can then be compared with the scans of the pristine samples.

Several tests could be applied to analyze the amount of wear of carbon lining samples, but few are non-destructive. The advantage of using non-destructive testing is the ability to investigate the same set of samples both before and after experiments. This allows investigation of how the morphology influences the experimental results, by comparing the two sets of CT scans. The samples will also be examined in higher magnifications using Electron Probe Micro-Analysis (EPMA), to investigate wetting, intrusion and chemical reactions.

Chapter 2

Theory

The goal of this report is to investigate the internal structure of different carbon linings, and wear of carbon linings when exposed to liquid silicon and slag. To gain an understanding of this, it is important to consider how the silicon production process and furnaces work, how the linings are designed and installed into furnaces, the different mechanisms of lining wear and the properties of both the lining material and the furnace content.

This chapter contains a short introduction to the silicon production process and silicon furnaces, lining design, lining materials and their properties and the properties of the furnace content. It will also look at previous studies on the topic of interactions between silicon or slag and carbon materials, and explain the principles behind the furnaces and lining wear investigation methods chosen for this work.

2.1 Production of silicon

Silicon is produced by reducing oxide raw materials (quartz, SiO_2) in a submerged arc furnace at elevated temperatures. The reducing agent for this process is carbon, mainly in the form of coke, coal, charcoal or woodchips. Both quartz and carbon enter the furnace at the top, while liquid silicon is tapped at the bottom of the furnace. The total reaction for reduction of quartz to silicon is given in equation 2.1.

$$SiO_2(s) + 2C(s) = Si(l) + 2CO(g) \tag{2.1}$$

However, it is common to consider several reactions in the reduction process, taking place in different parts of the furnace. Schei et al. [6] present a model which divides

the furnace into two zones; an inner zone and an outer zone. The inner zone has high temperatures and is where Si and SiO is produced, which occurs according to equation 2.2 and 2.3. In the outer zone, the temperature is significantly lower, and SiO(g) produced in the inner zone is recovered here, according to equation 2.4 - 2.6.

$$\mathrm{SiO(g) + SiC(s) = 2Si(l) + CO(g)} \qquad \Delta H_{1800^\circ C} = 47.5\mathrm{kW/mol} \tag{2.2}$$

$$\mathrm{Si(l) + SiO_2(s) = 2SiO(g)} \qquad \Delta H_{1800^\circ C} = 166\mathrm{kW/mol} \tag{2.3}$$

$$\mathrm{SiO(g) + 2C(s) = SiC(s) + CO(g)} \qquad \Delta H_{1000^\circ C} = -21\mathrm{kW/mol} \tag{2.4}$$

$$\mathrm{3SiO(g) + CO(g) = SiC(s) + 2SiO_2(s)} \qquad \Delta H_{1000^\circ C} = -397\mathrm{kW/mol} \tag{2.5}$$

$$\mathrm{2SiO(g) = Si(l) + SiO_2(s)} \qquad \Delta H_{1000^\circ C} = -189\mathrm{kW/mol} \tag{2.6}$$

Figure 2.1 illustrates the species in the ternary Si-O-C system. In the temperature range 1400-2100°C, the species are in the following state:

- Solid: C, SiC
- Liquid or solid: Si, SiO_2
- Gas: SiO, CO, CO_2, O_2

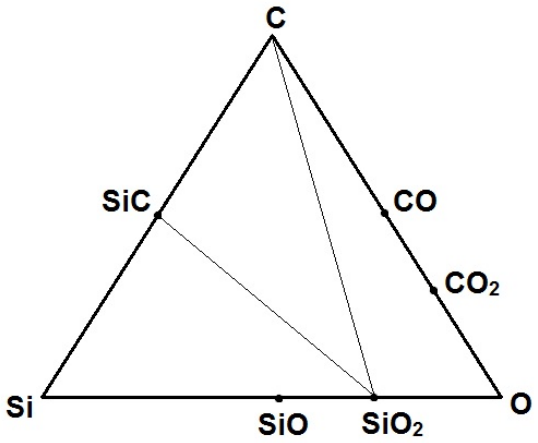

Figure 2.1: Schematic diagram of the phase relations in the Si-O-C system, after Schei et al. [6]

Carbon will always be present in the furnace as a solid. Graphite, which is the stable modification of carbon, sublimates at about 3500°C [6]. SiC is the only stable condensed compound in the system, and remains solid until it decomposes peritectically at 2830°C [7]. The melting temperature of silicon is 1416°C [8], and it could thus be present as both a liquid and a solid in the furnace. SiO_2 is found in the main solid forms of quartz, tridymite and cristobalite, where high temperature cristobalite has a melting point of approximately 1725°C[6].

SiO is stable as a gaseous component at high temperatures, and both CO and CO_2 will be present as gases throughout the system. The ratio between CO and CO_2 depends on which direction the Boudouard reaction, given in equation 2.7, is driven. This depends on the temperature at which the reaction occurs [9]. The Boudouard equilibrium diagram, given in figure 2.2, shows that CO_2 will only exist in very small amounts at the temperatures obtained in the silicon producing process (1300-2000°C).

$$C(g) + CO_2(g) = 2CO(g) \qquad \text{(Boudouard reaction)} \qquad (2.7)$$

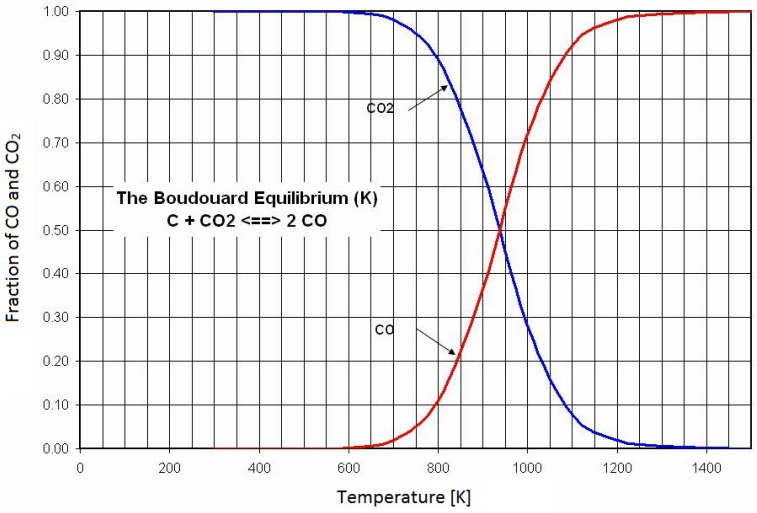

Figure 2.2: Equilibrium of the Boudouard reaction [10].

Several of the reactions occuring in a silicon producing furnace will produce SiO(g), and in the silicon furnace, SiO(g) and CO(g) will be the prevailing gas species. Figure 2.3 shows the calculated ratio between the partial pressure of SiO(g) and CO(g) against temperature by dominating reactions in the furnace [11]. In this figure, it is assumed that the total pressure is 1 bar and that SiO(g) and CO(g) are the only gases present in the furnace.

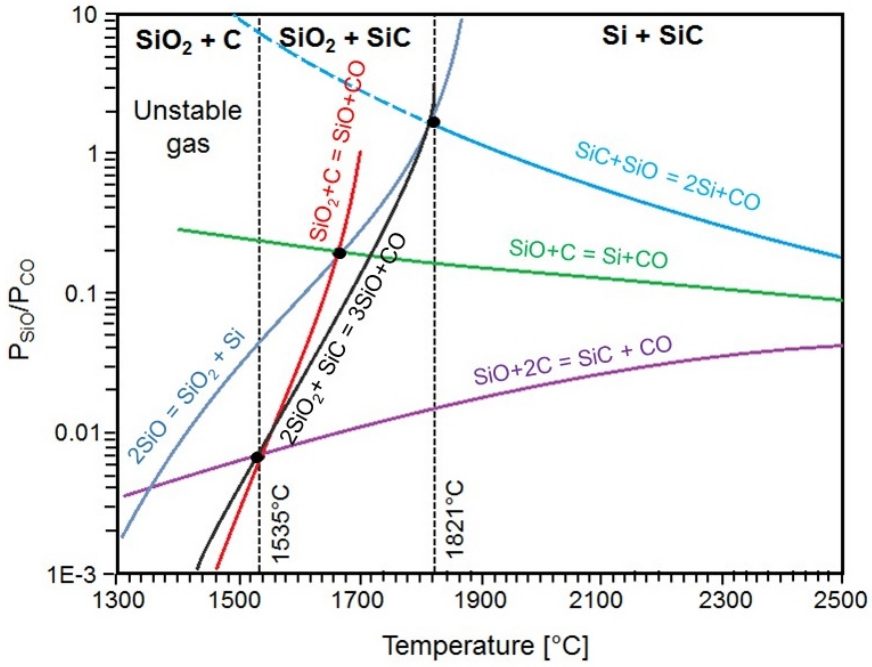

Figure 2.3: Equilibrium diagram for the dominating reactions in a silicon furnace, after Bao et al. [11]

2.1.1 Inner structure of silicon furnaces

Figure 2.4 shows the suggested structure for a working silicon furnace, as presented by Lynch [12]. This structure is the same as the structure presented by Schei et al. [6]. The relative sizes of the furnace pot and electrode are similar to that in production furnaces, and the figure shows a furnace producing silicon or high silicon ferrosilicon shortly before it is ripe for stoking. From the figure, it is observed that the carbon lining is in contact with both solid and liquid silicon, silicon carbide, and a Si-SiC slurry.

In some cases, oxides from the raw material charge could be present all the way down to the lining. It has also been established through furnace excavations that slag could be present all the way down to the bottom of the furnace [13]. The slag found in silicon furnaces usually consists of the oxides Al_2O_3, CaO and SiO_2 [6].

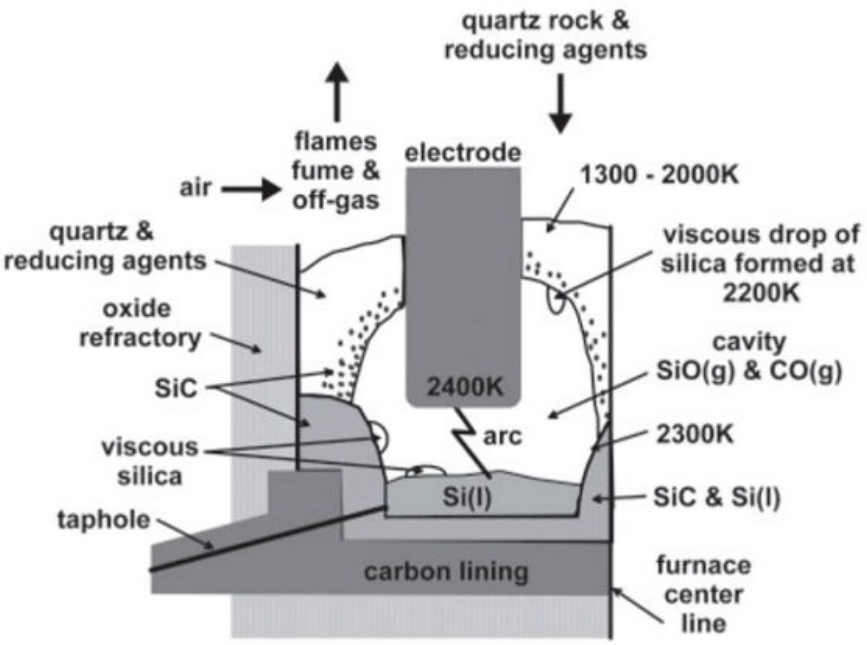

Figure 2.4: Structure of a working silicon furnace. [12]

2.2 Carbon refractory materials

The discovery that some materials have higher temperature resistance than others is probably almost as old as the discovery of fire itself, and already 30 000 years ago, chinese bakers used certain clays as refractory lining in their ovens [14]. Production of refractory materials has developed as a major industry parallel to the development of the metal producing industry, and selection and design of good refractories has been essential for good furnace operation and furnace lifespan.

There are a lot of different refractories to choose from, depending on the properties desired from the lining. The most common materials are silica refractories, aluminosilicates, magnesia-based refractories, silicon carbide and carbonaceous (graphite or carbon) refractories [14]. The focus of this report will be on carbonaceous refractories.

2.2.1 Lining design principles

An important factor to furnace design is the choice of refractory materials. These are chosen to ensure the desired heat conduction away from the furnace, i.e. to optimize production while ensuring sufficient cooling. When designing a furnace lining, two main approaches might be applied [3];

- Insulating linings
- Freeze linings

The insulating lining is designed to minimize the heat loss, and keep as much heat as possible inside the furnace. This is a desired property, but it also leads to higher temperatures at the refractory hot face. A high temperature at the refractory hot face, $T_{hotface}$, increases the chance of a molten layer of slag/silicon at the refractory surface, which could have an effect on the degree of wear on the lining. The molten slag/silicon could intrude into the lining, and the lining could be dissolved in the slag.

The freeze/conducting lining is designed to conduct heat away more efficiently, which leads to lower temperatures on the refractory hot face. The reduction of $T_{hotface}$ leaves a layer of frozen slag/metal/raw materials on the refractory surface, which could protect the lining surface from wear by the furnace content. An illustration of the two lining principles is given in figure 2.19, which shows the heat transfer out of the furnace for the two main types of lining.

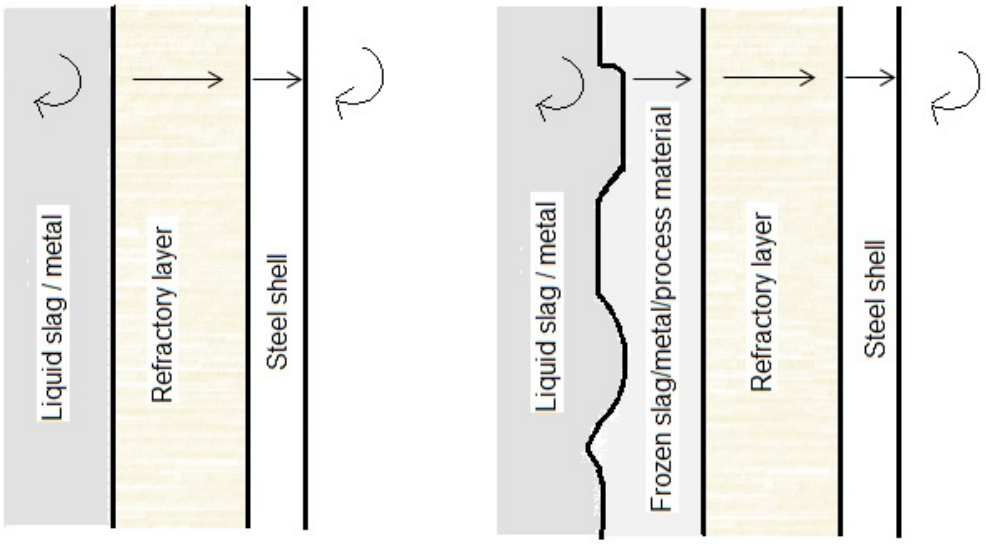

(a) Insulating lining **(b)** Freeze lining

Figure 2.5: Illustration of the insulating and the freeze lining principles, and the heat transfer through the two principles. The curved arrows indicate heat transfer through convection, straight arrows through conduction (After J.D. Steenkamp [3]).

The insulating lining has traditionally been the most common choice for submerged arc furnaces, but the freeze lining concept has increasingly gained acceptance in the industry over the last 10-15 years [4][15]. It is also possible to design linings as a combination of freeze lining and insulating lining.

2.2.2 Structure and properties of carbon refractories

Carbon linings are made up of solid carbon materials, mixed together with a binder. As previously mentioned, the carbon lining is usually in direct contact with the furnace content in the bottom parts of the furnace. Because of this, it needs to fulfill certain requirements [16]:

- Resistance to furnace content
- Low absorption of metal
- Withstand high temperatures
- Good electrical conductivity
- Mechanical strength

Carbon solids in carbon linings

Carbon used in industrial linings has a polycrystalline and polygranular nature, giving an anisotropic structure. The anisotropic structure leads to anisotropy in the thermomechanical properties of the carbon, such as in thermal and electrical conductivity. The polycrystalline carbons span from amorphous (local alignment only) to graphitic (extended alignment of basal planes)[17].

The carbon particles used for refractory materials are usually coals, graphite or petroleum coke. These solid particles are added in different size fractions to ensure the best packing; smaller particles fill the voids that occur between the bigger particles, increasing the bulk density and minimizing the inter-particle porosity [18]. The carbon solids have to fulfill certain requirements due to the harsh conditions in the submerged arc furnace; they have to have low expansion during heating, high density (low porosity), high electrical conduction, high compressive strength and elasticity [16].

Anthracite is the most common carbon solid for lining materials, and is the basis for the lining materials applied in the experimental work for this report. Anthracite is a type of coal with high content of carbon and low amount of impurities

and volatile components, such as sulfur and phosphorus. The carbon solids are often calsined in high temperatures, which removes the last of the volatile components. When using an electric calciner, the temperature varies from 1300-3000°C, meaning that some of the carbon materials go through graphitizing. This changes the structure towards a more graphitic structure, which alters the properties by increasing the heat conductivity and electric conductivity of the carbon solids significantly. Graphitizing also increases the resistance against chemical attack [19]. Figure 2.6 shows the change in structure from a non-graphitic to graphitic structure.

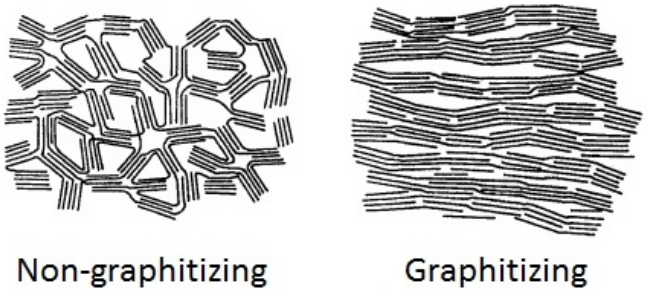

Figure 2.6: Structure of non-graphitic and graphitic carbon. [17]

As previously mentioned, the electrical resistivity of carbon materials depends greatly on the material structure and anisotropy. As the anthracite grains are calsined and aqquire a partially graphitic strucure, the resistivity of the grains become more dependent of the direction of the basal planes. The resistance is significantly larger for the direction perpendicular to the basal graphene planes than for the parallel direction, as can be seen in figure 2.7, which is a resistance plot for graphite. The figure shows the resistance in the two directions as a function of temperature. It is noted that the difference in resistance between the two directions decreases with increasing temperatures.

Similar to the electrical resistivity, the thermal properties of carbon materials also depend on the material structure and anisotropy. The thermal conductivity is significantly larger parallel to the basal planes than perpendicular to the basal planes, but it is noted that they both have the same trend in temperature dependence, see figure 2.8.

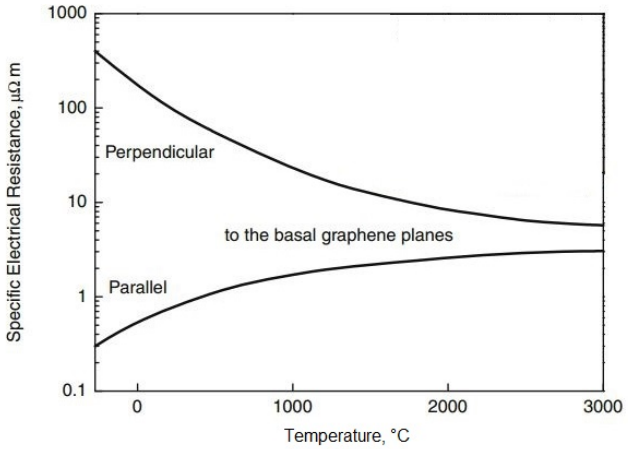

Figure 2.7: Resistance in two different directions in graphite as a function of temperature, after Shabalin [20].

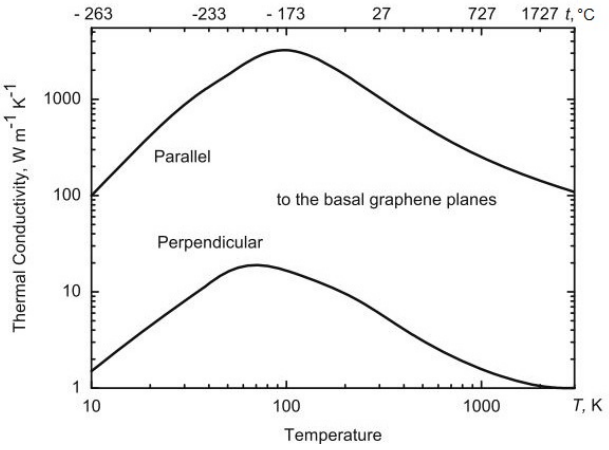

Figure 2.8: Thermal conductivity in two different directions in graphite as a function of temperature [20].

It is not uncommon to mix other additives to anthracite based paste, such as graphite to increase the thermal and electrical conductivity, or small fractions of solid silicon. The purpose of adding solid silicon is to obtain reaction with carbon in the lining as the lining is heated, creating strong and resistant silicon carbide. This conversion starts occuring very slowly as the temperature rises above approximately 1200°C, with increasing reaction rates as the temperature increases and the silicon particles melt.

Binders

To the mix of dry carbon fractions, a binder is added. The purpose of the binder is to keep the solids toghether and make a paste. To do this, the binder has to fill the voids between the solids and fill any pores on the solid particles themselves. The most commonly used binders for carbon lining are coal tar pitch, petroleum pitch, or resin. Requirements for the binder include high degree of wetting between the solids and the binder, temperature stability and similar reactivity as the solids after baking of the lining [16].

Recently, awareness of the potential harm caused by polycyclic aromatic hydrocarbons (PAHs) in traditional binders has increased. PAHs can cause cancer in humans and severly damage the environment [21], and PAH free binders are now often preferred for carbon linings and electrodes.

2.2.3 Installation of carbon lining in metal producing furnaces

Several different types of lining exist, and they are installed in furnaces using slightly different procedures. The two main types are prebaked lining blocks and carbon lining pastes. Prebaked blocks are a mix of calcined anthracite, calsined coal, petroleum coke or carbon black, with either petroleum or coal tar pitch as binder. The bricks/blocks are shaped in moulds or extruded, before they are baked at temperatures between 800 and 1400° C to carbonize the binder [3]. Prebaked blocks are installed in the furnace with minimal gaps inbetween the blocks, or with ramming paste to fill the gaps.

Carbon paste is a mix between calcined anthracite, graphite aggregates or petroleum coke mixed with resin, tar or petroleum pitch. This type of lining is installed by ramming in layers of up to 9 cm thickness per layer after ramming. The final thickness of the lining, and thus the total number of layers, depends on parameters such as the desired temperature drop through the lining. After installation, the carbon paste is baked in the furnace at a minimum temperature of 550°C, which creates a monolithic lining. All the lining samples used in the experimental work for this report are made from carbon tamping paste.

Carbon tamping paste with high thermal conductivity is often also installed in the outer parts of the furnace, between the oxides and the steel shell. This is done both to ensure cooling of the lining, and to act as a final protector of the steel shell in case liquid metal should work its way through the inner carbon and oxide refractory layer.

During mixing and installation of carbon lining paste, problems involving segregation must be considered. As the dry mix of solid carbon particles contains different size fractions, mixing and installation has to be executed in a way that avoids segregation of the different fractions. Figure 2.9 shows how larger particles collect closer to the wall when segregation occurs during filling, while the smaller particles are found closer to the center. Segregation could comprimize the packing, and result in areas with increased porosity [18]. Segregation may also occur during mixing and other forms of handling.

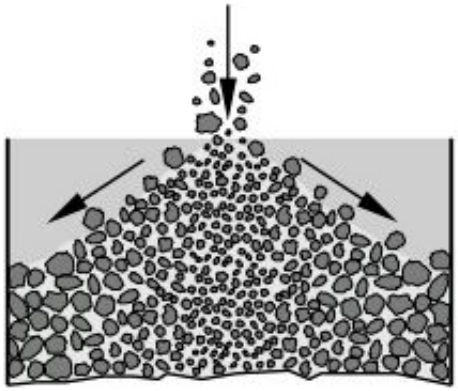

Figure 2.9: Illustration of how larger particles segregate from smaller particles when segregation occurs during filling [22].

2.2.4 CT investigations of carbon lining morphology

In the preliminary project work for this report [5], the internal morphology of different carbon lining samples was investigated using CT (X-ray computed tomography). The lining samples were prepared using two different preparation techniques;

- Standard samples normally used for testing of physical properties, produced by ramming paste in a cylindrical container with 100 strokes using a Fischer-Sandrammer, which applied even force across the entire sample. This gave solid sylindrical samples with Ø50 mm and height of approximately 58 mm.

- Layered samples produced by ramming one layer of paste to approximately 60 mm height using a star shaped ramming head, before adding more paste and ramming the next layer to about 60 mm height. This was repeated until the finished samples consisted of 4 layers of 6 cm each.

CT investigations of the interior of each sample type showed that the preparation technique had influenced the internal morphology of the lining. By processing the images using the image processing program ImageJ, it was possible to obtain orthogonal views of the samples in X-Z and Y-Z direction. These images showed that while the samples prepared in the Fischer-Sandrammer had uniform density in height direction, the layered samples showed clear density variations depending on position relative to the ramming layers. This was confirmed by using ImageJ to calculate the average density of each cross section of the sample, and plotting the density as a function of height in the sample. Figure 2.10 shows the orthogonal view of a layered sample in X-Z direction on the left hand side, and the average cross section density as a function of height on the right.

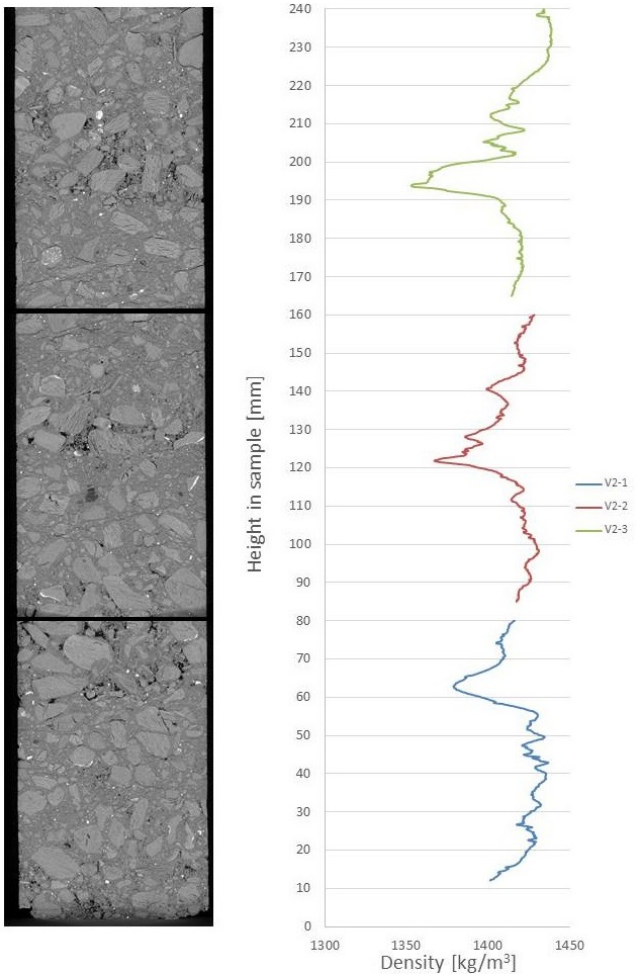

Figure 2.10: Orthogonal view of layered sample V2 in X-Z direction, and the average cross section density as a function of height.

Transition areas between the layers can be observed at approximately 65 mm, 125 mm and 195 mm. The porous areas are assumed to be the bottom of each ramming layer, where the paste has been less compacted by the ramming procedure. Directly below these porous areas, 5-10 mm of lining with higher density and fewer large grains can be observed. This is assumed to be the top section of the ramming layers. It was also observed that an accumulation of large grains had occurred at the bottom of each layer, and it was assumed that this segregation was caused by vibrations during the layer ramming, rearranging the grains as the samples were prepared.

Figure 2.11 shows results obtained from CT scans of one of the solid, standard Fischer-Sandrammer samples. The left hand side of figure 2.11a shows the orthogonal view in the X-Z direction of sample FS1. The average density for each cross section was obtained using ImageJ, and the average density as a function of height is given in the right hand side of figure 2.11a. Inspection of these samples showed a much more even density distribution in across the height (Z-direction), but differences across the X-Y cross section. The porosity in one half of the sample proved to be larger than for the other half, which can be seen in figure 2.11b. This was assumed to be caused by segregation occuring as the paste was moved into the cylinders for sample preparation.

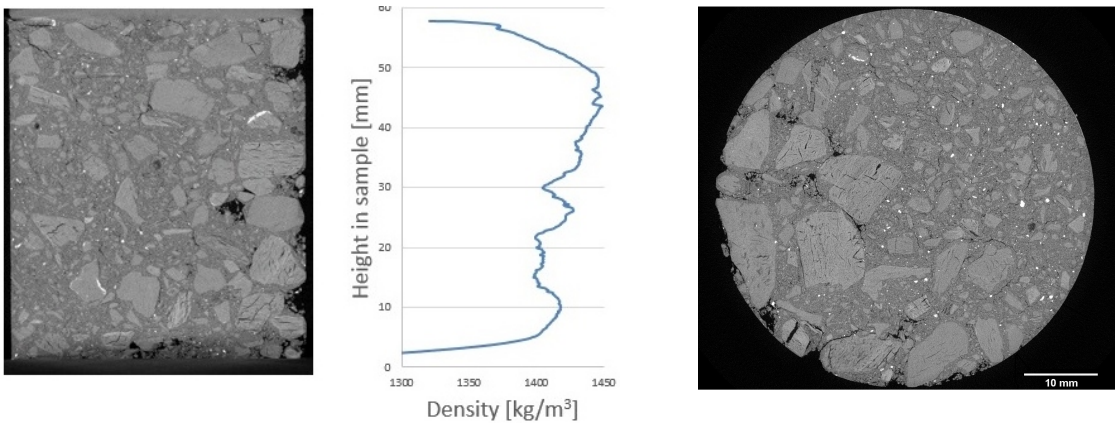

(a) X-Z orthogonal view and density profile **(b)** X-Y cross section

Figure 2.11: X-Z orthogonal view, average cross section densities and a X-Y cross section for solid sample FS1.

2.3 Furnace content properties

2.3.1 Properties of silicon

Experimental data from studies by Glazov and Shchelikov [8] in table 2.1, show that the density of a silicon melt at the melting point is higher than that of crystals at the same temperature. The data also show that the melt volume is smaller, meaning that silicon melts with compaction and crystallizes with expansion. This is one of the properties that make silicon a popular alloying element in casting metals, as it counteracts the shrinkage and potential crack formation that occur during solidification of most metals. This property could also cause difficulties if liquid silicon intrudes into the lining and then solidifies, more on this in section 2.4.

Table 2.1: Changes in the density and specific volume upon melting of silicon [8].

Substance	T_m [°C]	ρ_L-ρ_S [g cm^{-3}]	V_L-V_S [cm^3 g^{-1}]
Silicon	1416	0.25	-0.043

The resistivity of silicon is dependent on temperature, and decreases as the temperature of the melt increases. This temperature dependency is caused by the semiconductive properties of silicon. For an electron to be able to flow through a material and conduct electricity, a certain minimum energy is required. In semiconductors such as silicon, all electrons have strong bands in the crystal structure, making them unavailable for electrical conduction [23]. To obtain free electrons that can participate in current conduction, the semiconductor has to be subjected to elevated temperatures which cause thermal vibrations, breaking free the electrons from their bands. As the temperature increases, the number of electrons with enough energy to stay in the conducting state increases [24]. This leads to an improvement of the conducting properties of the silicon, and thus the resistance decreases.

Oxidation of silicon can occur both when the silicon is in solid state, and after melting to liquid state. In silicon production, oxidation of produced silicon can occur both during tapping and refining, and is a big source of fugitive emissions in the plant [25]. The rate and type of oxidation strongly depends on both oxygen partial pressure and temperature.

If silicon is heated without any shielding gas, interactions between silicon and oxygen could occur. This could occur either through passive oxidation, where

solid silicon oxide forms on silicon as in reaction 2.8, or through active oxidation, where the formed silicon oxide is gaseous as in reaction 2.9.

$$\mathrm{Si(l/s)} + \mathrm{O_2(g)} = \mathrm{SiO_2(s)} \tag{2.8}$$

$$\mathrm{Si(l/s)} + \frac{1}{2}\mathrm{O_2(g)} = \mathrm{SiO(g)} \tag{2.9}$$

Already at room temperature, a very thin layer of silica would form on the surface of fresh, solid silicon [26]. As the temperature increases, this oxide film thickens through passive oxidation until the temperature reaches a certain temperature T*. At T*, silicon deoxidination occurs according to reaction 2.10, where the oxide film reacts with the underlying silicon to form SiO(g):

$$\mathrm{Si(l/s)} + \mathrm{SiO_2(s)} = 2\mathrm{SiO(g)} \tag{2.10}$$

Above temperature T*, active oxidation occurs according to reaction 2.9. T* is dependent upon the partial pressure of oxygen in the furnace. Which type of oxidation occurs, depending on the oxygen partial pressure and temperature in the furnace, can be seen from figure 2.12.

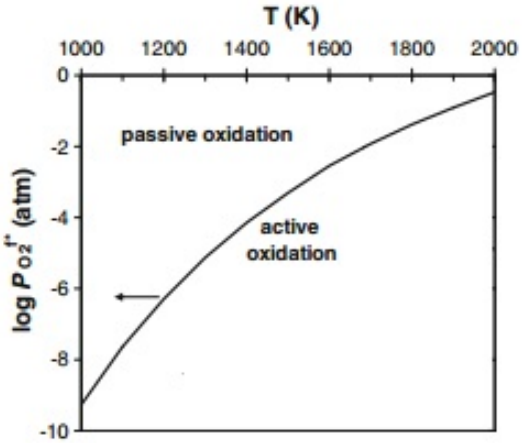

Figure 2.12: The domains of active and passive oxidation of silicon at different oxygen partial pressures and temperatures, after Drevet and Eustathopoulos [26]. P_{O_2} is the partial pressure of oxygen in the furnace, T is the temperature in the furnace.

2.3.2 Properties of slags for silicon production

Production of silicon through the carbothermic process is usually defined as a slag free process [6]. This is, however, not complient with reality, and slags are formed and tapped from silicon producing furnaces in various amounts. The amount and composition of the slag that forms in the furnace depends on several factors, such as the furnace operating conditions, the input of aluminium and calcium, and the relative distribution of these elements in the feed [6].

The slag in silicon producing furnaces usually consist of silica (SiO_2), alumina (Al_2O_3) and lime (CaO) in different ratios. Figure 2.13 shows the ternary phase diagram for these components [27].

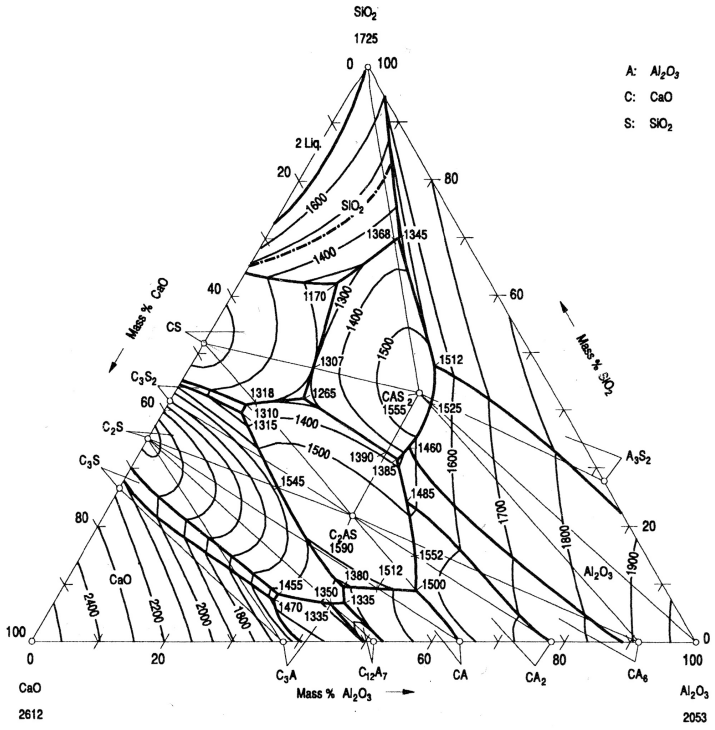

Figure 2.13: Ternary phase diagram for the Al_2O_3-CaO-SiO_2 system [27].

The density and viscosity of different compositions of these elements have also been estimated. Figure 2.14a shows the suggested isodensity lines for the system at 1550°C, with the values given in g/cm^3. This diagram is based on data given by Winterhager [28] and Barrett [29]. Figure 2.14b shows iso-viscosity (poise) contours for the alumina-silica-lime melts at 1500°C [27]. The density and viscosity

is especially important for how the slag behaves in the furnace; the density determines the position of the slag relative to e.g. the liquid silicon, and the viscosity describes how the slag flows in the furnace.

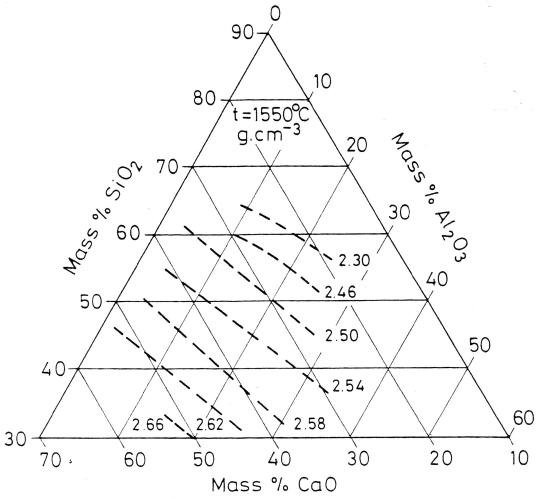

(a) Isodensity lines

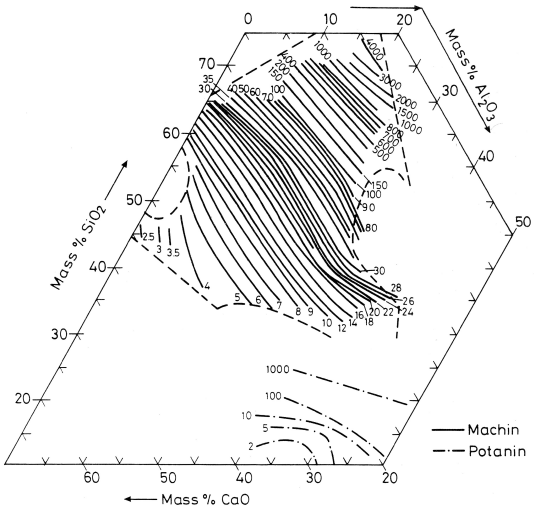

(b) Iso-visvosity contours

Figure 2.14: Isodensity lines and iso-viscosity contours for the Al_2O_3-CaO-SiO_2 system [27].

2.4 Wear mechanisms

In a submerged arc furnace, there are four main mechanisms of carbon lining wear: densification, spalling, erosion and corrosion [3].

Densification is the process of infiltration by liquid metal and/or slag into the lining, possibly reacting with the refractory material. Spalls are flakes of the refractory material broken off from the solid lining structure, and *spalling* could occur due to densification, or thermal stress caused by i.e. a high thermal gradient across the refractory body. *Erosion* is mechanical wear on the lining caused by abrasion by solid furnace content. *Corrosion*, or chemical wear, occurs if the system is not at equilibrium, and the slag, metal or raw materials react with the carbon lining. Corrosion is especially problematic if one of the phases (binder or aggregate) is more reactive than the other, which leads to localized corrosion.

2.4.1 Chemical wear

Chemical reactions between the furnace content and the carbon from the lining occur in all silicon producing furnaces. The possible reactants, apart from carbon, are SiO_2, SiO(g) or Si (l). Chemical reactions between carbon and these furnace constituents could either lead to consumption of the carbon, such as in equation 2.11, 2.12 and 2.14, or conversion from carbon to silicon carbide, such as in equation 2.13, 2.15 and 2.16.

$$SiO_2(s) + C(s) = SiO(g) + CO(g) \tag{2.11}$$

$$SiO_2(s) + 2C(s) = Si(l) + 2CO(g) \tag{2.12}$$

$$SiO_2(s) + 3C(s) = SiC(s) + 2CO(g) \tag{2.13}$$

$$SiO(g) + C(s) = Si(l) + 2CO(g) \tag{2.14}$$

$$SiO(g) + 2C(s) = SiC(s) + CO(g) \tag{2.15}$$

$$Si(l) + C(s) = SiC(s) \tag{2.16}$$

The potential for these reactions at 1600°C was determined using the thermodynamic calculation software HSC Chemistry. The calculated values for Gibb's free energy, ΔG^0, as a function of temperature are given in figure 2.15.

When ΔG^0 is negative, the reaction is said to be spontaneous and thermodynamically possible. Figure 2.15 shows that reaction 2.11 and 2.12 only have positive values for ΔG^0 up to 1600°C, and they will not be thermodynamically favoured

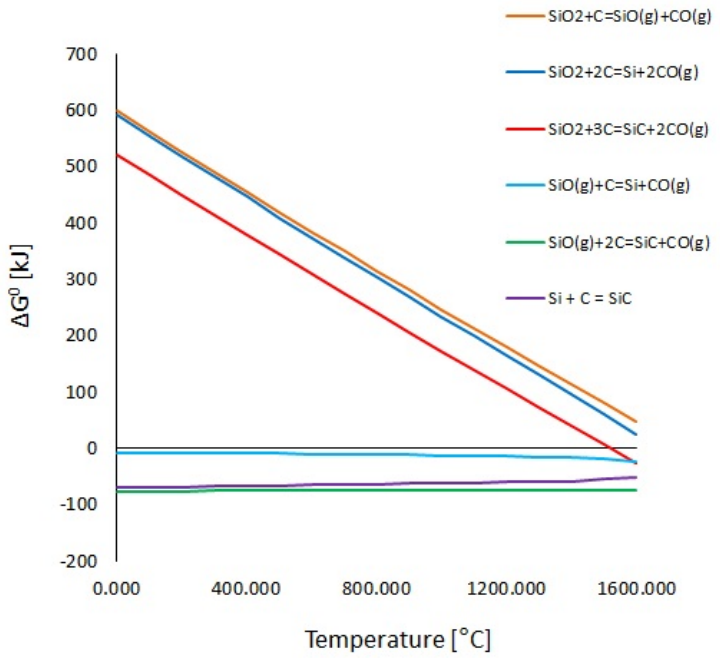

Figure 2.15: Gibb's free energy as a function of temperature for the possible reactions between carbon from lining and different furnace constituents.

in this temperature interval. The other reactions have negative values for ΔG^0, and could occur in temperatures equal to or below 1600°C. It is noted that the analysis of the chemical potential has been performed with all species in their standard state. The reaction between Si(l) and carbon forming silicon carbides, given in equation 2.16, will according to Shabalin [20] occur instantly when the two elements are in contact at elevated temperatures.

It is also worth noticing that reaction 2.13 is a solid-solid reaction. This reaction would, due to kinetics, be significantly slower than the gas/liquid-solid reactions in reaction 2.14, 2.15 and 2.16, as the only reacting surface is the shared interface between the two solid particles [30].

2.4.2 Erosion

Mechanical erosion of the carbon lining by the furnace content could occur under certain conditions. First of all, the lining design has to be of the insulating principle; freeze linings give a solid layer on the lining surface which acts as protection against erosion. Second of all, erosion requires that solid furnace content, not only

liquids, is in contact with the lining.

The possible solid furnace constituents in contact with the furnace lining are the oxide raw materials, solid silicon, and silicon carbide formed in the furnace. Quartz (oxide raw material) has a hardness of 7 on Moh's hardness scale [31][32], and silicon carbide has a hardness around 9-9.5 [31][33] (in comparison; diamond has the highest value of 10 on Moh's scale), making both quartz and silicon carbide relatively hard materials. The conditions in a working silicon furnace are far from stationary, and movement of the solid furnace constituents could lead to erosion of the softer carbon lining. Preventing extensive lining erosion is one of the reasons why larger anthracite grains are added to the lining mix; larger anthracite grains prevent the lining from being eroded away evenly, and provide erosion resistance. This is illustrated in figure 2.16, where the binder phase and smaller fractions of anthracite have eroded while the larger anthracite grains in the carbon lining remain mostly uneroded.

Figure 2.16: Example of carbon lining erosion, where the binder phase has eroded while the larger anthracite grains remain.

It is also noted that graphite is very soft, with a hardness of only 1.5 on Moh's scale [33][34]. This is softer than anthracite, which is a quite hard type of coal [35]. This means that the probability of erosion of the carbon lining increase with additions of graphite, and when the anthracite goes through graphitization over time when exposed to high temperatures.

2.4.3 Densification

Densification occurs when liquid furnace content intrudes into the carbon lining. In silicon producing furnaces, the only liquid components are liquid silicon and liquid slag.

As liquid furnace content intrudes into the carbon lining, it fills the pores and increase the surface area between the liquid content and the carbon lining. This increases the potential for chemical reaction between the lining and the furnace content, and it may also alter properties of the lining such as thermal conductivity, electrical conductivity and mechanical strength. It also increases the possibility of spalling, more on this in section 2.4.4.

2.4.4 Spalling

As the carbon lining is subjected to furnace operating conditions over extended periods of time, spalling of the lining might occur.

Spalling could occur as a result of thermal stresses in the lining, either by large temperature changes between lining surface and lining interior, or by temperature changes inside the furnace, e.g. during furnace shut downs and start ups.

Spalling could also occur as a result of densification. This is espesially a concern in silicon producing furnaces; if silicon intrudes into the lining and solidifies, the expansion of the silicon might break of pieces of the lining. An example of intruded and expanded silicon in carbon lining is shown in figure 2.17. This shows the lining from an excavation of a silicon producing furnace, where a metal spike into the lining has occurred. This could, over time, lead to spalling.

Figure 2.17: Metal spike in carbon lining, example from silicon furnace excavation.

2.5 Wetting of carbon materials

The following section presents previously performed studies of wetting and intrusion of different furnace constituents on different carbon substrates, such as graphite and carbon lining. Studies with furnace constituents on silicon carbide will also be presented, as section 2.4.1 showed that transformation of the lining to SiC might occur in the furnace.

Several wettability studies have been performed on different types of carbon materials, by different compounds in silicon furnaces. Safarian et al. [36] performed studies of silicon carbide wettability by CaO-SiO_2 slags, Ciftja [37] investigated wetting of molten silicon on graphites and Tangstad [38] performed experiments investigating wetting by both silicon and quartz on carbon pastes and prebaked lining. All these studies were performed using the sessile drop technique. This is an important method used to characterize surface tension by capillary action of a drop of liquid material on a solid substrate.

Wetting by a liquid drop on a solid surface is usually characterized by the contact angle, θ, which is the angle formed at the gas-liquid-solid interface (illustrated in figure 2.18). θ is a function of the surface energy between the different phases. The relationship between the contact angle and the surface tension is given in the Young-Dupre equation:

$$\cos\theta = \frac{\gamma^{\mathrm{sg}} - \gamma^{\mathrm{sl}}}{\sigma^{\mathrm{lg}}} \tag{2.17}$$

where γ^{sg} is the surface energy between solid and gas, γ^{sl} is the surface energy between solid and liquid and σ^{lg} is the surface tension of the liquid [37].

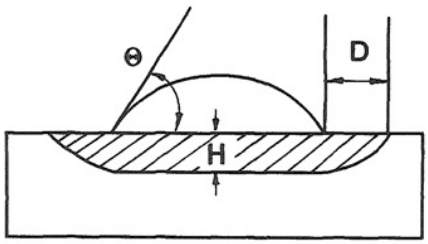

Figure 2.18: Illustration of contact angle, θ, between a solid surface and a liquid drop, and lateral intrusion (D) and vertical intrusion (H) into the substrate [37].

For $\theta > 90°$, the liquid on the solid substrate is defined as non-wetting. If $\theta < 90°$, the liquid is said to be wetting, and with $\theta = 0°$, the liquid is defined as perfectly

wetting. The H illustrated in figure 2.18 is the vertical intrusion depth of the liquid into the solid substrate, while D is the lateral intrusion.

2.5.1 Wettability of carbon materials by liquid silicon

In experiments with pure poly-crystalline silicon samples on graphite materials in a wetting furnace performed by Ciftja [37], the temperature and atmosphere were held constant, while the surface roughness of the graphite materials was varied. The holding temperature was 1500°C and the atmosphere was purified Ar(g). These experiments showed that smooth graphite surfaces gave contact angles of about 30°, while an increase in surface roughness gave decreasing θ values, eventually reaching 0° (full wetting). The samples were also examined in side view to determine the infiltration depth (H in figure 2.18), and it was determined that the infiltration depth increased with average pore diameter.

Experiments investigating wetting of polycrystalline SiC by silicon were also performed by Yupko [39], and these showed that the wetting between liquid silicon and silicon carbide was good, and that wetting increased as the surface roughness decreased. This was the same conclusion as obtained by Ciftja [37], and in the experiments, all measured contact angles were less than 20°, even on the most polished surfaces.

Experiments performed by Li and Hausner [40] using the sessile drop method investigating molten silicon on graphite substrates showed the same trend between surface roughness and contact angle as Ciftjas studies. These experiments were also performed in Ar atmosphere, and with holding temperature of 1430°C. In this study, the relationship between the surface contact angle θ and vertical intrusion depth H was investigated more thoroughly, and Li and Hausner also looked more closely into the lateral intrusion (D) of the silicon on graphite. It was concluded that the vertical intrusion was independent of the contact angle, but that the lateral intrusion seemed to dependend on the wetting behaviour. The experimental results are shown in figure 2.19a and 2.19b.

Experiments using the sessile drop technique were performed by Tangstad [38] using poly-crystalline silicon on two different types of carbon paste and one prebaked lining. The experiments were performed in a wetting furnace with heating rates of 300 °C/min to 950°C, 100 °C/min to 1350°C and 20 °C/min to 1900°C. All experiments were performed in CO gas with the exception of one experiment performed in Ar. The aim of this experiment was to investigate the vertical intrusion of liquid silicon into the three lining materials, and the infiltration images are given in figure 2.20.

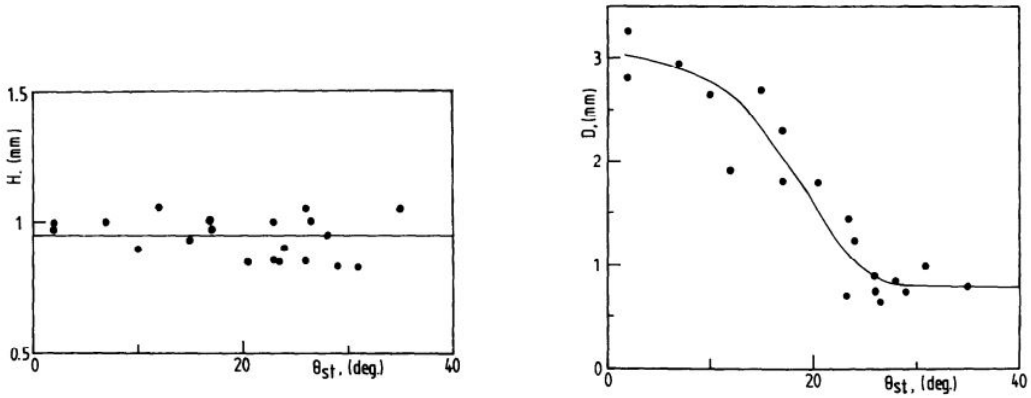

(a) Vertical intrusion depth (H) **(b)** Lateral intrusion depth (D)

Figure 2.19: Intrusion of molten silicon on graphite as a function of contact angle θ in vertical and lateral direction [40].

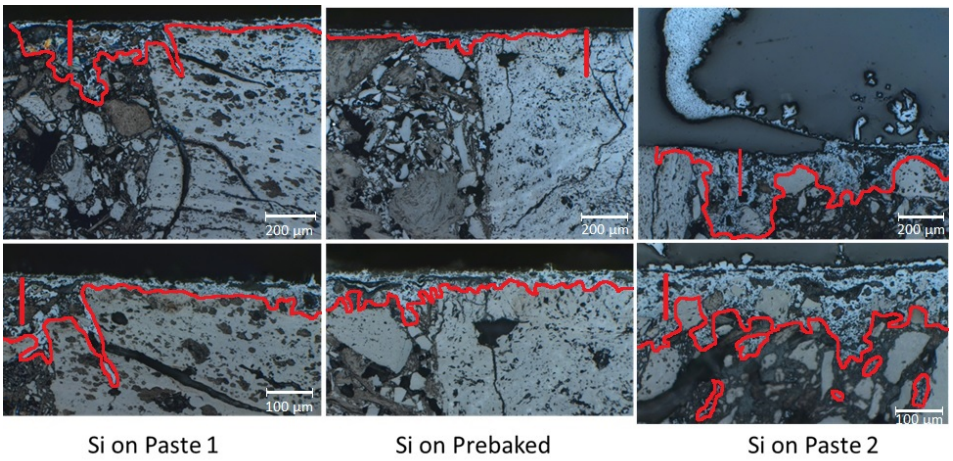

Figure 2.20: Vertical intrusion of Si in three different carbon linings [38].

The maximum infiltration depth was measured to approximately 300 μm for the two pastes, and only 50 μm for the prebaked lining. When repeating the experiment for paste 2, only changing atmospheres from CO to Ar, the maximum infiltration depth increased to 500 μm.

2.5.2 Wettability of carbon materials by raw materials

In the same study by Tangstad, the wettability and intrusion of quartz was investigated on the same three types of linings in CO gas. The experiment showed no wetting of any of the linings, see figure 2.21, but some dents in paste 2. After examination in SEM, the maximum intrusion depth was determined to approximately 100μm for the two carbon pastes, and 100 μm for the prebaked lining sample. It was also observed that attack from the quartz on the lining occurred on the aggregates, not in the binder phase. This is opposite of the observations with silicon from the same study, where the binder phase was attacked.

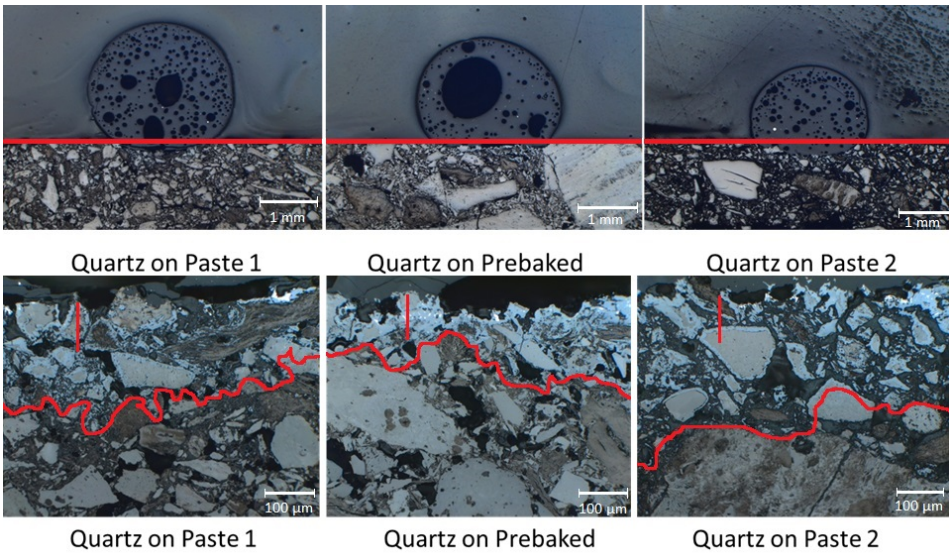

Figure 2.21: Intrusion of quartz in three different carbon linings [38].

2.5.3 Wettability of carbon materials by slags

Wettability of SiC by CaO-SiO_2 slags was studied by Safarian et al. [36] using the sessile drop technique in both Ar and CO atmospheres. Different heating regimes were used to melt slags with SiO_2 content varying from 47-60 wt%, and the maximum temperature was set to 1600°C. The study used both SiC powder substrate and SiC single crystal, and the results showed that the wetting on both types of SiC was relatively high, but infiltration could only be observed in the powder substrate. From this study, it was also concluded that the heating regimes did not influence the wetting, which was only dependent on the slag composition and atmosphere. The wetting in CO gas proved to be lower than in Ar atmosphere, which is in compliance with the results obtained by Tangstad for Si on carbon lining samples. It is noted that CO(g) is a common gas to find in a silicon producing

furnace [11], while Ar(g) is not. The study also showed that wetting decreased as the SiO_2 content in the slag increased. This is also in accordance with Tangstads study, showing no wetting by quartz on the carbon lining samples. When increasing the amount of SiO_2 in the slag from 47 wt% to 60 wt%, the wetting decreased from almost complete wetting with contact angle $\theta = 0$, to non-wetting with contact angle $\theta > 90°$.

Mailliart et al. [41] performed experiments in a sessile drop furnace studying wetting between polycrystalline SiC and 23 wt%CaO, 15 wt% Al_2O_3, 62 wt% SiO_2 oxide glass under air for temperatures between 1100 and 1590°C. These studies showed that good wetting is obtained in the oxide glass/SiC system, and that the wetting depends somewhat on the temperature. The final contact angle θ_F is lower than 50° for temperatures above 1300°C, while it was significantly larger in the experiment conducted at 1100°C. This is shown in figure 2.22, which also shows that the spreading kinetics is rapid and increasing as the temperature increases. The final contact angle θ_F is reached in less than 7 min for all temperatures except for the experiment performed at 1100°C. In that experiment, θ_F was not reached even after 30 min of spreading.

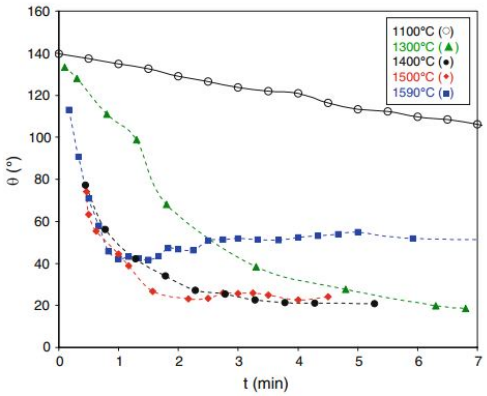

Figure 2.22: Kinteics of slag spreading (contact angle θ vs time) on SiC at different temperatures [41].

It was observed by Joalet Steenkamp [3] in her PhD thesis that industrial slags from silicomanganese furnaces containing CaO, Al_2O_3, SiO_2 and MnO wetted the surface of carbon lining paste perfectly. It was also observed that parts of the lining had been converted to SiC during experiments, and that this SiC could often be found in the slag surrounding the carbon lining surface.

2.6 Induction furnace experiments

Experiments subjecting carbon lining to liquid silicon in an induction furnace was performed in the preliminary work [5], exposing baked carbon lining paste samples to liquid silicon at 1600°C for 40 minutes. The samples were investigated using CT both before and after exposure to liquid silicon.

2.6.1 Densification/intrusion

The experiments performed in the preliminary work [5] showed that no intrusion of liquid silicon into the carbon lining occurred during experiments in the induction furnace, not even in extremely porous areas. Figure 2.23 shows how porous areas at the surface have not even been wetted by the liquid silicon.

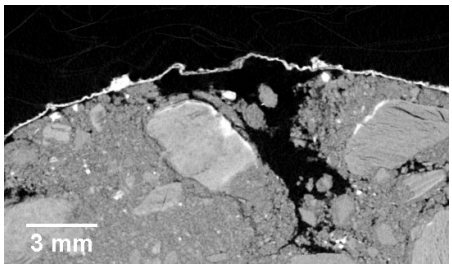

Figure 2.23: Porous area of carbon lining sample exposed to liquid silicon.

Five sylindrical samples were tested, with a total summed area of metal exposure of 40 cm^2, and only one single case of silicon intrusion was detected. CT images showing this area both before and after exposure to silicon is shown in figure 2.24, as well as an orthogonal view of the sample in Y-Z direction.

Figure 2.24 shows that the intrusion into the lining occurred into an athracite grain, and not into the binder phase. From this results it was speculated whether there were any difference in wetting of the grains and of the binder phase.

2.6.2 Corrosion

In the same set of samples, cases of chemical reactions with the carbon lining was found in the CT scans performed after exposure to silicon. Comparison with the CT images taken before the experiments in IF-75 showed that no lining had been consumed, and it was concluded that the chemical reaction had to be conversion. It was assumed that the conversion product was SiC, silicon carbide. Figure 2.25 shows CT images of the same area of a layered sample, where figure 2.25a shows

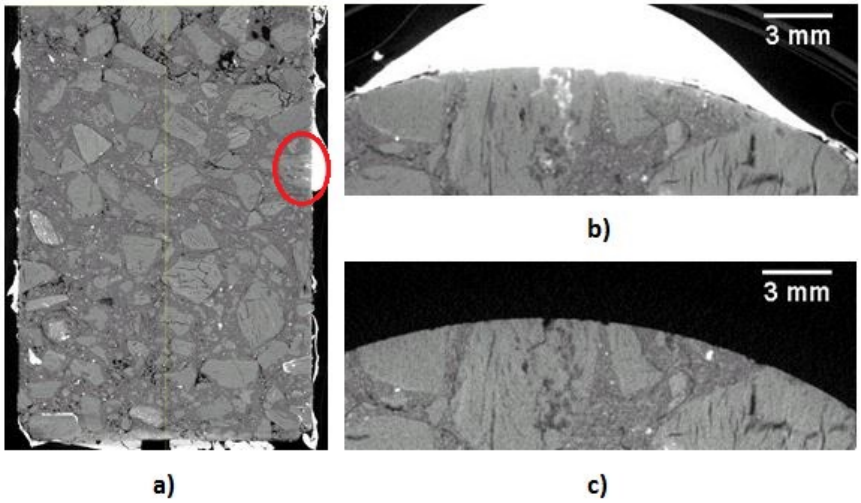

Figure 2.24: Intrusion of liquid Si into carbon lining sample: a) area of intrusion seen in Y-Z direction, b) parts of the cross section with intrusion and c) pre metal exposure scan from the same area.

the area before exposure to silicon and figure 2.25b shows the same area after exposure to silicon.

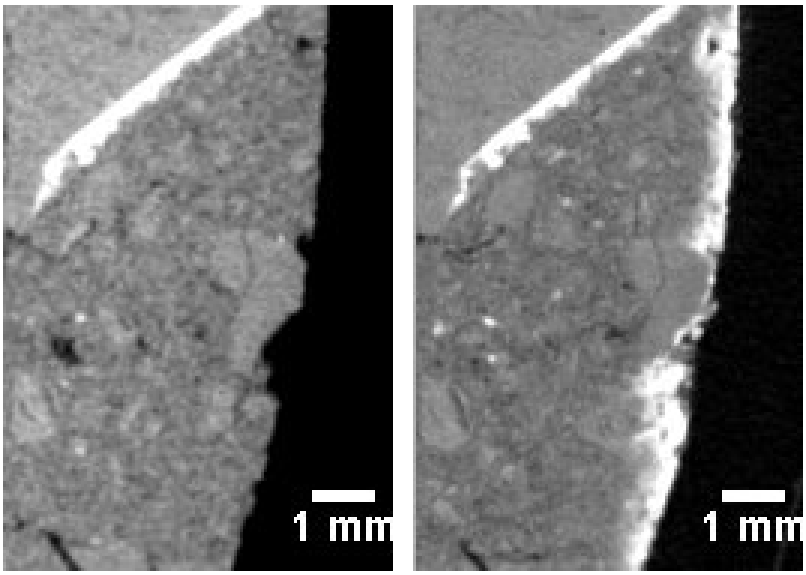

(a) Before exposure to silicon **(b)** After exposure to silicon

Figure 2.25: Corroded area of a carbon sample surface, with a formed layer of silicon carbide. Images from both before and after exposure to silicon.

2.7 Furnace theory

2.7.1 Induction heated furnace

In an induction furnace, copper coils surround a crucible, which holds the metal charge. An alternating current flows through these copper coils, producing alternating magnetic fluxes. As the crucible holding the metal is placed in this magnetic flux, electromotive forces are induced in the metal, creating eddy currents. These eddy currents are circulating movements of electrical current within the metal bath, and are caused by the intersection of the conductive metal with the moving magnetic field. If a conductive crucible, for instance made of graphite, is used, eddy currents will also be created in the crucible. Figure 2.26 shows an induction furnace with the fluxes and induced eddy currents that occur due to the alternating currents.

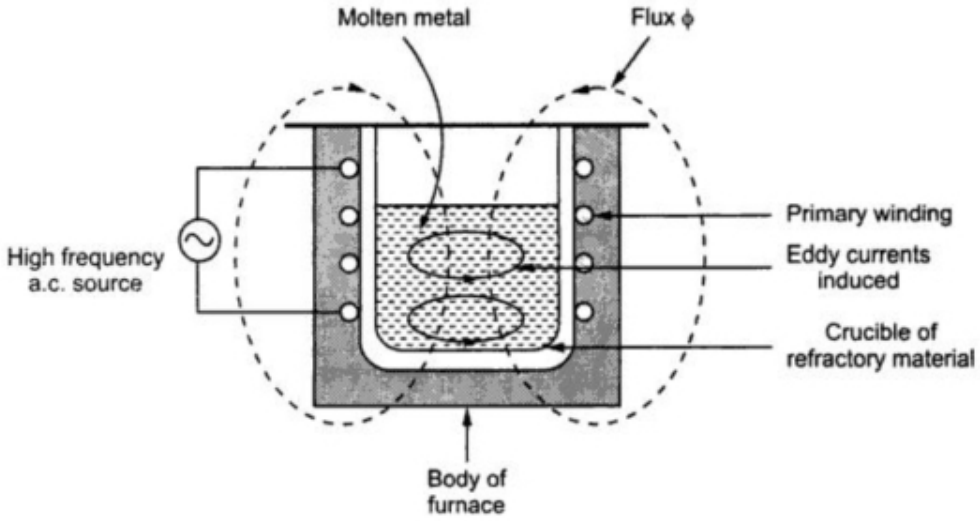

Figure 2.26: Schematic diagram of an induction furnace using the transformer principle [42].

The induction of currents in the metal occurs according to Faradays law, which states that the amount of voltage created is equal to the change in magnetic flux divided by the change in time. This correlation gives that the amount of voltage increases as the change in the magnetic field increases [43]. In mathematical terms, the electromotive force induced in the metal can be expressed as

$$\epsilon = \frac{d\phi_B}{dt} \tag{2.18}$$

where ϵ is the electromotive force, ϕ_B is the magnetic flux and t is time [43].

The induced eddy currents, flowing through the electrical resistance of the bulk metal, heat the metal according to Joules law. Joules law give the relationship between the produced electrical current, the electrical resistance of the metal and the heat produced, and is given in equation 2.19:

$$Q = I^2 * R * t \tag{2.19}$$

where Q is the amount of heat, I is the electric current flowing through the metal and R is the electrical resistance in the metal. This relationship shows that the efficiency of the induction furnace depends on the resistance of the heated materials, as well as the produced current. When heating two different materials in the same crucible, the current would be the same through both materials, but the electrical resistivity will most likely be different. This could lead to one furnace constituent overheating relative to the other, which might produce thermal stresses.

2.7.2 Resistance heated furnace

Resistance heated furnaces are electric furnaces where the heat is produced by leading an electric current through a material with suitable resistance. The electrical resistance creates Joule heating, which occurs according to Joules law (eqation 2.19).

Resistance heated furnaces are separated into two types; indirect or direct heating. The furnace used in the experimental work for this report is of the indirect type. Indirect resistance heated furnaces are constructed with a working chamber surrounded by refractory layers and heat insulation. Inside the working chamber, close to the refractory wall, heating elements are placed to provide heat. These heating elements are heated by Joule heating from electric currents. A crucible holding the charge is placed inside the working chamber and the charge is heated through radiation, convection or conduction. Figure 2.27 shows a schematic diagram of an indirect resistance heated furnace.

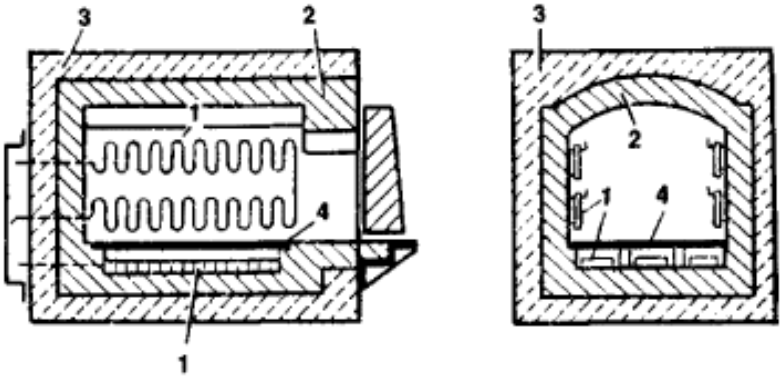

Figure 2.27: Diagram of a batch-type indirect-heat resistance chamber furnace: (1) heating elements, (2) refractory lining, (3) heat insulation, (4) refractory hearth plate [44].

2.8 Methods of wear investigation

2.8.1 X-ray computed tomography

X-ray computed tomography, or CT, is a non-destructive imaging method which allows inspection of the internal morphology in samples. The non-destructive nature of investigations using CT makes it a useful tool to provide information about both pristine and silicon exposed lining samples, and gives the opportunity to compare the inside of larger samples before and after experiments.

In CT, X-rays are created and emitted in a fan-beam from an X-ray source. This beam of x-rays is translated across and rotated about an object. When the X-rays travel through one slice of the object, some X-rays are attenuated by the material while some travel straight through, depending on the density of the material the X-rays encounter. On the other side of the object, a X-ray detector is placed to register these X-rays [45]. Figure 2.28 shows the X-ray source, fan-beam, object and X-ray detector.

As the X-ray source, and thus the fan-beam, is rotated about the object, several projections from different angles are obtained. These can be filtered and back-projected, showing the density across an entire cross section. Figure 2.29 shows how the density projections are obtained, filtered and combined to e.g. to show areas with increased density (the red circle) in an object.

The result is a stack of cross section images which displays differences in density by variation of gray scales; areas with higher density will be shown in brighter

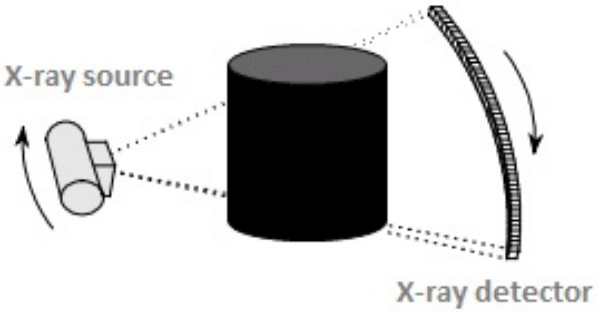

Figure 2.28: Illustration of the X-ray computed tomography (CT) setup; X-ray source, fan-beam and X-ray detector. After Powsner et al. [45]

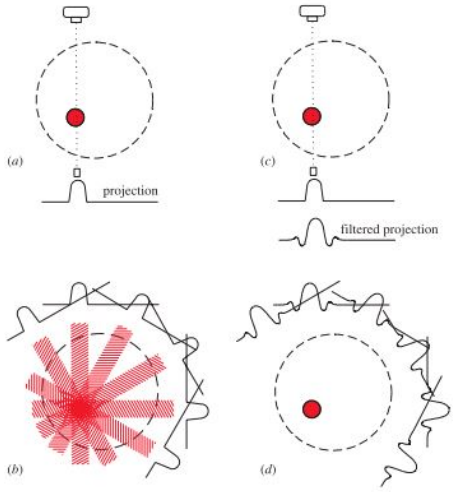

Figure 2.29: a) shows the attenuation profile measured from one angle, while b) shows the back-projection where all the attenuation profiles are projected across the image plane. c) shows how the attenuation profiles can be filtered into giving a clean cross section image showed in d).[46].

shades of gray than those with lower density. CT has a wide range of applications in carbon materials, such as density measurements, crack detection, pore distribution and consumption inspection. Picard [47] showed how CT could determine the apparent density of the carbon anodes, and gave examples of how CT can be used to detect cracking in carbon anodes.

2.8.2 Electron Probe Micro-Analysis

Electron Probe Micro-Analysis (EPMA) is an analytical instrument used for imaging at high magnification, as well as determining the composition of small areas on samples.

EPMA images are produced by directing a focused beam of electrons onto a sample. The interaction between the sample and the electron beam yields both X-ray photons and derivative electrons (either secondary electrons or backscattered electrons). The derivative electrons can be used for high magnification imaging in the same manner as in scanning electron microscopy (SEM), and for imaging of carbon materials, backscattered electrons are the most efficient. This type of imaging shows each phase in different gray scales depending on their atomic number (Z), or mean atomic number (Z_{mean}) for compounds such as SiC. With higher atomic number, the number of backscattered electrons increase and the element/compound is shown brighter. [48]. The emitted X-ray photons are characteristic of the different elements in the sample, and can thus be used to identify what elements the investigated part of the sample contains [48]. Figure 2.30 shows the setup of an EPMA instrument.

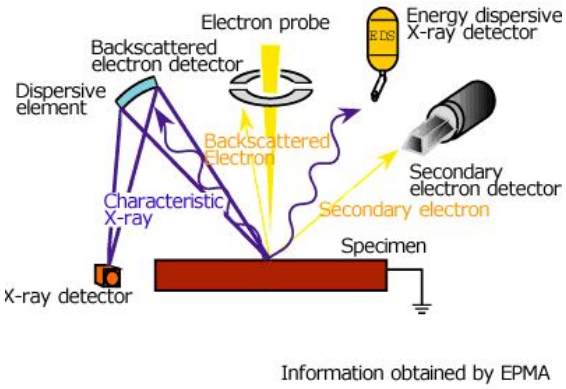

Figure 2.30: Illustration of an EMPA instrument, and the emitted electrons and x-ray photons.[49].

EPMA itself is a non-desutructive method of analysis, but it requires small sample sizes and can only be used to investigate the surface of a sample. To investigate the interior of larger samples, the samples would have to be cut into smaller pieces.

Chapter 3

Experimental

The purpose of the experimental work presented in this report was to investigate the mechanisms of wear in carbon lining samples subjected to silicon at elevated temperatures. An illustration of the experimental process is given in figure 3.1.

Figure 3.1: Illustration of the experimental process.

Two different types of furnaces were used to expose carbon lining samples to silicon. This was done to investigate whether choice of furnace affected wear of the lining samples. Six samples were exposed to silicon using the same induction furnace as in the experiments for the preliminary project work [5], while three samples were exposed to silicon using an electric resistance heated furnace.

In most of the experiments, a slag consisting of Al_2O_3, CaO and SiO_2 was added, and in five of the experiments the temperature was cycled to see whether the intrusion and wear was affected by the solidification of silicon. To investigate the wear of the carbon lining, the lining samples were scanned using X-ray computed tomography (CT) both before and after exposure to silicon. After the last scanning using CT, the samples were investigated using Electron Probe Micro-Analysis (EPMA).

Experiments were also performed to investigate the wetting and intrusion of silicon on anthracite and binder phase separately. These were performed in a sessile drop furnace in argon atmosphere, and the results were investigated using EPMA.

3.1 Raw materials

The silicon used in the experimental work was provided by Elkem Thamshavn, and the carbon lining paste was provided by Elkem Carbon AS. The lining samples used in the experiments were made in the laboratories of Elkem Carbon Kristiansand.

3.1.1 Si

The silicon used in the experimental work was provided in two separate batches, and an analysis of the Si was performed by Elkem Thamshavn. The impurity content of the silicon is given in table 3.1.

Table 3.1: Analysis of Si metal used in the experimental work.

	Element	Batch A	Batch B
%	Si	99.22	99.46
%	Al	0.151	0.084
%	Ca	0.037	0.010
%	Fe	0.447	0.306
%	Ti	0.028	0.021

It is noted that the two batches are very similar, and it will not be specified which batch that has been used in the different experiments.

3.1.2 Slag

In some of the experiments, a slag consisting of Al_2O_3, CaO and SiO_2 was added to the liquid silicon. The slag was added both to investigate carbon lining wear caused by the slag, but also to prevent oxidation of the liquid silicon. To prevent oxidation, two prerequisites were obtained for the slag; it had to melt at the lowest temperature possible, while still ensuring that the slag density was kept below the density of liquid silicon. To obtain an early melting slag with low density, a composition of 65% SiO_2, 20% CaO and 15% Al_2O_3 was chosen. This composition gives a liquidus temperature of 1170°C and density below 2.30 g/cm^3. Figure 3.2 shows the phase diagrams with liquidus temperatures and density for the Al_2O_3, CaO and SiO_2 system. The slag composition used in this experimental work has been marked with a red dot in the phase diagrams.

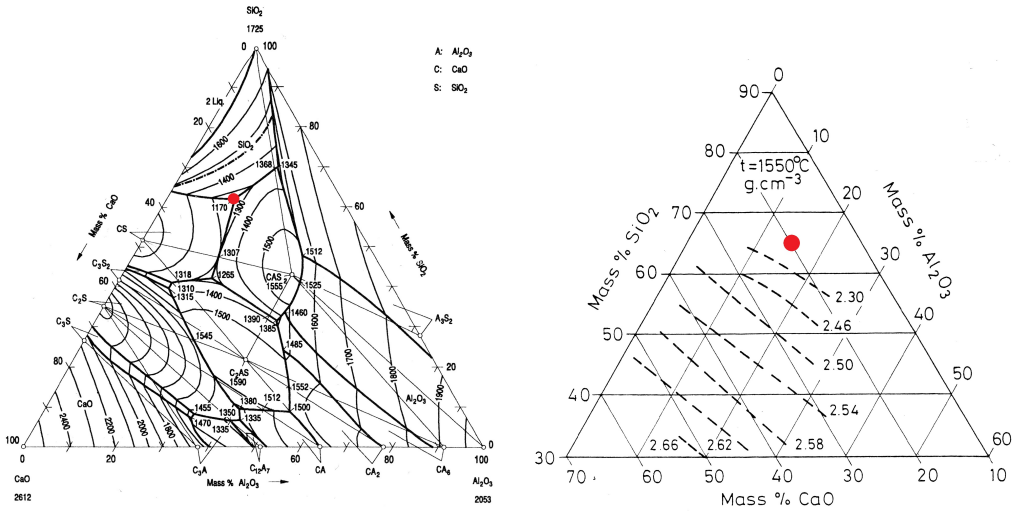

(a) Liquidus temperatures **(b)** Density

Figure 3.2: Phase diagrams with liquidus temperatures and densities for the Al_2O_3, CaO and SiO_2 system, where the experimental slag composition has been marked.

3.1.3 Carbon lining

The carbon linings used in the experimental work for this report are different types of cold ramming paste linings. The carbon lining pastes were provided by Elkem Carbon AS, and pastes with three different types of binder were provided; tar pitch, resin and eco binder.

The first lining type used in the experiments is an anthracite based paste with tar pitch as the binder phase. This paste was produced by Elkem Carbon during February 2015 and formed and baked in July 2015. Two different sample types were prepared from this paste, see figure 3.3.

The samples in figure 3.3a were produced by ramming 4 layers of approximately 6-6.5 cm each in a 23x58 cm steel crate, with a total height of 26 cm. The ramming was performed with a star shaped ramming head. After baking at 600°C for 120 minutes then 950°C for an additional 120 minutes, 2 sylindrical samples of Ø50mm were drilled vertically from the rammed lump of lining paste, giving the samples sketched in figure 3.3a. Two such samples were made, and named V4 and V5. Sample V2 and V3, used in the project work performed prior to this report [5], were produced in the same manner.

The samples in figure 3.3b were formed using 100 strokes at 25°C in a Fischer-

Sandrammer, before baking at 950° for 120 minutes. The Fischer-Sandrammer applies even force across the entire cross section of the sample, providing a solid, cylindrical sample. These cylindrical samples have a diameter of approximately 50 mm with height varying from 56-58 mm. Four such samples were produced and named FS4, FS5, FS6 and FS7. Sample FS1, FS2 and FS3 which was used in the project work [5] were produced in the same manner.

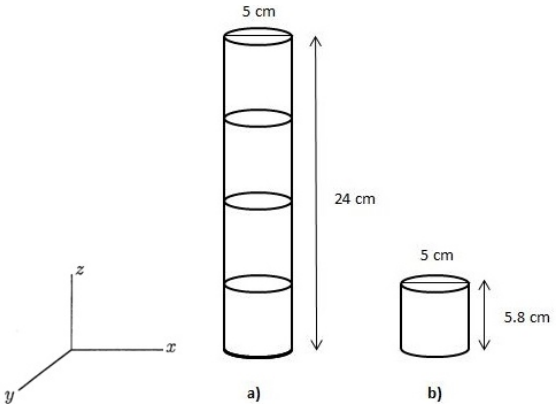

Figure 3.3: Sample structure for a) layered samples V4 and V5, and b) Fischer-Sandrammer samples FS4, FS5, FS6 and FS7. The axes defined in the figure applies for the rest of the report.

An additional set of samples was prepared by Elkem Carbon in January 2016. These samples were prepared from an anthracite based paste using eco binder as the binder phase, which is free from harmful substances such as polyaromatic hydrocarbons. These samples were also added small fractions of solid silicon along with the anthracite fractions. The samples were prepared using the same preparation technique as for the layered samples V4 and V5, but were prepared with thinner layers of approximately 2 cm and by using a flat ramming head. Same as for sample V4 and V5, the samples were prepared as part of a bigger lump in a steel crate and baked using the same temperature profile as for the layered tar pitch samples. After baking, two cylindrical samples of approximately 16-17 cm height and 5 cm diameter were cut from the big lump, and named V6 and V7.

One last sample was produced using resin as the binder phase, and by ramming down layers of carbon paste in a steel crate. This lump was made with thicker layers of approximately 9 cm. Apart from the different binders, this sample was produced using the same preparation technique as sample V4 and V5, with the star shaped ramming head. The lump of carbon paste with resin binder was baked faster than the other two types of layered samples, with a heating rate of approxi-

mately 60°C/hour and with a maximum temperature of 1500° after only 24 hours. After baking, a small sample with 60 mm diameter and 82 mm height was cut from the middle of the larger sample, and named V8. This sample contains only one layer and no layer transitions, but will still be defined as a layered sample due to the preparation technique.

The baking temperature profiles for the FS samples and the different layered samples are given in figure 3.4.

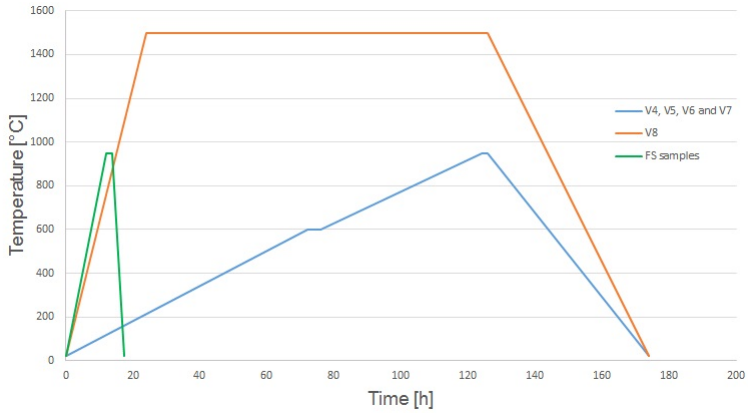

Figure 3.4: Baking program used for the FS samples compared with the program for the layered samples with tar pitch binder.

An overview of the samples for the experimental work is given in table 3.2, which shows the binder phase, structure and average density, ρ_{ave}, for each of the samples. The average density was calculated after measuring the sample volume and weight.

Table 3.2: Sample overview, with sample binder phase, structure and average density, ρ_{ave}.

Sample no.	Binder phase	Structure	$\rho_{ave}[\frac{kg}{m^3}]$
$FS4$	Tar pitch	Solid	1443
$FS5$	Tar pitch	Solid	1434
$FS6$	Tar pitch	Solid	1442
$FS7$	Tar pitch	Solid	1436
$V4$	Tar pitch	Layered	1439
$V5$	Tar pitch	Layered	1442
$V6$	Eco	Layered	1441
$V7$	Eco	Layered	1440
$V8$	Resin	Layered	1441

3.2 Experimental work

Experiments subjecting carbon lining to liquid silicon were performed in a resistance heated furnace, an induction furnace, and a sessile drop furnace. The experiments in the resistance heated furnace and the induction furnace were performed to investigate wear mechanisms of the lining, primarily chemical wear, densification and spalling. In the sessile drop furnace, the wetting and intrusion of silicon was investigated on pure anthracite, binder phase and carbon lining samples.

3.2.1 Entech resistance heated furnace

Three of the carbon lining samples, FS4, FS5 and FS6, were exposed to liquid silicon using an Entech resistance heated furnace. The furnace is top loaded and isolated with oxide bricks both in the side walls and the bottom of the furnace. The furnace was used with the top lid open, and the top was isolated with large pieces of kaowool. Figure 3.5 shows an image of the resistance furnace used in these experiments.

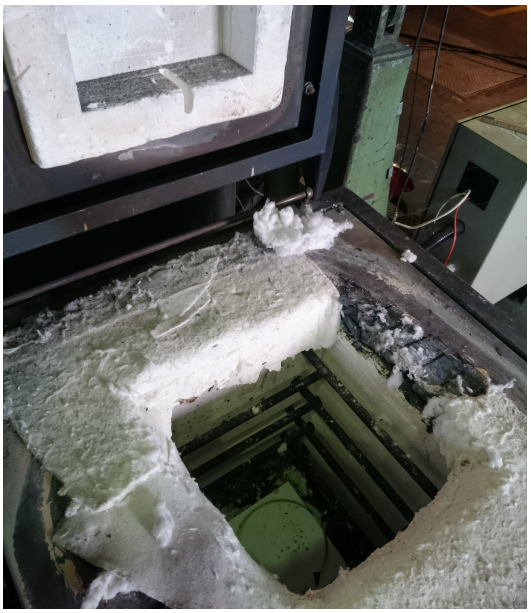

Figure 3.5: Image of the Entech electric resistance heated furnace used in the experiments.

Carbon lining samples and silicon or silicon+slag were placed in a graphite crucible and heated from room temperature to 1500°C. A graphite rod was attached to each carbon lining sample to make the process of removing the samples from

the liquid silicon easier. Threads were made on the bottom part of the graphite rod, and threaded holes were drilled into the top 1.5 cm of each sample. A sketch of the experimental setup in the resistance heated furnace is provided in figure 3.6.

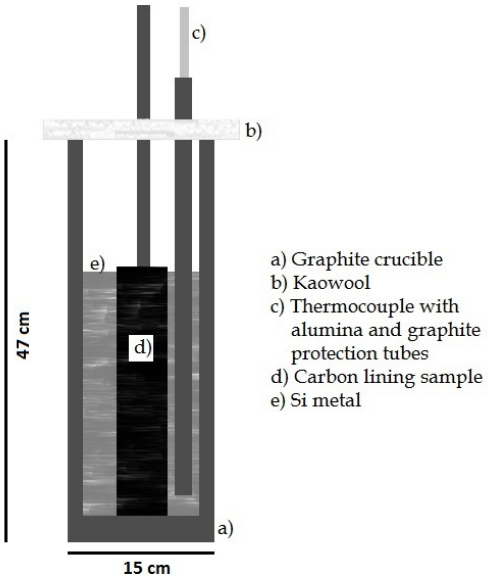

Figure 3.6: Sketch of the experimental setup used for silicon exposure in the electric resistance heated furnace.

The temperature was recorded using a thermocouple protected by an alumina tube and a graphite tube. This was placed in the metal bath, approximately 1 cm above the graphite crucible bottom, and in equal distance to both the carbon lining sample and the crucible wall. Figure 3.7 shows the experimental setup seen from above.

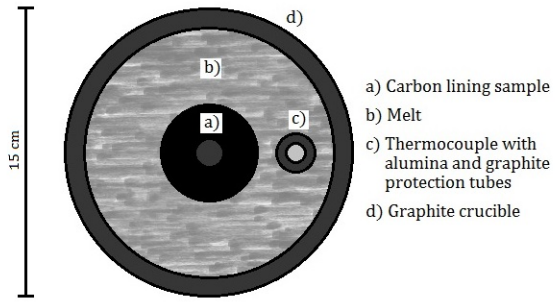

Figure 3.7: Sketch of the experimental setup used for silicon exposure in the electric resistance heated furnace, seen from above.

Table 3.3 gives an overview of the experiments performed in the Entech resistance heated furnace. A total of 3 FS samples were heated from room temperature to 1500°C as quickly as possible. The 3 experiments in the Entech furnace were performed with different crucible content and/or holding times at 1500°C, which is shown in table 3.3.

Table 3.3: Overview of experiments performed in Entech resistance heated furnace.

Sample no.	Crucible content	Holding time [min]
$FS4$	Silicon	45
$FS5$	Silicon	60
$FS6$	Si + slag	60

Some modifications to the furnace were made between the experiment with sample FS4 and sample FS5. The furnace bottom was built higher using oxide bricks, elevating the crucible with 5 cm and ensuring that the kaowool fully covered the crucible opening, and an additional lid was put on top of the crucible. This was done to prevent oxygen flow into the crucible and decrease oxidation of the furnace content. For the third experiment in the Entech furnace, slag was added to the crucible. The composition of the slag is given in section 3.1.2, and part of the motivation behind adding the slag was, again, to reduce oxidation.

The heating rate in the resistance heated furnace was set to the maximum of the furnace capacity, giving various heating rates depending on the furnace temperature. The heating rate from room temperature to 1000°C was consistent at approximately 25 °C/min, while the heating rate from 1000°C to 1300°C was just below 10°C/min. Above this temperature, the heating rate slowed significantly, and as the temperature reached 1450°C, the heating rate fell below 1°C/min. The low heating rate was probably due to heat loss to the surroundings from the furnace working chamber, and to the low maximum furnace temperature of approximately 1520°C. Due to the slow heating rate, the holding time of 60 minutes was started as the temperature reached 1450°C, not 1500°C as planned. Figure 3.8a shows the temperature logs from the experiments performed in the Entech furnace.

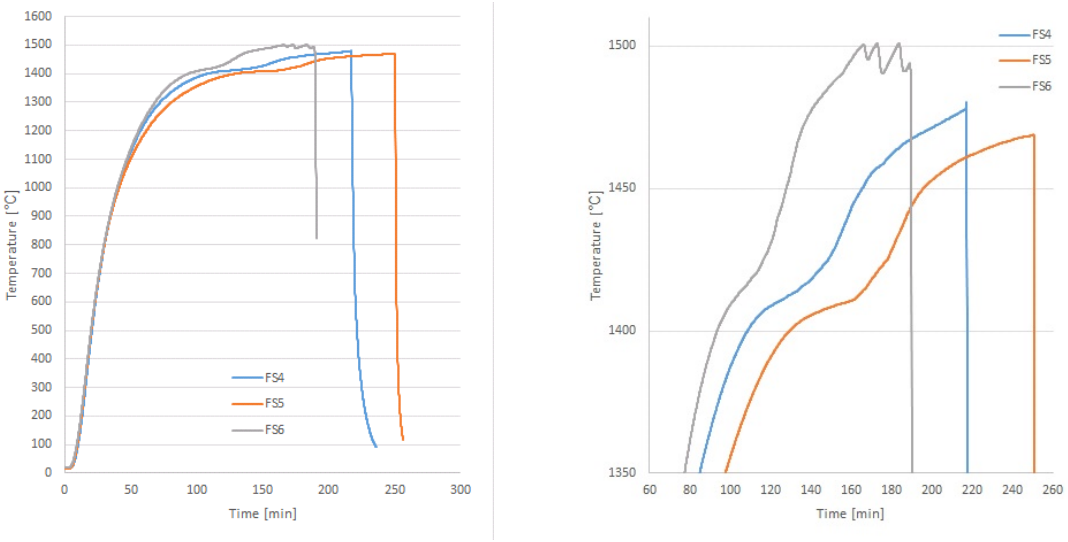

(a) From room temperature to 1500° **(b)** From 1350° to 1500°

Figure 3.8: Temperature profile for the Entech resistance heated furnace heating Si or Si+slag, and carbon samples FS4, FS5 and FS6.

3.2.2 IF-75 induction furnace

Another set of experiments subjecting carbon lining samples to silicon and slag were performed using the IF-75 induction furnace. The experimental setup was the same as in figure 3.6 and 3.7 in section 3.2.1, and figure 3.9 shows an image of the induction furnace used in these experiments.

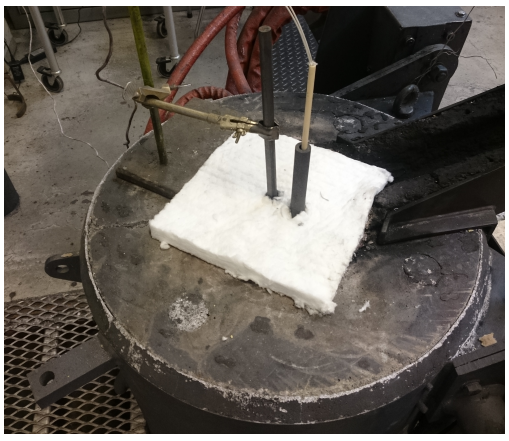

Figure 3.9: Image of the induction furnace IF-75 used in the experimental work.

The last Fischer-Sandrammer sample, sample FS7, was heated from room temperature to 1500°C using the induction furnace, and held at this temperature for 60 minutes. The sample was submerged in silicon and slag, and the slag composition is given in section 3.1.2. These were the same conditions as for sample FS6 in the Entech resistance heated furnace, with the exception of the heating rate. The heating rate in the induction furnace experiment was kept constant at 40°C/min, and the temperature log from silicon exposure of sample FS7 in IF-75 is given in figure 3.10. The graph also shows the temperature log from the Entech experiment with sample FS6 for comparison, and it is observed that the heating rate is much faster in the induction furnace, espesially above 1000°C.

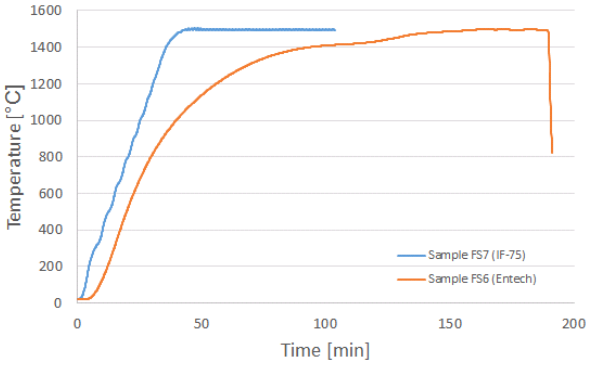

Figure 3.10: Temperature profile for the induction furnace IF-75 heating sample FS7 and silicon+slag, compared with the experiment heating sample FS6 and silicon+slag using the Entech furnace.

Layered samples V4 and V8 were exposed to silicon and slag while the temperature was cycled around the solidification temperature of silicon (1416°C[7]). This temperature cycling was performed to investigate the effect from the solidification of silicon on the intrusion and wear of the sample. The heating rate for these two experiments was kept constant at 40°C/min up to 1600°C. The temerature was held here for 10 minutes before dropping by 20°C/min down to 1350°C. The temperature was again raised by 40°C/min to 1600°C, before it was dropped down to 1350°C, again by decreasing the temperature with 20°C/min. To be able to remove the sample from the crucible, the temperature was increased above the melting temperature one last time, before terminating the experiment. The temperature log from the two experiments is given in figure 3.11. It is noted that the cooling and heating rate halts at around 1412-1420°C for both experiments. This is due to the melting and solidification of the silicon in the crucible. It is also noted that this temperature stagnation is shorter for sample V8 than for V4, probably due to the fact that sample V8 is a smaller sample with less silicon in the crucible.

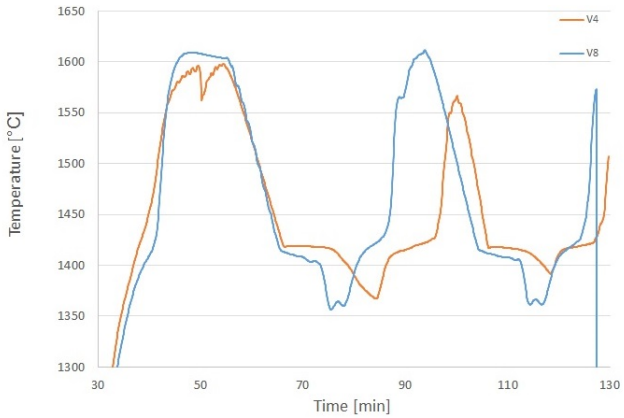

Figure 3.11: Temperature logs from experiments with sample V4 and V8 in silicon and slag.

Sample V5 and V6 were also subjected to silicon and slag in the induction furnace, this time while cycling the temperature above the solidification temperature of silicon, between 1600°C and 1450°C. Sample V7 was subjected to the same temperature profile, but only to silicon, not slag. The temperature profile for these three experiments is given in figure 3.12, along with the temperature profile for the experiment with sample V8 for comparison. It is noted that the heating and cooling rates are the same as for the experiment with sample V8, and that the only difference is the selected holding temperatures.

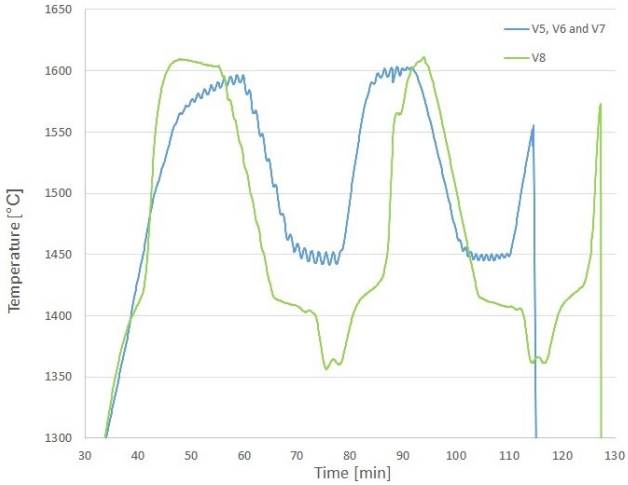

Figure 3.12: Temperature log from experiments with sample V5, V6 and V7 compared with the temperature log from the experiment with sample V8.

The temperature cycling above the solidification temperature of silicon shown in figure 3.12 gave the opportunity to investigate the effect from the temperature cycling without the added effect from the solidification of silicon. Individual temperature logs for sample V5, V6 and V7 are given in figure A.1 in appendix A. It is noted that the temperature logs are very similar for the three experiments, which indicates that the furnace follows the programmed temperature profile consistently.

An overview of all the experiments performed in the Entech resistance heated furnace and the induction furnace IF-75 is given in table 3.4. This shows the furnace, temperature profile and crucible content for each sample.

Table 3.4: Overview of experiments performed in the Entech resistance heated furnace and induction furnace IF-75.

Sample no.	Furnace	Crucible content	Temperature profile
$FS4$	Entech	Silicon	1475°C, 45 min
$FS5$	Entech	Silicon	1475°C, 60 min
$FS6$	Entech	Si + slag	1500°C, 60 min
$FS7$	IF-75	Si + slag	1500°C, 60 min
$V4$	IF-75	Si + slag	Cycling: 1600°C to 1350°C
$V5$	IF-75	Si + slag	Cycling: 1600°C to 1450°C
$V6$	IF-75	Si + slag	Cycling: 1600°C to 1450°C
$V7$	IF-75	Si	Cycling: 1600°C to 1450°C
$V8$	IF-75	Si + slag	Cycling: 1600°C to 1350°C

3.2.3 Sessile drop furnace

Sessile drop furnaces are small scale furnaces used for wetting and intrusion experiments. The sessile drop and the substrate are both heated by conduction from graphite heating elements inside the furnace, in the same way as in a large resistance heated furnace; as the graphite elements are heated, heat is conducted to the sessile drop and substrate. Experiments in sessile drop furnaces are often performed using shielding gas to control the gaseous environment. Figure 3.13 shows a sketch of the sessile drop furnace used in this experimental work.

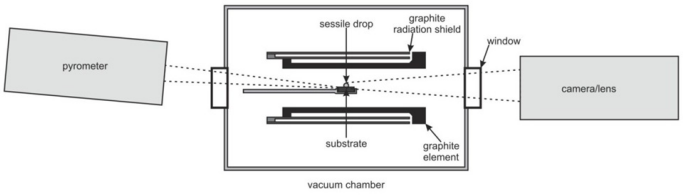

Figure 3.13: Illustration of a sessile drop furnace setup [37].

Experiments investigating the wetting and intrusion of silicon on carbon lining substrates were performed in a sessile drop furnace. In these experiments, three sets of substrates were used;

- Baked carbon lining paste (anthracite + binder)
- Calcined anthracite grains
- Baked binder phase with only fine carbon solid particles ($<800\mu$m)

These substrates were chosen to compare the wetting and intrusion of silicon on the carbon lining in this type of furnace, as well as investigating differences in wetting and intrusion between the different constituents in the baked carbon lining paste.

The anthracite substrate was produced by grinding down an anthracite grain to a disc of approximately 3 mm height and 10 mm diameter. The other two substrates were cut to the same measurements directly from baked paste, where one substrate was cut from an area with very few anthracite grains (to represent the binder phase) while the other was chosen from an area with both grains and binder-phase representative for the sample average. All the substrates were polished to avoid open cracks and pores running completely though the substrate.

The silicon used for the sessile drop was cut into cubes of approximately 2x2x2 mm and cleaned in hydrofluoric acid (HF) to avoid any oxide formation at the silicon surface.

The experiments in the sessile drop furnace were performed using argon as shielding gas. The heating rate was kept at 300°C/min up to 1000°C, and then at 50°C to 1420°C. After this, the temperature was increased by 5°C/min. For the experiment using pure anthracite as the substrate, the temperature was increased up to 1480°C, where the temperature was held until the experiment was terminated. The experiment with the binder phase and fine solid particles followed the same temperature profile. For the experiment using carbon lining, the experiment was terminated shortly after melting of the silicon due to uncontrolled and vigorous movement of the silicon. The temperature profiles are given in figure 3.14.

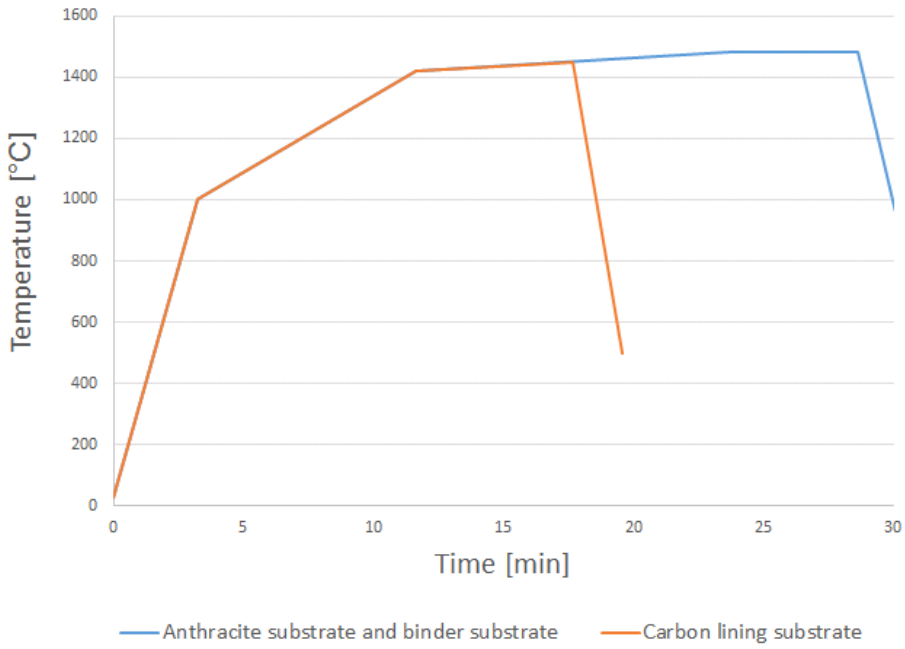

Figure 3.14: Temperature profiles for the sessile drop furnace experiments.

3.3 Sample analysis

3.3.1 X-ray Computed Tomography

Both before and after exposure to silicon, the carbon lining samples were scanned using X-ray computed tomography (CT).

The scans were performed with a Nikon XT H225 ST, and the settings for the imaging were 130kV and 115μA. To create the final CT images, three different software programs from Nikon Metrology were used; Inspect-X (controls the x-ray generator, sample table and image collecting), CTPro3D (edits the parameter files for reconstruction of CT images) and CT Agent (reconstructs the CT images). After reconstruction, the images were exported into the program ImageJ for cropping, translation and rotation to make the scans taken before exposure to silicon match the ones taken after experiments in IF-75 and the Entech furnace.

Due to the height of the layered samples, V4 and V5 had to be scanned in three sections and V6 and V7 in two sections, where each section covered 8 cm of the samples. For the FS samples and layered sample V8, the required quality for the scans could be obtained by scanning the full sample height in one scan.

3.3.2 EPMA

Electron probe micro-analysis (EPMA) was performed on samples from the induction furnace, the resistance furnace and the wetting furnace. The purpose of using EPMA was to investigate the wetting, intrusion and chemical reaction between the liquid silicon+slag and the carbon lining samples.

In order to investigate the carbon lining samples using EPMA, the samples had to be cut into smaller pieces. The FS samples were cut into semi cylinders before sectioned into smaller pieces as shown in figure 3.15a. The layered samples where first cut into discs before each disc was cut into smaller pieces, as shown in figure 3.15b. The sessile drop samples were cast in epoxy, then cut into semi cylinders.

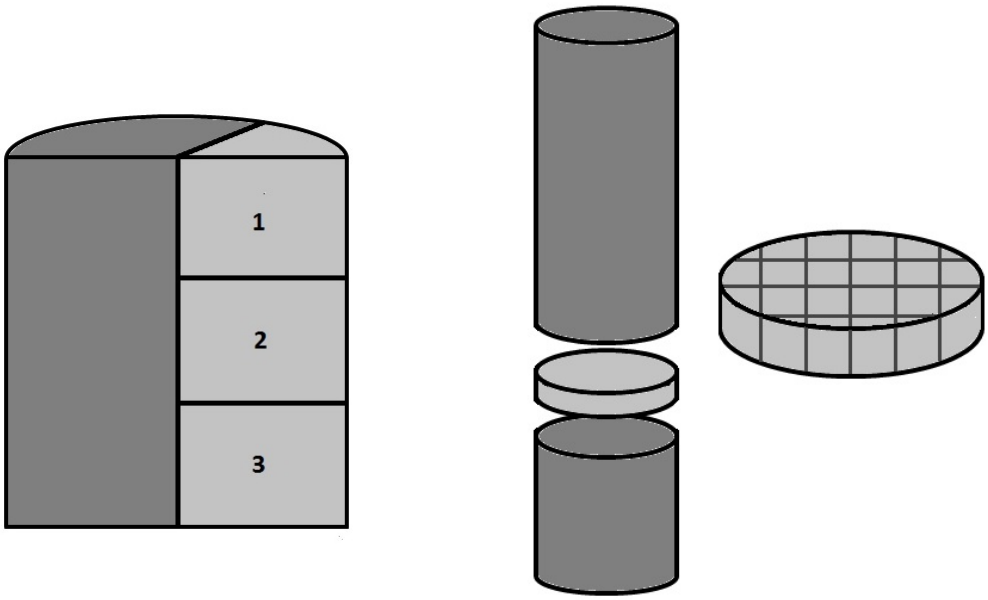

(a) FS samples **(b)** Layered samples

Figure 3.15: Sectioning of carbon lining samples for EPMA investigation.

Table 3.5 shows an overview of the samples investigated using EPMA. The numbers on the FS samples refer to the numbers shown in figure 3.15.

Table 3.5: Analysis of Si metal used in induction furnace experiments.

Sample no.	Section	No.
FS4	Surface	2
FS5	Surface	3
FS6	Surface	2
FS7	Surface	2
V4	Surface + interior	-
V5	Surface + interior	-
V6	Surface + interior	-
V7	Surface + interior	-
V8	Surface + interior	-
Anthracite substrate	Whole sample	-
Binder substrate	Whole sample	-
Paste substrate	Whole sample	-

All the carbon lining pieces were cast in epoxy, to make sylinders with diameters

of 25 mm and height of approximately 15 mm. These samples were grinded and polished down to 1 μm, before coating the samples with carbon to ensure a conductive surface over the whole sample. Figure 3.16 shows an image of one of the finished samples for EPMA.

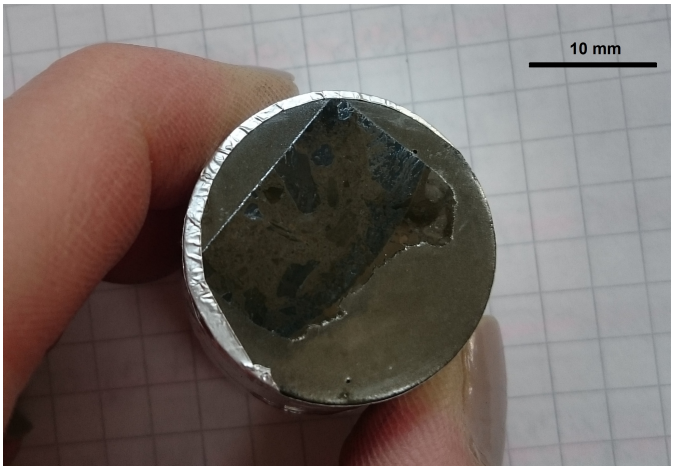

Figure 3.16: Prepped sample for EPMA.

All images captured using the EPMA were aqquired using the backscattered electrons, while the characteristic X-ray photons were used for the element mapping and point analyses. As mentioned in section 2.8 in the theory chapter, backscattered electron images show different phases in different shades of gray depending on their atomic number. Table 3.6 shows an overview of the different elements and compounds that can be found in the samples, sorted from brightest in the images (highest Z or Z_{mean}) to darkest.

Table 3.6: Atomic number, Z_{mean}, for all elements and compounds found in the experiments.

Element/compound	Z_{mean}	Brightness
Iron	26	Brightest
Silicon	14	-
Slag	11.9	-
SiO_2	10.8	-
SiC	8.4	-
Carbon	6	Darkest

Chapter 4

Results

This chapter presents the results from the CT scans performed prior to silicon exposure, as well as the results from the experimental work in the induction furnace, resistance heated furnace and sessile drop furnace. After the furnace experiments the samples were investigated using both CT (X-ray computed tomography) and EPMA (electron probe micro-analysis).

4.1 CT prior to silicon exposure

All samples except those used in the sessile drop furnace were scanned using CT prior to the furnace experiments. Four different types of samples were used; Fischer-Sandrammer samples with tar pitch binder, layered samples with tar pitch binder, layered samples with eco binder and layered samples with resin binder.

4.1.1 Layered samples with tar pitch binder

CT images performed on the layered samples with tar pitch binder prior to silicon exposure show that the average density of each cross section varies across the height of the sample. This can be seen from figure 4.1, which shows the orthogonal view of sample V4 in X-Z direction. By processing the CT scans using the ImageJ software, an average density for each cross section can be obtained. These values have been calculated for each cross section and plotted as a function of height in the sample, and this plot can be seen in the right hand side of figure 4.1. The maximum density value found in the sample is measured at the top of the top layer, with an average cross section density of 1448 kg/m^3, while the lowest cross section density, which is measured to 1435 kg/m^3, is found in the bottom of the second-bottom layer. This gives a density variation of 13 kg/m^3.

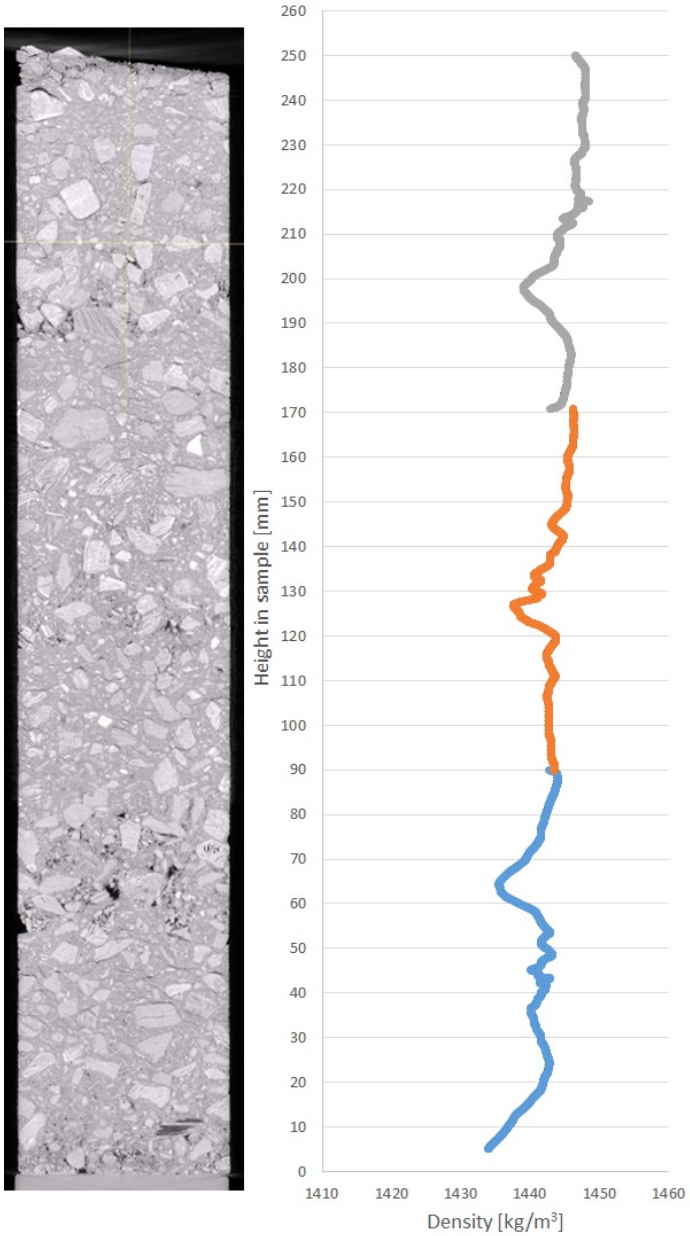

Figure 4.1: Orthogonal view of sample V4 in X-Z direction, and average cross section density as a function of height in the sample.

Transitions between layers can be seen at approximately 65 mm, 125 mm and 200mm. It is assumed that the less dense packing at 60-70 mm, 120-130 mm and 195-205 mm is the bottom of each ramming layer, and that the more densely packed areas directly below, at 55 mm, 120 mm and 185 mm, are the tops of the next layers.

Similar calculations and images can be obtained for sample V5, and are shown in figure 4.2. The left hand side shows the orthogonal view in X-Z direction, while the right hand side shows the average cross section densities as a function of height in the sample. In this sample, layer transition areas can be observed at approximately 65 mm, 125 mm and 200 mm.

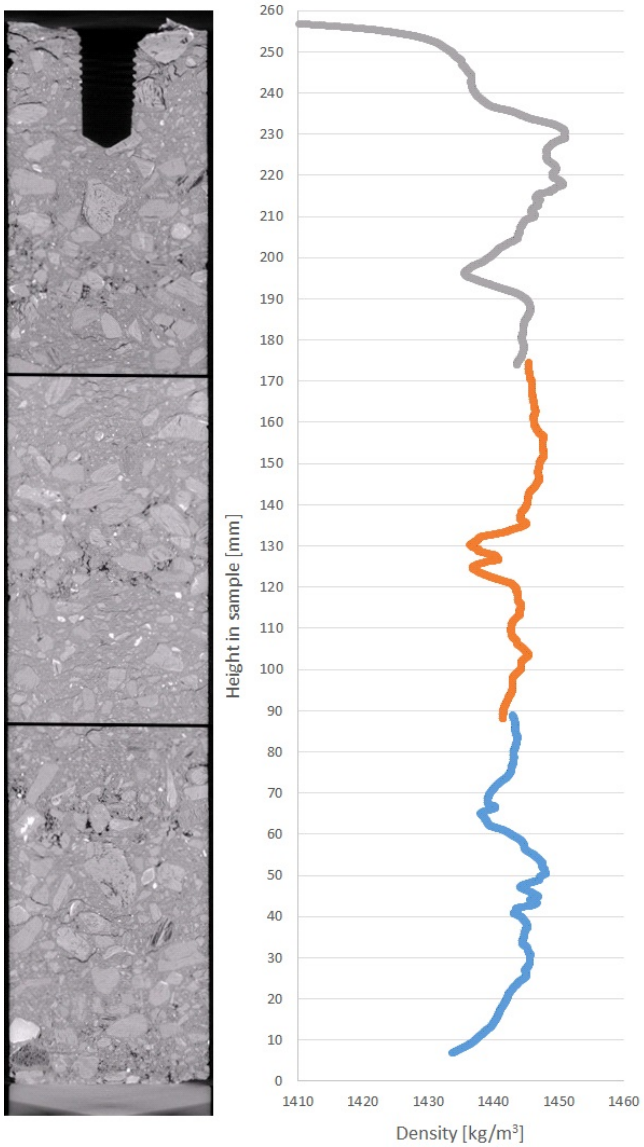

Figure 4.2: Orthogonal view of sample V5 in X-Z direction, and average cross section density as a function of height in the sample.

Figure 4.2 shows that the maximum density in sample V5 is in the top of the top layer, where the average cross section density is 1451 kg/m^3. Unlike sample V4, the lowest density is found at the bottom of the top layer, not towards the bottom of the sample. The measured minimum density found in this area is 1436 kg/m^3, which gives a difference of 15 kg/m^3. It is noted that the CT cannom measure the density at the bottom of the sample. This is the case for the density measurements in all of the samples.

The density difference between the porous bottom of each layer and the rest of the sample is also clear in the cross section images. Figure 4.3 shows the difference between the packing mid layer, and towards the bottom of a layer in sample V4.

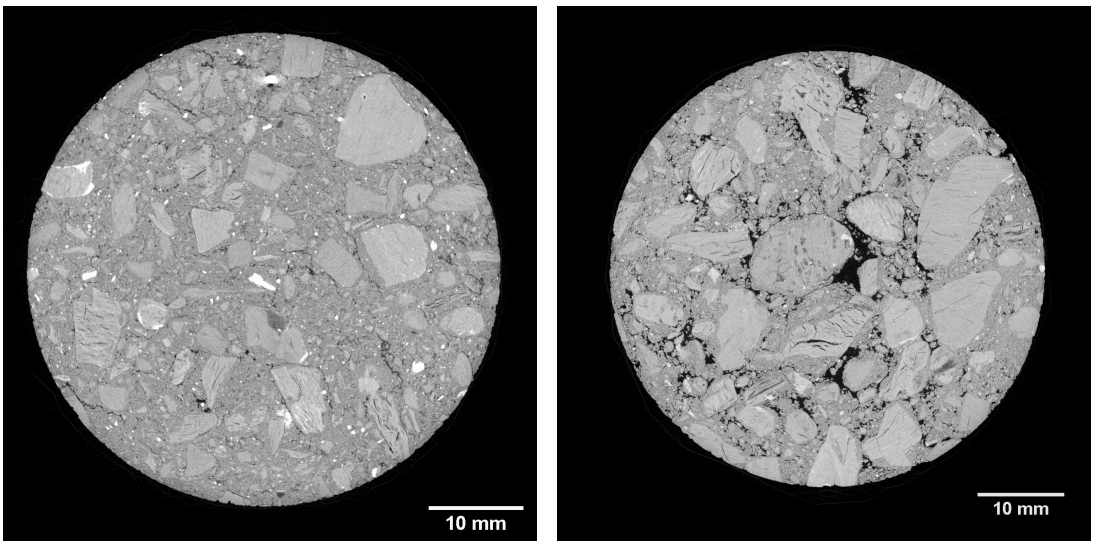

(a) Mid layer, 5 cm into sample **(b)** Bottom of layer, 6.2 cm into sample

Figure 4.3: Difference in packing from middle section of layer to bottom section of layer in sample V4.

It is also observed that there seems to be an accumulation of larger anthracite grains in the bottom of the ramming layers in sample V4 and V5, compared with the distribution over the rest of the layer height.

In addition to these density variations, it is also observed that all the grains in some areas of both sample V4 and V5 are broken and crushed. It is noted that these areas always occur right below the porous areas, and it is assumed that these areas are the top of each ramming layer. The most severe grain crushing is observed in the top 2 mm of each ramming layer. Figure 4.4 and 4.5 show grain crushing in the top of the ramming layers in sample V4 and sample V5, respectively.

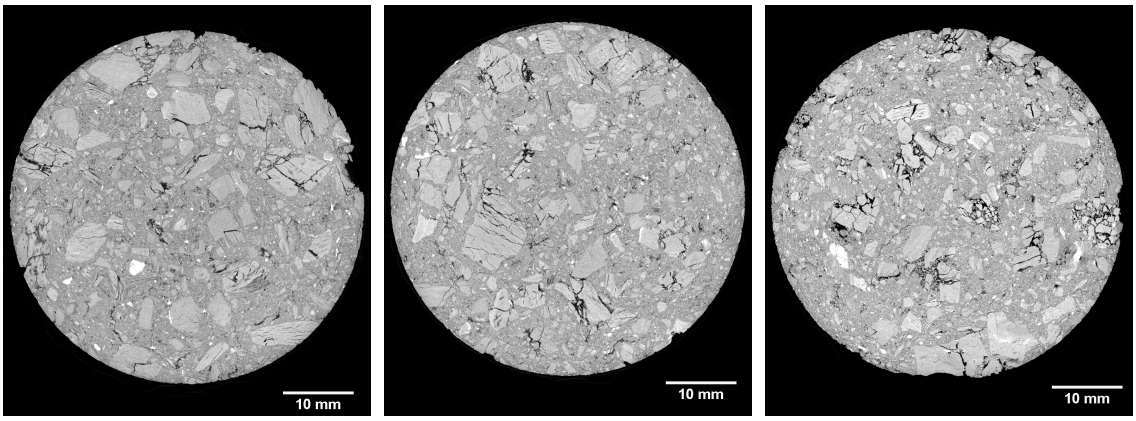

(a) V4 - layer 1 **(b)** V4 - layer 2 **(c)** V4 - layer 3

Figure 4.4: Crushed grains in the top 2 mm of ramming layers from layered sample V4.

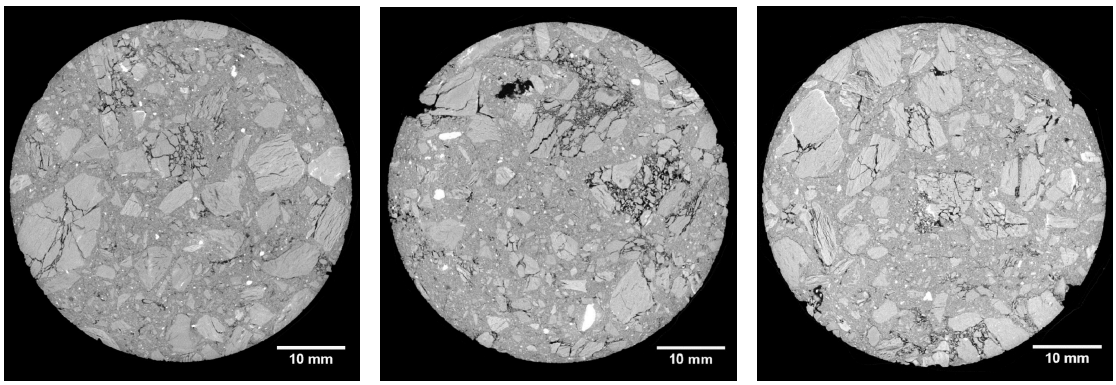

(a) V5 - layer 1 **(b)** V5 - layer 2 **(c)** V5 - layer 3

Figure 4.5: Crushed grains in the top 2 mm of ramming layers from layered sample V5.

Formation of cracks can be observed in the layered samples V4 and V5, as can be seen in figure 4.6. The observed cracks are very narrow, and the length of the cracks varies from 5 mm to cracks running through almost the entire sample in X or Y direction. The cracks seem randomly distributed, and do not depend on the layering of the samples.

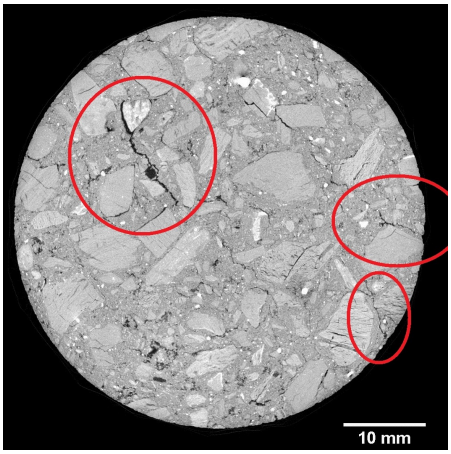

(a) Sample V4

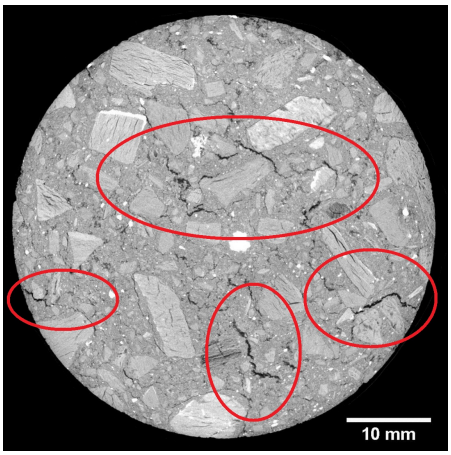

(b) Sample V5

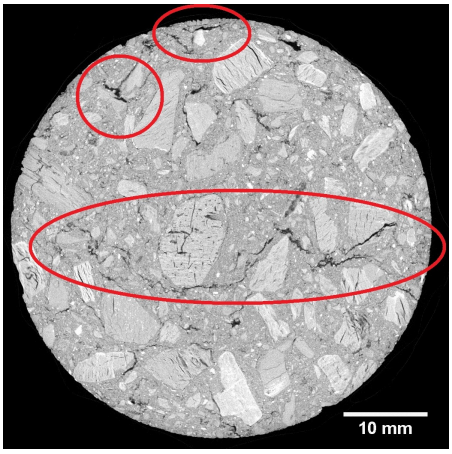

(c) Sample V5

Figure 4.6: Cracks in layered samples V4 and V5.

4.1.2 Layered samples with eco binder

Sample V6 and V7, produced with PAH free eco binder and layers of approximately 2 cm, were scanned and processed in the same manner as sample V4 and V5. It is noted that the CT scan does not include the top 3 cm of both samples.

Figure 4.7 shows the orthogonal view in X-Z direction for sample V6 and V7, as well as the calculated cross section densities as a function of height in the sample. When inspecting the orthogonal view in X-Z direction along with the cross section densities, it is observed that the density variations seems periodical and dependent on the layers. Similar to the assumption made for sample V4 and V5, it is assumed that the areas with decreased density are the bottom of the ramming layers, where the packing of the paste is less dense.

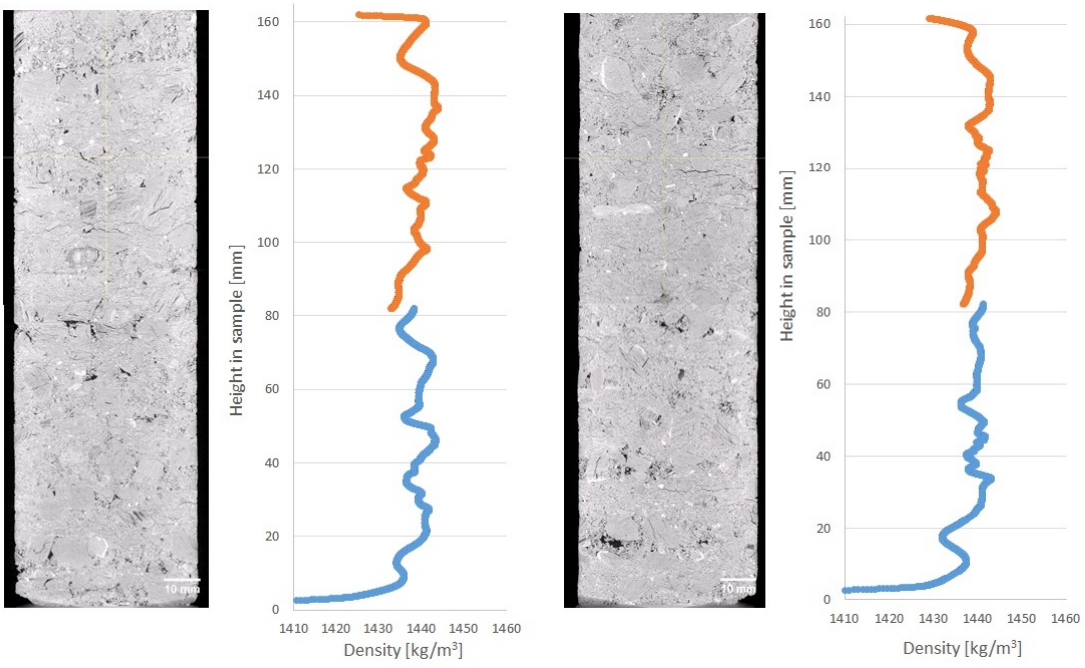

(a) Sample V6 **(b)** Sample V7

Figure 4.7: Orthogonal view in X-Z direction and average cross section densities across the sample height of sample V6 and V7.

The highest cross section density in sample V6 is detected in the top of the top layer, where the cross section density is measured to 1444 kg/m^3. In sample V7, the highest cross section density is found in the top of the second-bottom layer,

where the measured density is 1443 kg/m^3. In both of the samples, the lowest cross section density is found in the bottom of the second bottom layer, where the density is measured to 1434 kg/m^3 for sample V6 and 1433 kg/m^3 for sample V7. That makes the maximum-minimum difference of the two samples equal, with a value of 10 kg/m^3. No significant accumulation of anthracite grains can be observed in these samples.

From the CT scans, it is also noted that the difference in density between the anthracite grains and the binder phase area is significantly less in sample V6 and V7, with eco binder, than for sample V4 and V5 with tar pitch binder. Figure 4.8 compares cross section images from sample V5 and sample V7. This indicates that the density of the binder phase, and the very fine fractions of solid mixed in the binder, is higher in sample V6 and V7 compared with the tar pitch samples.

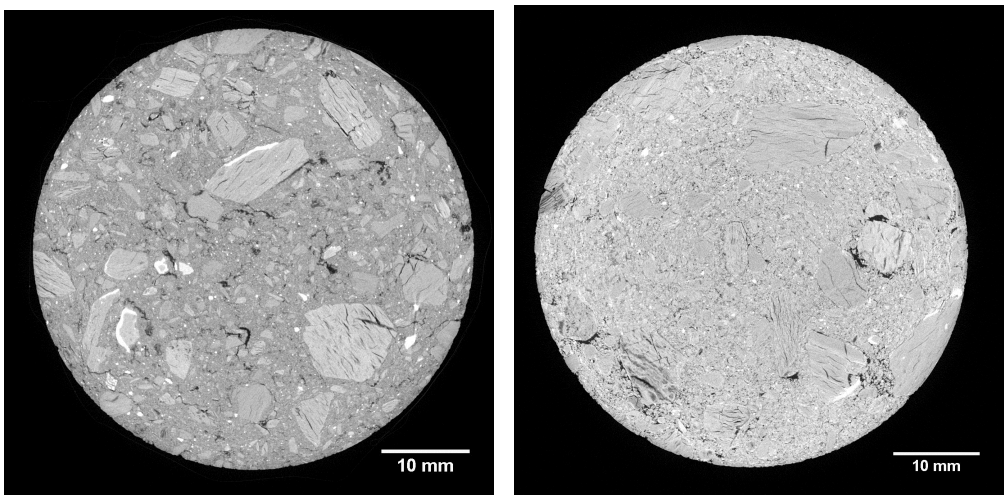

(a) Sample V5 **(b)** Sample V7

Figure 4.8: Cross sections from sample V5 with tar pitch binder and sample V7 with eco binder.

Unlike the observations from sample V4 and V5, only very limited grain crushing can be observed in sample V6 and V7. Even in the areas directly below the layer bottoms with decreased density, where the paste has been subjected to direct ramming, only a few of the grains have been crushed by the ramming procedure. It is noted that the ramming of sample V4 and V5 was preformed with a star shaped ramming head, while the ramming head used for preparation of sample V6 and V7 was completely flat. Figure 4.9a and 4.9b show the most significant grain crushing found in sample V6 and V7 respectivly, while figure 4.9c shows grain crushing in sample V5 for comparison.

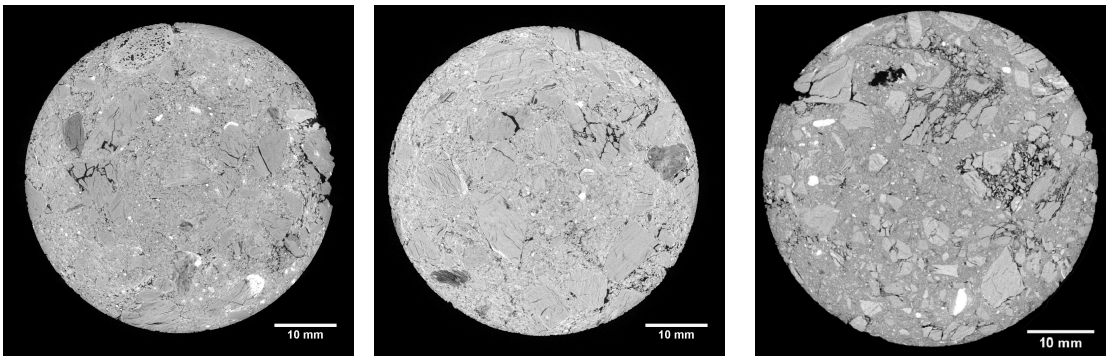

(a) V6 **(b)** V7 **(c)** V5

Figure 4.9: Grain crushing in sample V6, V7 and V5.

In sample V6 and V7, some formation of cracks could be observed. The cracks observed in the eco binder samples were randomly distributed in the samples, and fewer cracks were observed in sample V6 and V7 compared with sample V4 and V5. Figure 4.10 shows examples of cracks in sample V6 and V7.

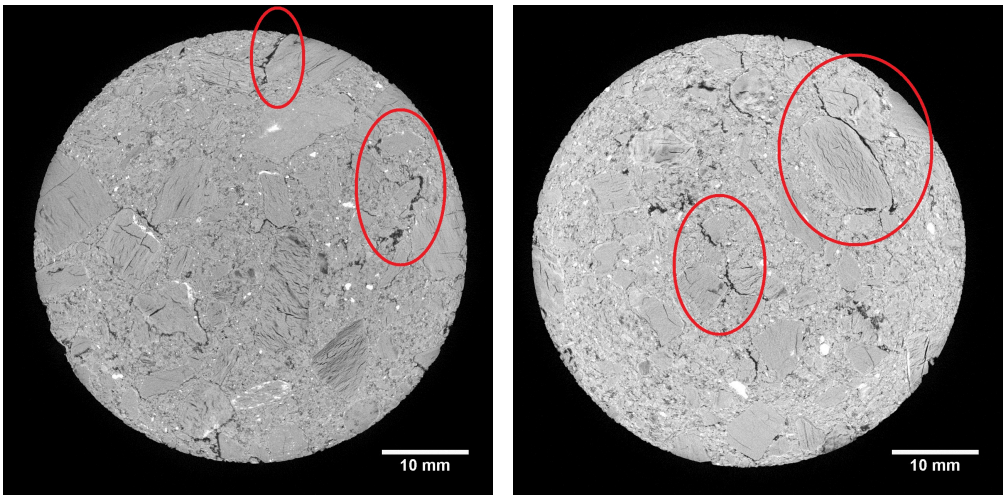

(a) Sample V6 **(b)** Sample V7

Figure 4.10: Cracks in sample V6 and sample V7.

4.1.3 Layered sample with resin binder

Sample V8, which was produced with resin as the binder phase, was prepared using the same ramming technique as for the layered samples V4-V7, but with only one layer of approximately 8.2 mm height and 60 mm diameter. It has, due to the preparation, been defined as a layered sample in this report.

In sample V8, it is observed that the density decreases towards the bottom of the sample. This can be seen from figure 4.11, which shows the orthogonal view in X-Z direction as well as the average cross section densities across the sample height. In this sample, the density varies from 1452 kg/m^3 at the top of the sample to 1436 kg/m^3 in the bottom of the sample, the largest variation found in any of the layered samples.

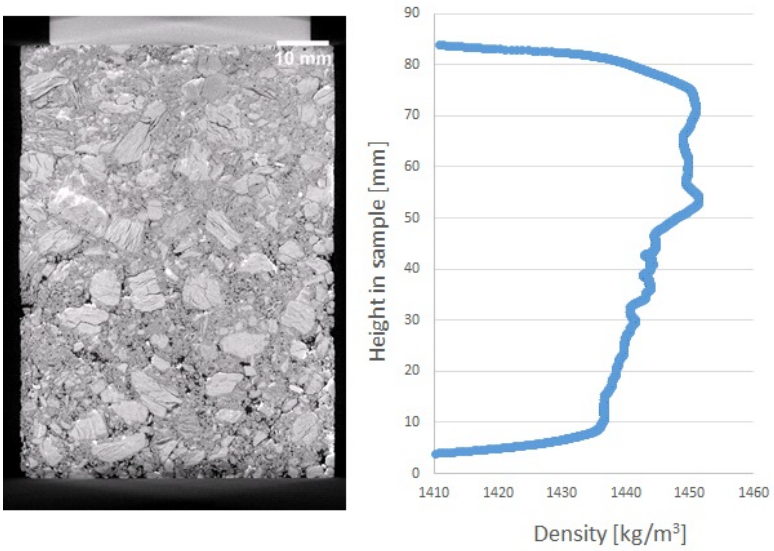

Figure 4.11: Orthogonal view of sample V8 in X-Z direction, and average cross section density as a funtion of height in the sample.

From the orthogonal view, it is noted that no significant accumulation of the larger anthracite grains is observed in sample V8.

It is also observed that the density of the binder phase resembles the density of the tar pitch binder more than the eco binder. This is shown in figure 4.12, which shows cross section images of samples with the three different binders, V5, V7 and V8. From this, it is observed that the resin binder has a distinct difference

in density compared with the anthracite, similar to the observations made in the samples with tar pitch binder.

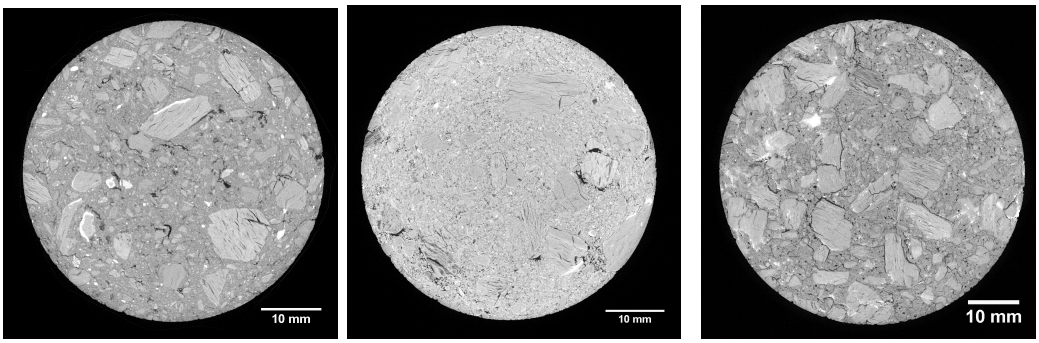

(a) V5 **(b)** V7 **(c)** V8

Figure 4.12: Cross section images from V5 (tar pitch), V7 (eco binder) and V8 (resin binder).

No signifigant cracks were observed in sample V8, but some crushing of the grains in the top 2-3 mm is observed. This is shown in figure 4.13a. Another area with a few crushed grains can be observed 5.4 cm from the bottom of the sample, and a cross section image from this area is shown in figure 4.13b. The reason for the crushed grains in the middle of sample V8 has not been determined.

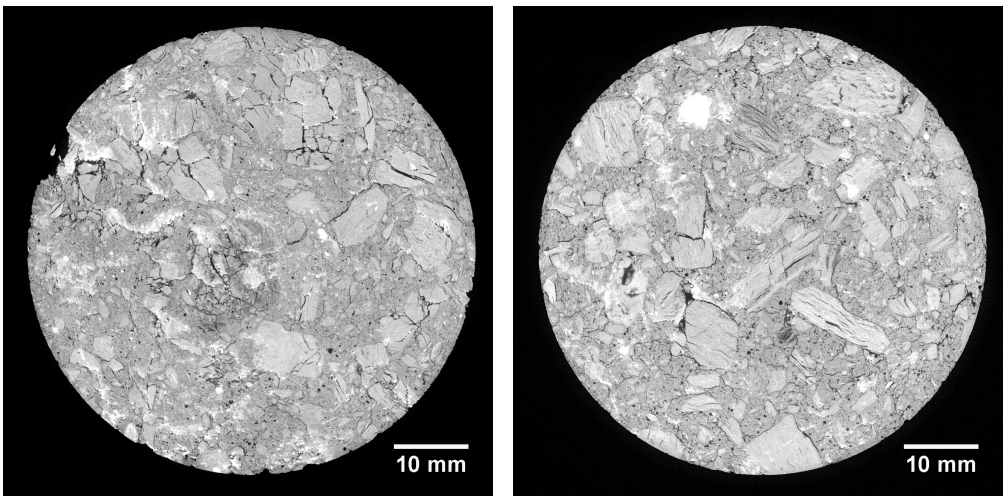

(a) Top of sample **(b)** 54 mm into sample

Figure 4.13: Crushed grains in sample V8.

4.1.4 Fischer-Sandrammer samples

The Fischer-Sandrammer samples were prepared by filling carbon paste in a cylindrical mold before applying 100 strokes evenly across the entire cylinder. This gave solid samples without any layering. The FS samples were prepared from the same tar pitch based paste as the layered samples V4 and V5.

CT images from the Fischer-Sandrammer samples FS4, FS5, FS6 and FS7 show that the internal morphology of these samples does not vary across the height of the samples, as it does for the layered samples. Some variation across the height of the samples can be seen in figure 4.14 showing the orthogonal view in X-Z direction and the average cross section densities, but these variations seem to be random and not dependent on position in the sample.

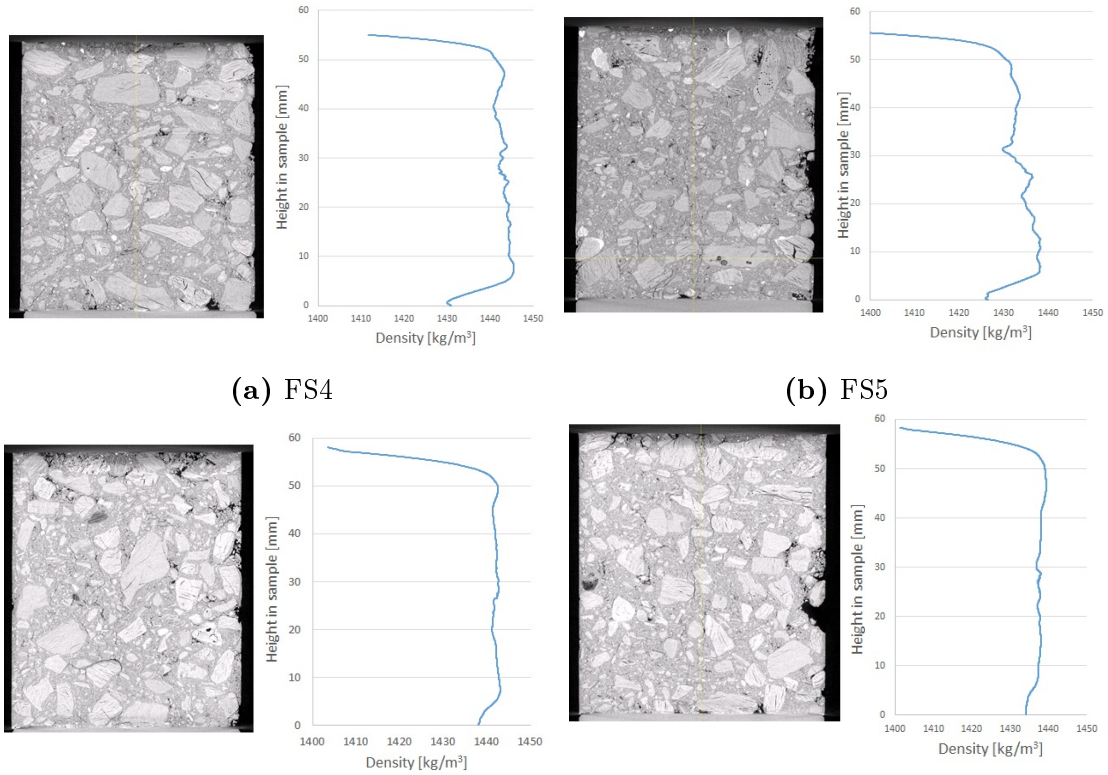

(a) FS4 **(b)** FS5

(c) FS6 **(d)** FS7

Figure 4.14: Orthogonal views and average cross section densities for samples FS4, FS5, FS6 and FS7.

Allthough no density trend could be observed across the height of the FS samples, in the Z direction, they all seem to have varying densities in the X-Y direction. Figure 4.15 shows cross section images from all of the FS samples, and it is observed that the larger grains have accumulated in the right hand side of the samples, making this side slightly more porous than the left hand side of the samples.

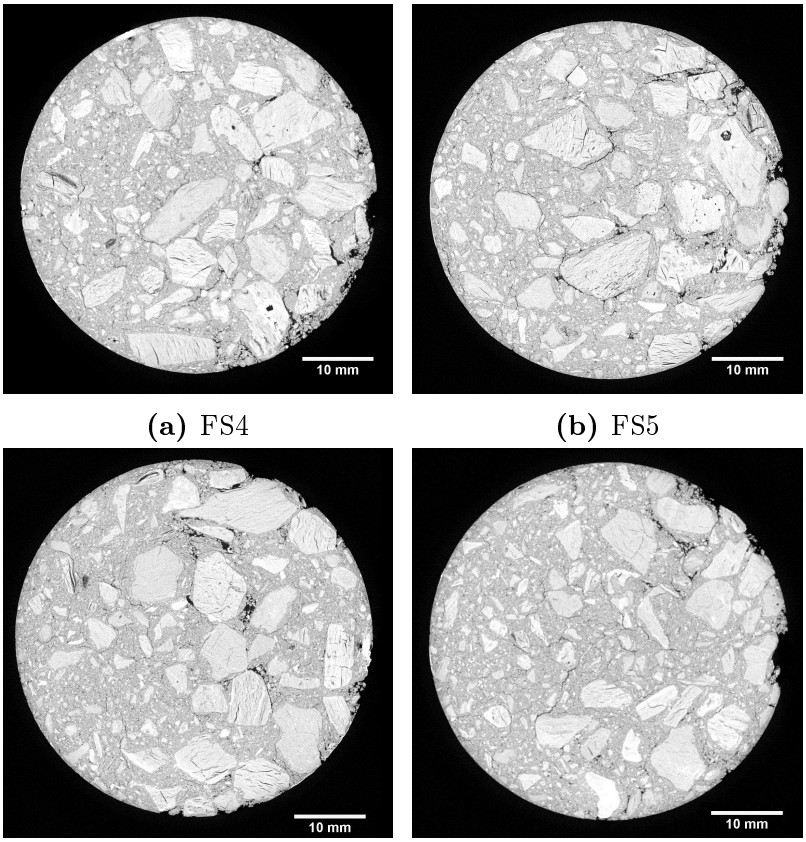

(a) FS4 **(b)** FS5

(c) FS6 **(d)** FS7

Figure 4.15: Cross section images from sample FS4, FS5, FS6 and FS7, which all show segregation to different extents.

The FS samples do not show the same extent of grain crushing, and hardly any broken grains are found in the samples. Similar to the layered samples V4 and V5, which contain the same paste as the FS samples, cracks can also be found randomly distributed in the FS samples. Some examples are given in figure 4.16.

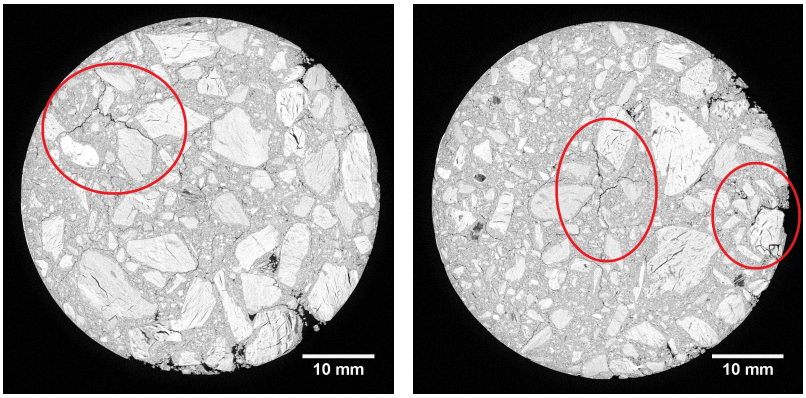

(a) FS4 **(b)** FS5

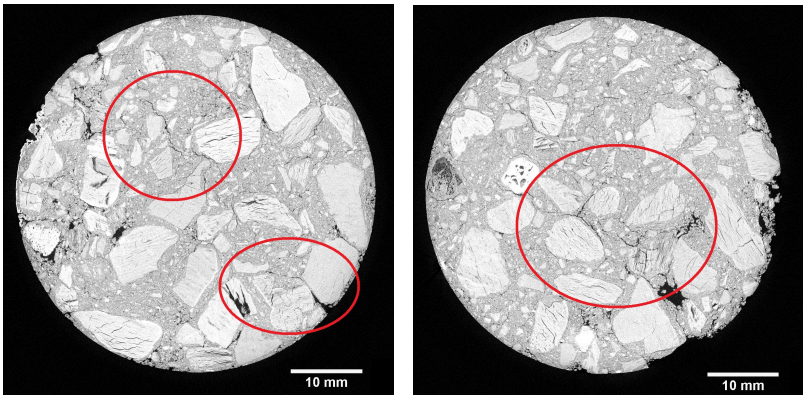

(c) FS6 **(d)** FS7

Figure 4.16: Cross section images from sample FS4, FS5, FS6 and FS7, showing cracks in the FS samples.

4.2 Induction furnace experiments

4.2.1 Sample FS7

Sample FS7 was subjected to silicon and slag using the induction furnace IF-75. The sample and silicon+slag was heated rapidly to 1500° and held at that temperature for 60 minutes without any temperature cycling.

From the visual inspection of FS7, it is observed that the silicon and slag looks completely melted, and that wetting between the molten silicon and the carbon lining sample seems very good. It is observed that some unmelted furnace content lies on the sample surface as lumps, and it is assumed that this is a slag crust. From the images it looks as though the top part of the sample, which has not been in contact with slag or silicon, is unreacted except for some oxidation of the carbon by the air flow in the crucible. Figure 4.17 shows images of sample FS7 after the induction furnace experiment.

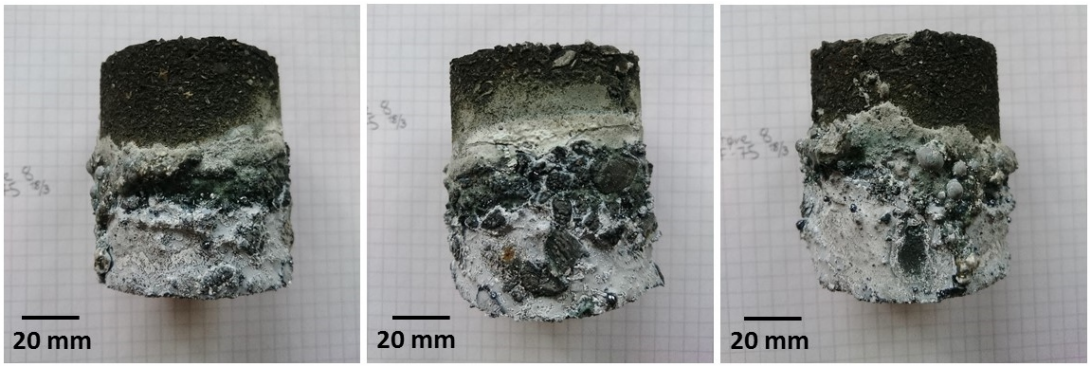

Figure 4.17: Visual inspection of sample FS7 in different views, after exposure to liquid silicon and slag in the induction furnace.

When inspecting sample FS7 using CT, the same observations as by visual inspection can be made; wetting between the furnace content and the carbon lining looks good, and the lower half of the sample has been covered during the experiment. Allthough the wetting has been almost complete, no intrusion or reaction is visible from the orthogonal views showed in figure 4.18. It is also noticed that no particular difference between the slag and the silicon can be seen in these CT images. This was the case in all the CT images performed after exposure to silicon and slag.

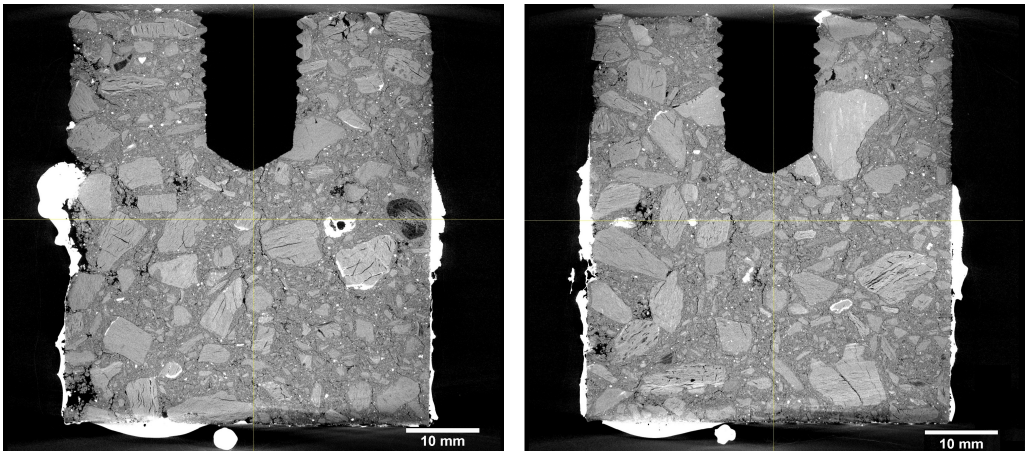

(a) X-Z direction **(b)** Y-Z direction

Figure 4.18: Orthogonal views in X-Z and Y-Z direction of sample FS7 after exposure to silicon in the induction furnace.

From the X-Y cross section images, it is again observed that wetting between the furnace content and the sample surface has been very good. Figure 4.19 shows cross sections from 0.5 cm and 2 cm from the bottom of sample FS7, which shows that the furnace content completely covers the sample surface.

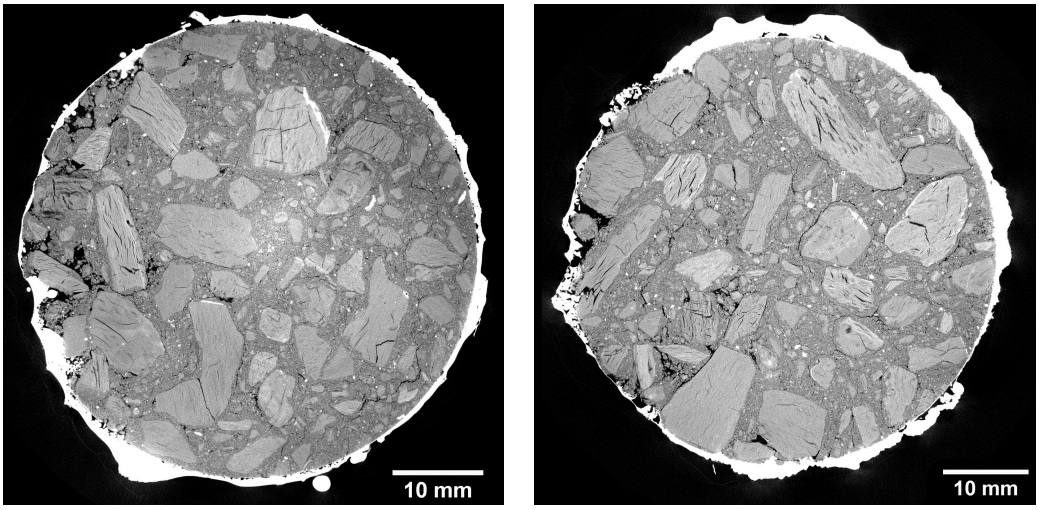

(a) 5 mm into sample **(b)** 20 mm into sample

Figure 4.19: X-Y cross section images from 0.5 cm and 2 cm into sample FS7.

From the bottom part of figure 4.19b, it is also observed that the furnace content has completely wetted the inside of pores with openings towards the surface. This

section is showed in higher magnification in figure 4.20, along with the CT scan of the same section before exposure to silicon and slag. From this figure, it is observed that no expansion of the pores seem to have occurred.

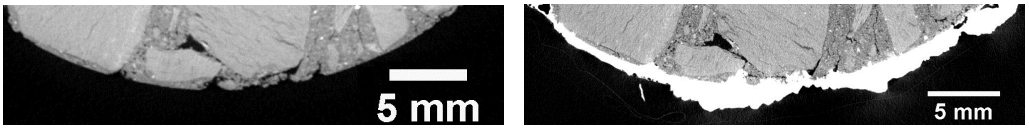

(a) Before furnace experiment **(b)** After furnace experiment

Figure 4.20: Magnified image of the bottom part of image 4.19b.

From the inspection of sample FS7 using backscattered electron imaging in EPMA, no intrusion could be detected, only wetting of larger surface pores. In addition, the carbon lining looks unreacted, and no converted layer of the lining could be observed on the sample surface. This can be seen in figure 4.21, which shows the carbon lining surface surrounded by three different phases. Analyses performed on the three different furnace constituents show that the sample has been surrounded by slag and silicon, and that areas with silicon dioxide is observed. It is also observed that only slag is in direct contact wth the sample surface. An analysis of the slag was performed in the position of the red number 1, and the results from this are given in table B.1 in appendix B. This shows that the slag consists of Al_2O_3, CaO and SiO_2, whith very small amounts of iron.

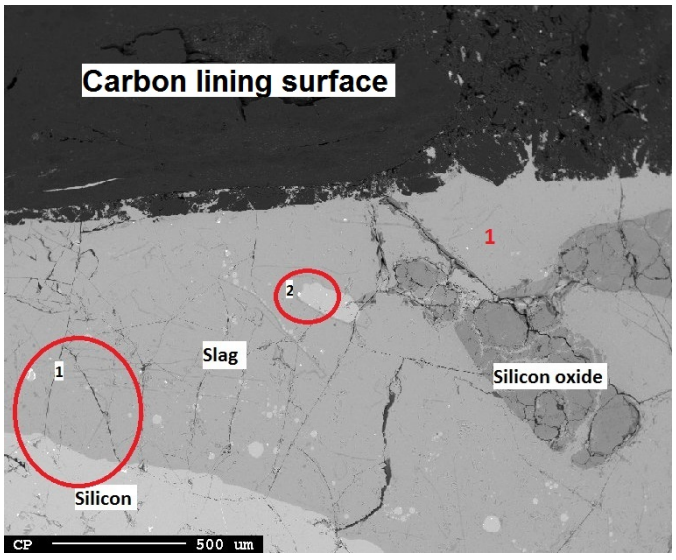

Figure 4.21: EPMA image from FS7 sample surface and surrounding furnace content.

In figure 4.22, the two circled sections from figure 4.21 are shown in higher magnification. Section 1 was mapped using emitted X-ray photons, showing that the darker threads that can be found in the slag are silicon carbide threads. This mapping is shown in figure 4.23.

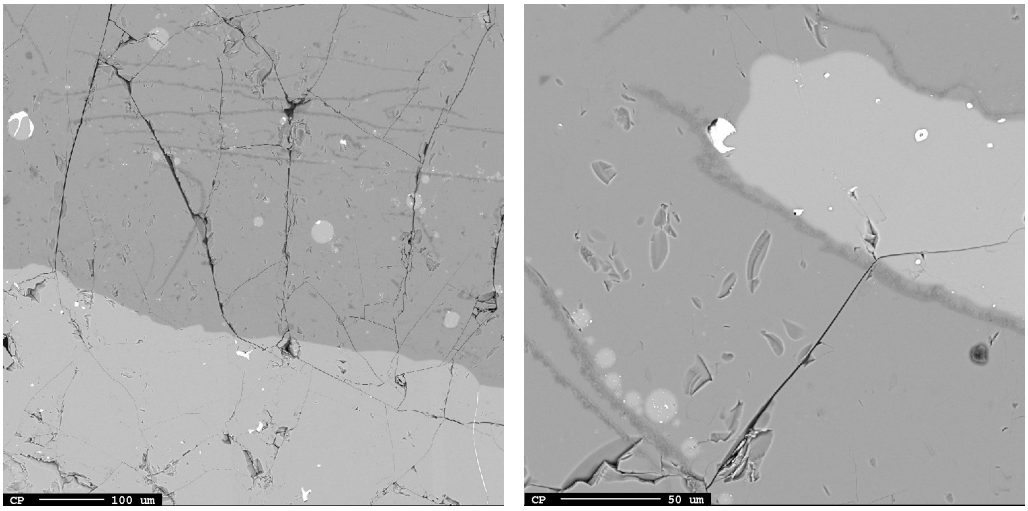

(a) Section 1 **(b)** Section 2

Figure 4.22: EPMA images from the surrounding furnace content of sample FS7.

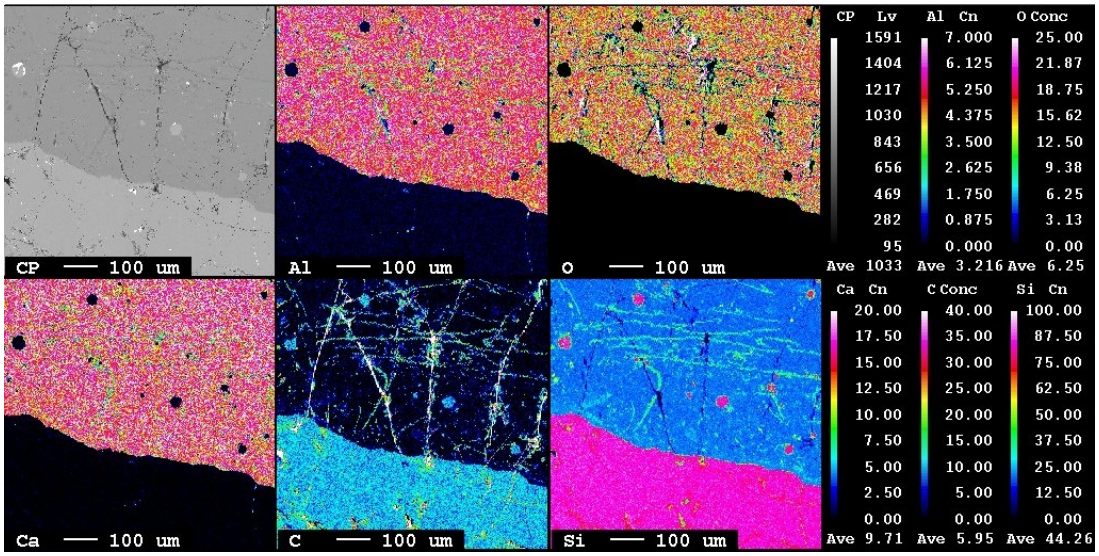

Figure 4.23: X-ray mapping of section 1 (figure 4.22a).

4.2.2 Sample V4

Sample V4 was made with the same tar pitch paste as sample FS7, with 4 layers of approximately 6 cm each. This sample was exposed to silicon and slag using the induction furnace, and the temperature was cycled twice between 1600°C and 1350°C. This allowed the silicon to solidify three times during the experiment.

The visual inspection of this sample shows that the top half of this sample has not been exposed to the silicon or slag, and heavy oxidation of the carbon lining sample in this area is observed. The top half of figure 4.24 shows an image of the entire sample, while the three images below show the bottom half which has been subjected to slag and silicon.

Figure 4.24: Visual inspection of sample V4 in different views, after exposure to silicon and slag in the induction furnace.

The CT scans from the layered sample V4 performed after the experimental work in IF-75 show drastic changes in the densisty of the sample interior. Figure 4.25 shows the orthogonal view in Y-Z and X-Z direction of the silicon covered part of sample V4.

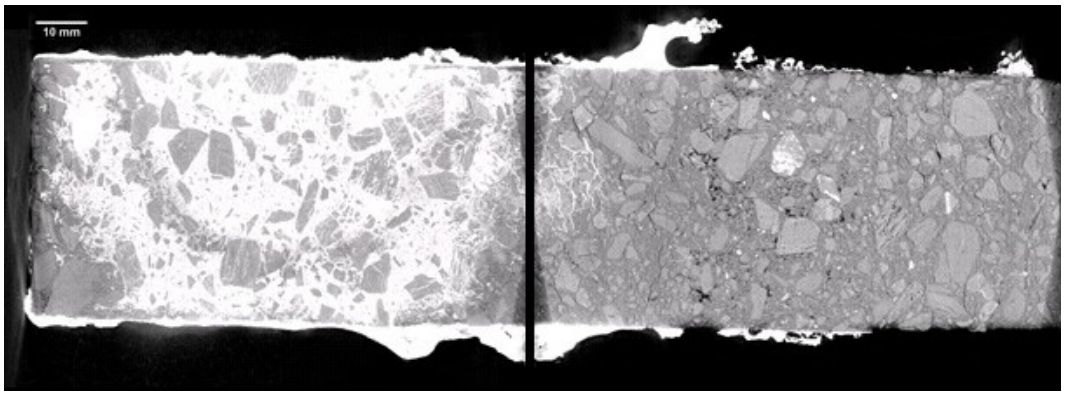

(a) X-Z direction

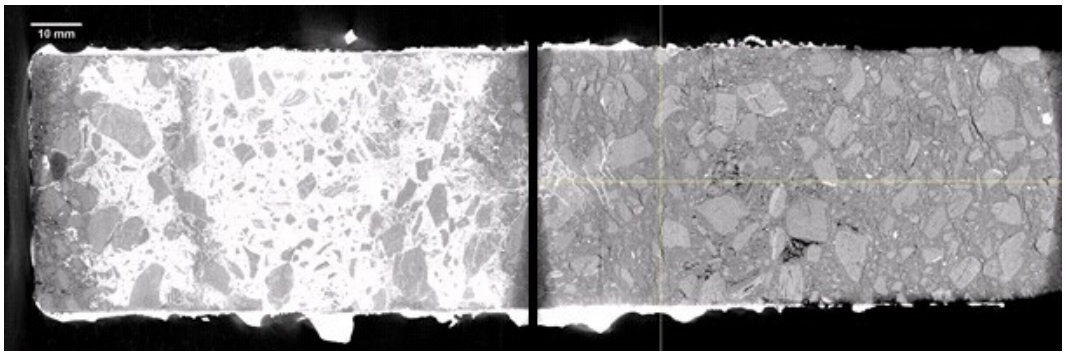

(b) Y-Z direction

Figure 4.25: Orthogonal views of sample V4 after exposure to silicon and slag. The black line marks the transition between two separate scannings, and will be found in all the orthogonal views of the layered samples except sample V8.

From these scans, it can be seen that the lower half of sample V4 has been perfectly wetted by the liquid silicon and slag, and that the density of the lower 7-8 cm of the sample has increased significantly. It is also observed that the density of most of the binder phase in the intruded area has been altered, and that the majority of the anthracite grains in this area seem to have been reduced in size.

Figure 4.26 shows cross sections from 1 cm into the sample (from the bottom) before and after experiments in IF-75, and it is observed that silicon and/or slag has intruded into the sample in the lower 1 cm, but only into existing cracks.

Both the binder phase and the anthracite grains are mostly unaffected by the intruded furnace content in this region, but it is observed that the cracks have expanded somewhat during solidification. This expansion is highlighted in the close up images shown in figure 4.27, where it is measured that the circled crack has expanded from 0.1 to 0.4 mm.

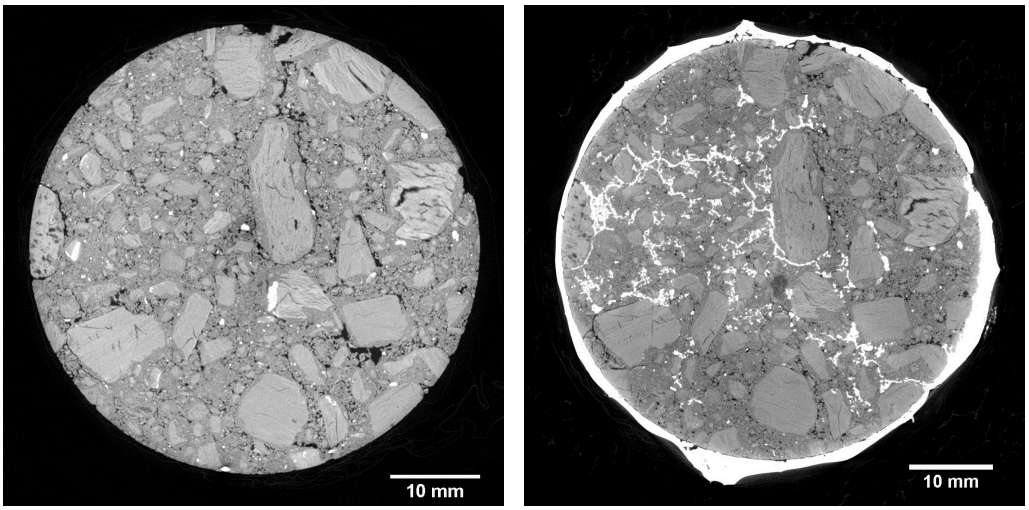

(a) Before furnace experiments **(b)** After furnace experiments

Figure 4.26: Cracks in sample V4, before and after exposure to silicon and slag.

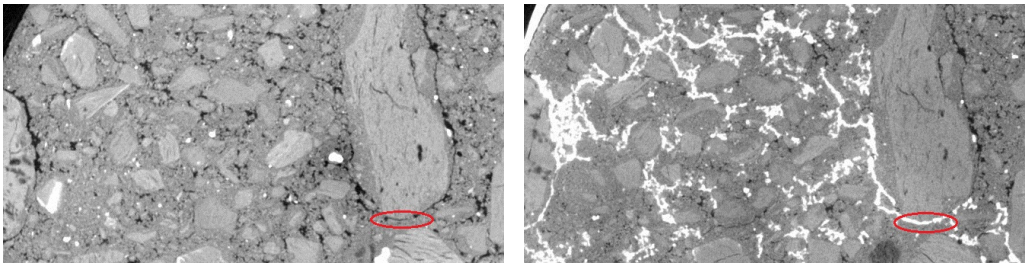

(a) Before exposure to silicon+slag **(b)** After exposure to silicon+slag

Figure 4.27: Close up images of cracks in sample V4, before and after exposure to silicon and slag.

Figure 4.28 shows cross sections from 5 cm into the sample both before and after exposure to liquid silicon and slag. In figure 4.28b taken after silicon exposure, only small areas of unaffected binder phase remain. It is also observed that most of the anthracite grains in figure 4.28a have shrinked compared with their size in the CT scan performed prior to the silicon exposure.

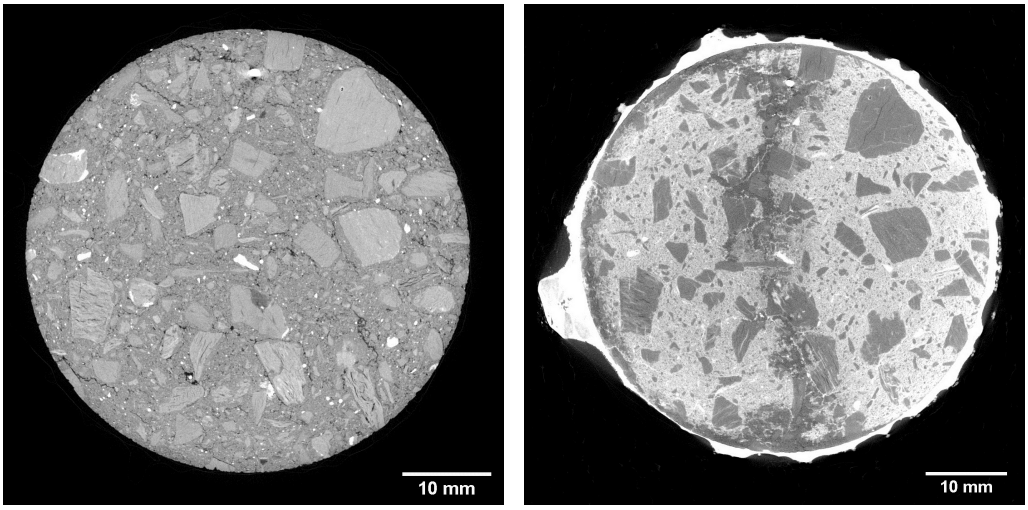

(a) Before **(b)** After

Figure 4.28: 5 cm into sample V4 before and after furnace experiments.

In sample V4, only a few examples of severely transformed anthracite grains can be found. Figure 4.29b and 4.30b show examples of transformed grains in sample V4. From the scans preformed before the experiment in IF-75, it is observed that these grains have darker areas and differ from the average anthracite grains. This can be observed in figure 4.29a and 4.30a.

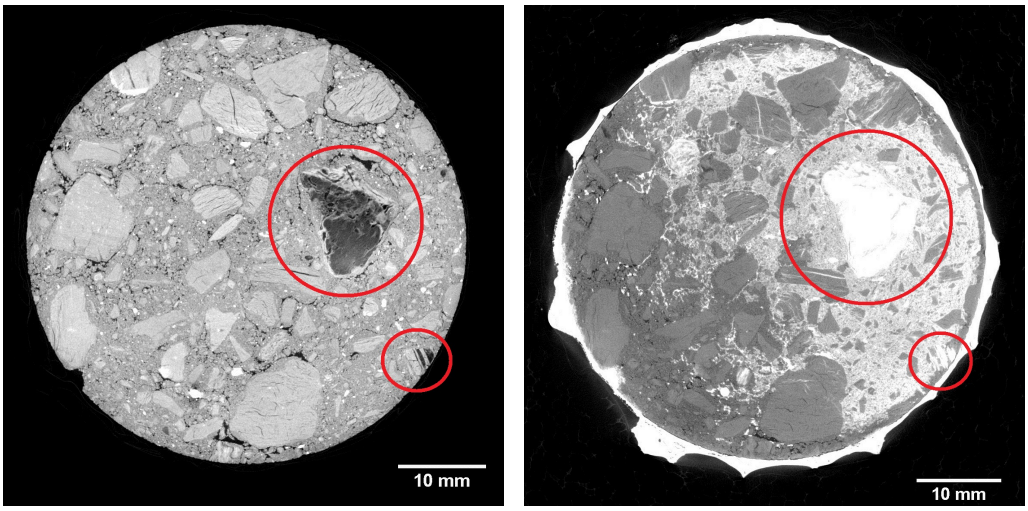

(a) Prior to silicon+slag exposure **(b)** After silicon+slag exposure

Figure 4.29: Examples of transformed anthracite grains after exposure to liquid silicon and slag.

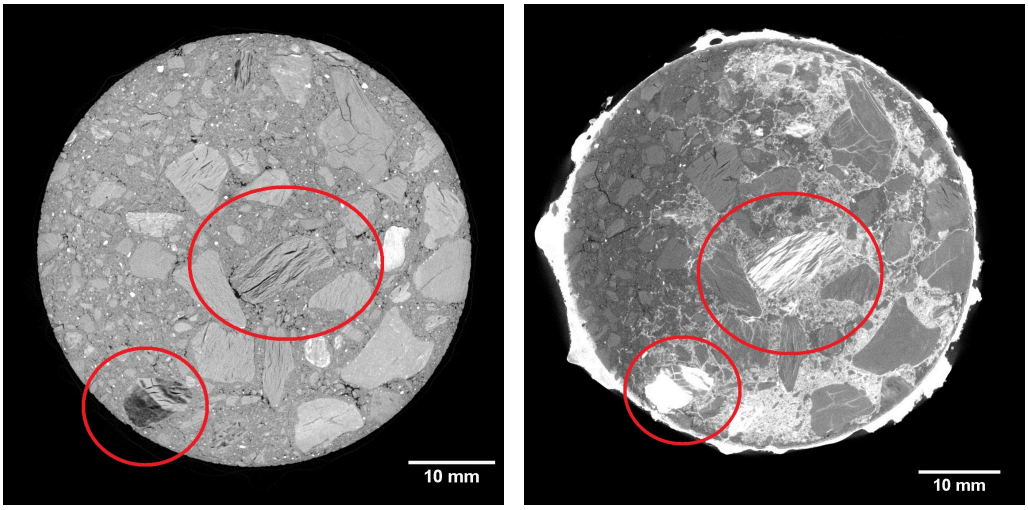

(a) Prior to silicon+slag exposure **(b)** After silicon+slag exposure

Figure 4.30: Examples of transformed anthracite grains after exposure to liquid silicon and slag.

From the CT scans, it appears as though the density of the sample interior after intrusion of furnace content differs from the density of the silicon surrounding the sample exterior. This could indicate reaction between the silicon and the carbon sample, primarily the binder phase (which was most severely altered, as shown in figure 4.28). Qualitative density measurements from the CT scans proved difficult, and to determine whether reaction has occurred, it is necessary to investigate the transformed areas using EPMA. This could help determine whether silicon or slag, or both, have intruded into the sample, and what the products of any reactions occuring between the intruded phases and the carbon lining might be.

Investigations using EPMA were performed on sections from both the interior and exterior of sample V4. The backscattered electron images from the sample exterior, shown in figure 4.31, show that the sample has been surrounded by both silicon and slag, but that in the interior of the sample, only silicon could be detected. An analysis of the slag in each of the two images in figure 4.31 was performed, the position of the analysis is marked by a red number 1 in figure 4.31a and 2 in figure 4.31b. The results are given in table 4.1, which also shows the original slag composition. Note that there were performed three analyses in each area (given in table B.2 and B.3 in appendix B), and that the values shown in table 4.1 are the average values from the three analyses. It is observed that the slags from the two different sections of sample V4 have slightly different compositions, and that neither completely match the original slag composition given in the Experimental chapter.

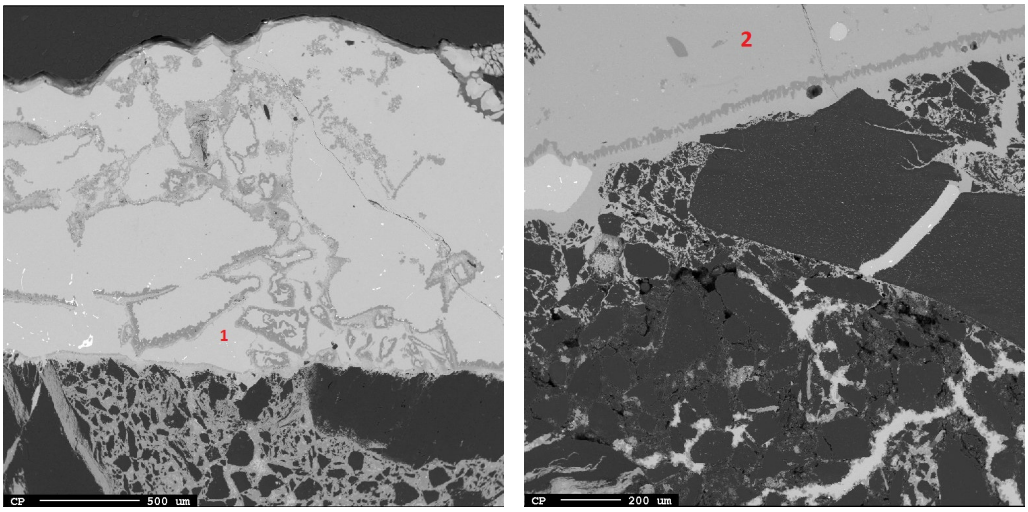

(a) **(b)**

Figure 4.31: EPMA images from the exterior and surrounding furnace content of sample V4.

Table 4.1: Analysis of slag surrounding sample V4 in figure 4.31a and 4.31b, as well as the original slag composition.

Element	Figure 4.31a [wt%]	Figure 4.31b [wt%]	Original slag comp. [wt%]
Al	8.103	9.554	7.935
O	25.61	36.586	47.41
Ca	11.061	15.763	14.3
C	8.255	4.474	0
Fe	0.002	0.005	0
Si	39.094	28.775	30.355

Mapping of the different elements in the area displayed in figure 4.31b was performed using the emitted X-ray photons, and the result is shown in figure 4.32. This shows that the intrusion into the sample interior is pure silicon, while the sample is mostly surrounded by slag. The maximum slag intrusion depth is measured to 500μm. The darker phase in the slag, just outside the sample surface, is silicon carbide, possibly broken free from the sample by the slag.

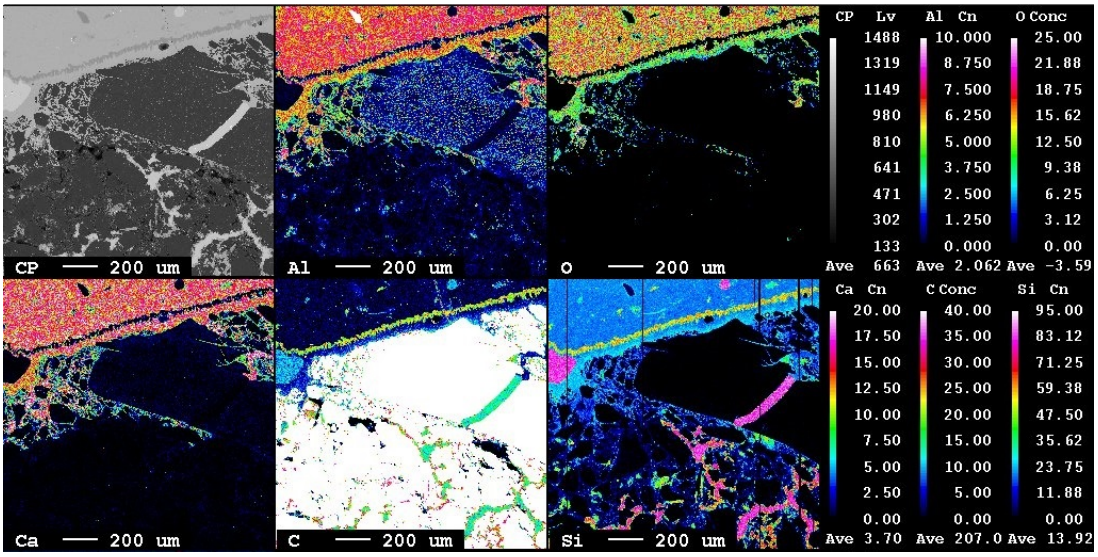

Figure 4.32: X-ray mapping of a section from the surface of sample V4.

Images from the sample interior, shown in figure 4.33, show that reaction has occurred between the binder phase and the intruded silicon, and analyses of the different elements show that the product of this conversion is silicon carbide. The formed SiC surrounds the anthracite grains, and no direct contact between silicon and anthracite grains can be observed. In the most heavily attacked regions, the entire binder phase has been converted, and the surface of the anthracite grains seems converted as well.

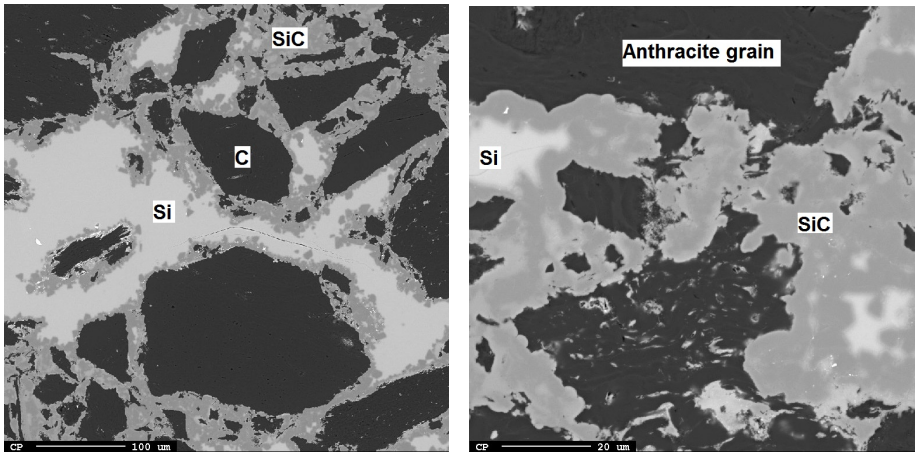

(a) **(b)**

Figure 4.33: EPMA images from the interior of sample V4.

4.2.3 Sample V5

Sample V5 was made with the same layered structure and from the same paste as sample V4. This sample was exposed to silicon and slag using the induction furnace, and the temperature was cycled twice between 1600°C and 1450°C. The conditions for this sample were similar to those for sample V4, with the exeption that the temperature cycling of sample V5 never dropped below the solidification temperature of silicon at 1416°C.

Figure 4.34 shows images of sample V5 taken from different views after the furnace experiment. Inspection of these images shows that the lower 3/4 of the sample has been exposed to the furnace content, and it looks like the lower half has been exposed only to liquid silicon. In the middle of the sample, and area with white deposit on the sample is oberved. This is assumed to be condensed SiO(g).

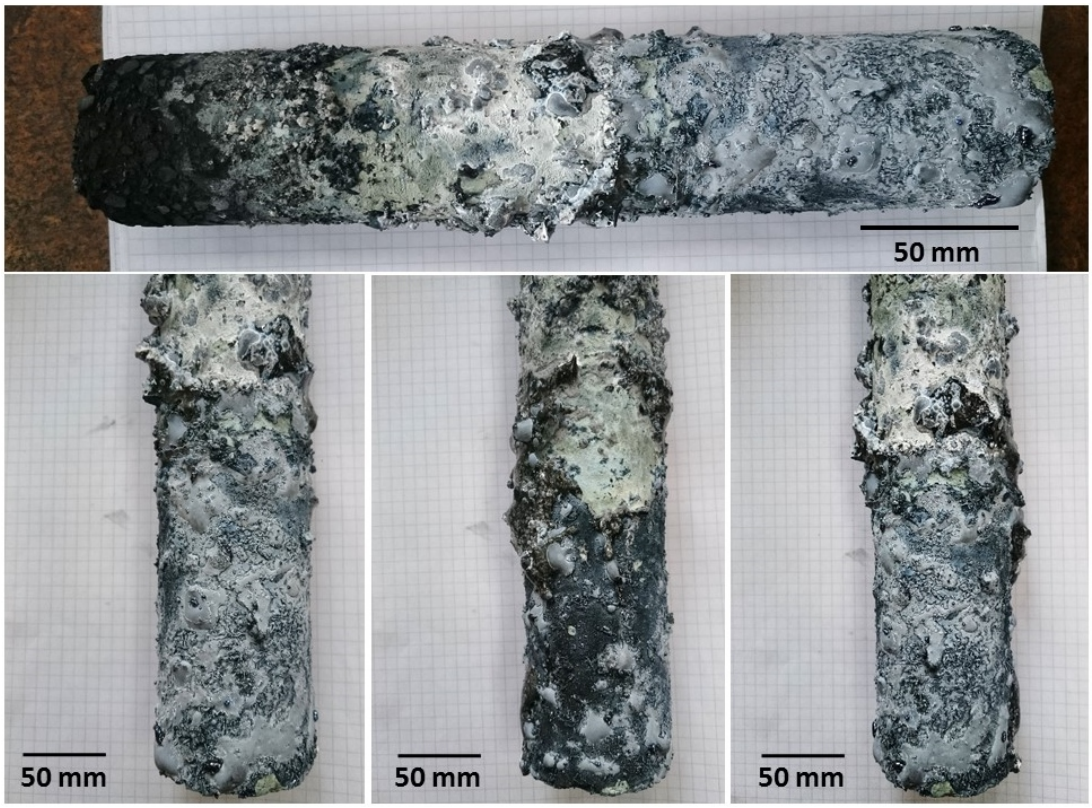

Figure 4.34: Visual inspection of sample V5 from different views, after experiments in the induction furnace.

By inspecting the orthogonal views of sample V5, obtained using CT, it is observed that the wetting seems good between the carbon lining surface and the silicon and slag. Despite this, no intrusion can be seen in the sample from these images. Figure 4.35 shows the orthogonal view of sample V5 in X-Z and Y-Z direction, after exposure to silicon and slag.

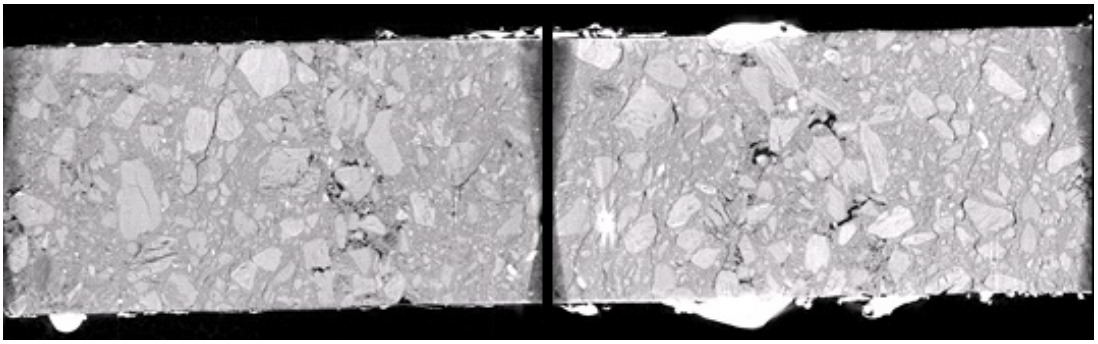

(a) X-Z direction

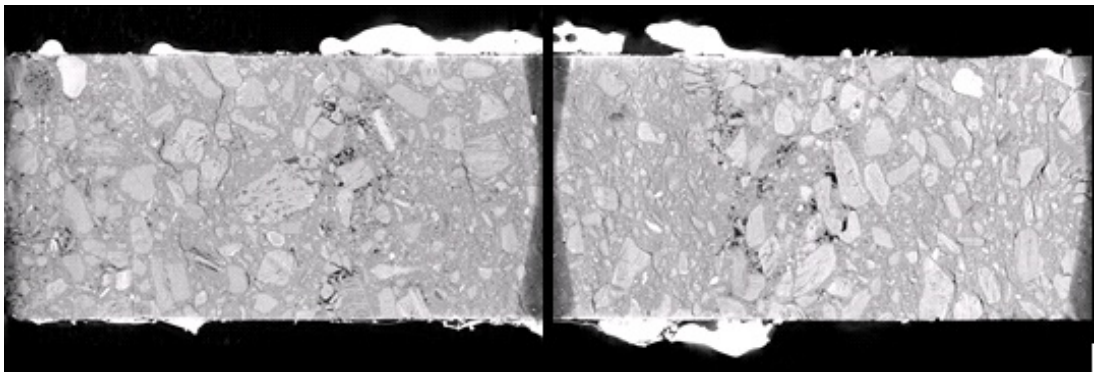

(b) Y-Z direction

Figure 4.35: Orthogonal views of sample V5 after exposure to silicon and slag.

When inspecting sample V5 using the X-Y cross sections, it is noticed that there seems to be a gap between the carbon lining sample and the silicon+slag. Figure 4.36 shows an area of sample V5 approximately 6 cm from the bottom of the sample, where there is a gap of approximately 0.25 mm between the sample surface and the surrounding silicon. An anthracite grain containing cracks with openings towards the silicon observed in this area looks completely unaffected by the surrounding furnace content. Figure 4.37a shows a cross section from the bottom of a ramming layer, where no intrusion or wetting of the surface pores has occurred, despite the increased porosity of the area. Figure 4.37b shows the bottom right section of figure 4.37a in higher magnification.

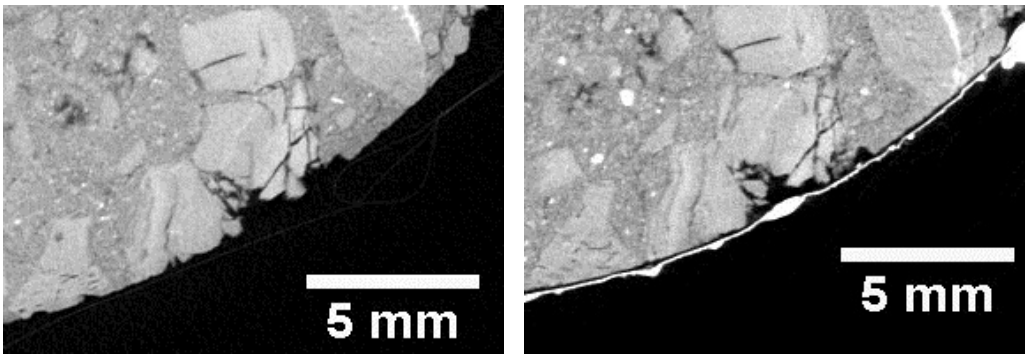

(a) Before exposure **(b)** After exposure

Figure 4.36: Section from 6 cm into sample V5 (layer bottom), where no intrusion has occurred.

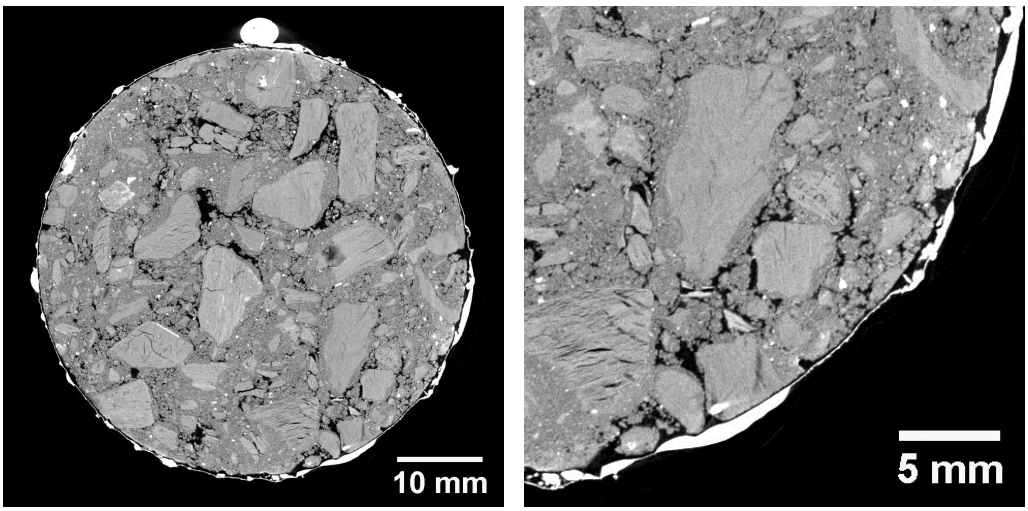

(a) Entire cross section **(b)** Magnified

Figure 4.37: Section from 5 cm into sample V5, where no intrusion has occurred.

Allthough no intrusion in sample V5 can be detected from the CT scans, and the wetting directly on the sample surface looks poor, it is observed that the density of the outer 0.5-1 mm of the sample has changed in several areas of the sample. This has occurred under the section of the sample which has been completely covered by furnace content, as can be seen in figure 4.38. The scans showed in this figure is collected from approximately 9 cm from the bottom of the sample, figure 4.38a is from before the furnace experiment, while figure 4.38b shows the same cross section after exposure to silicon and slag.

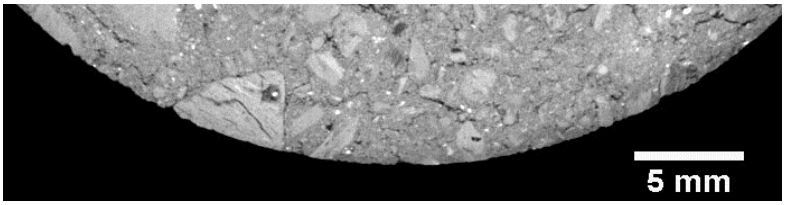

(a) Before exposure

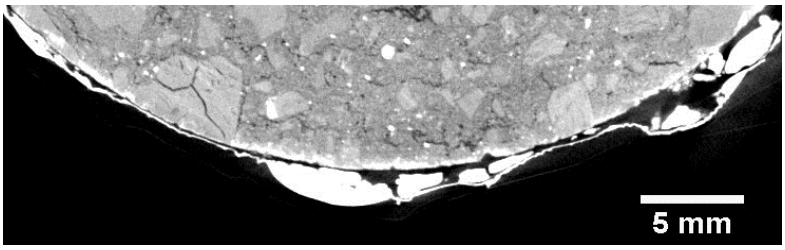

(b) After exposure

Figure 4.38: Section 9 cm from the bottom of sample V5, where a change in density of the outer 1 mm of the sample can be observed.

This change in density has also occurred in the upper sections of the sample, which have been subjected to SiO(g). Figure 4.39 shows a cross section scan from this area.

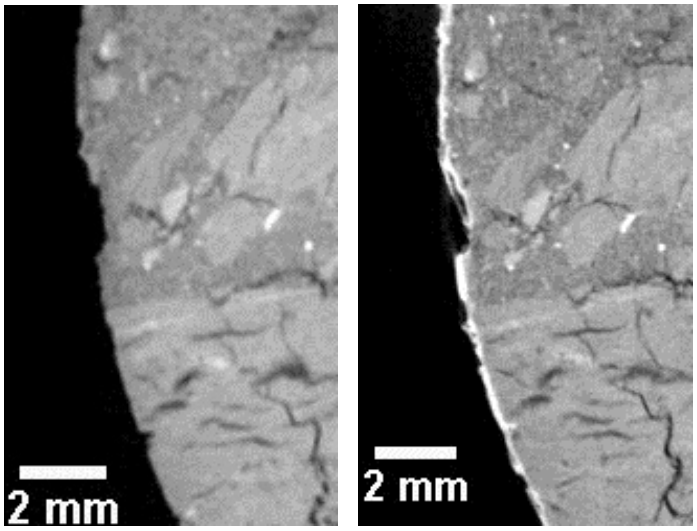

(a) Before exposure **(b)** After exposure

Figure 4.39: Section from the top of sample V5, where a change in density of the outer 1 mm of the sample can be observed.

Sections from both the surface and the interior of sample V5 was investigated using the backscattered electron imaging in EPMA, and allthough no intrusion of silicon or slag can be observed from the CT, the EPMA shows that areas with transformed lining can be found in the interior of the sample. Figure 4.40 shows images from the outer 0.5 mm of sample V5 from two different areas of the sample.

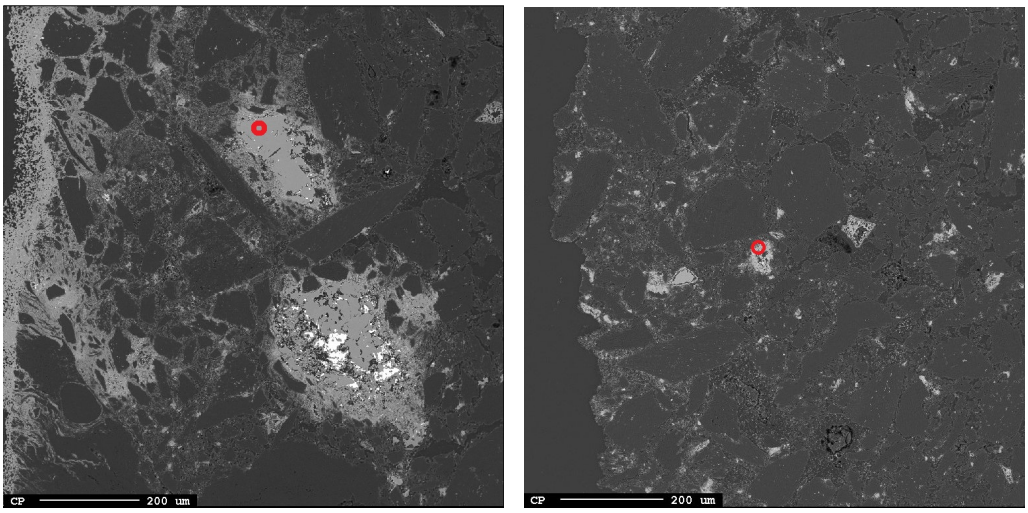

(a) **(b)**

Figure 4.40: Backscattered electron imaging of sample V5 using the EPMA.

Analyses performed in the circled areas of figure 4.40, given in table B.4 (figure 4.40a) and B.5 (figure 4.40b) appendix B, show that the transformed areas are silicon carbide. It is noted that no traces of pure silicon can be found in the proximity of the areas which have been transformed to SiC. Analysis of the lightest phase in figure 4.40a shows that this is iron, not silicon.

In figure 4.40a, it is observed that a porous layer surrounds the sample, and that some transformation of the binder phase can be observed up to 200 μm into sample V5. An image of this area in higher magnification is shown in figure 4.41, and a mapping of this area using the emitted X-ray photons was performed as well. This is given in figure 4.42, and shows that the outermost part of the porous layer on the surface consists of slag, while the sample surface is covered in SiO_2. Some slag can also be found in the outermost 50 μm of the sample, while only SiC and carbon lining can be detected from 50μm into the sample and inwards.

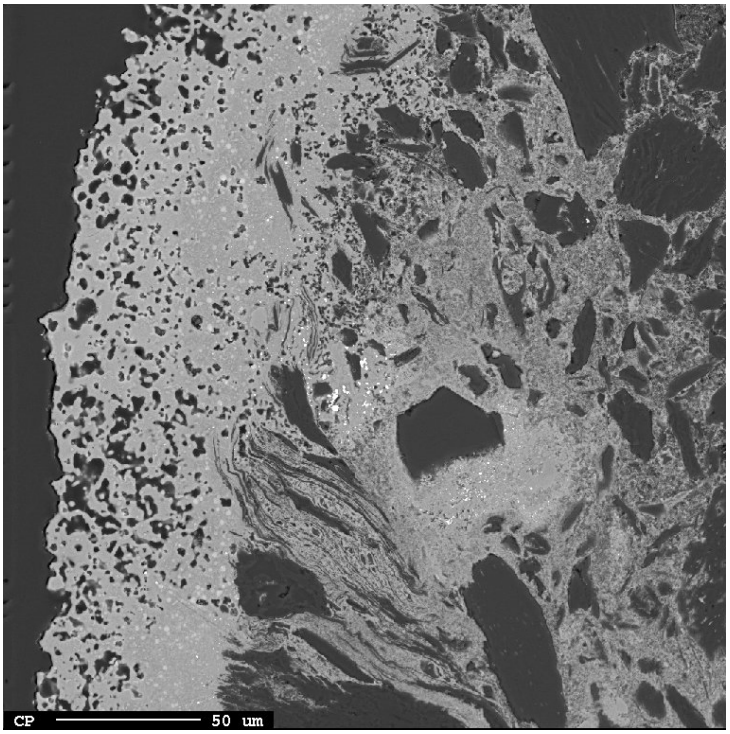

Figure 4.41: Close up EPMA image of sample V5 sample surface.

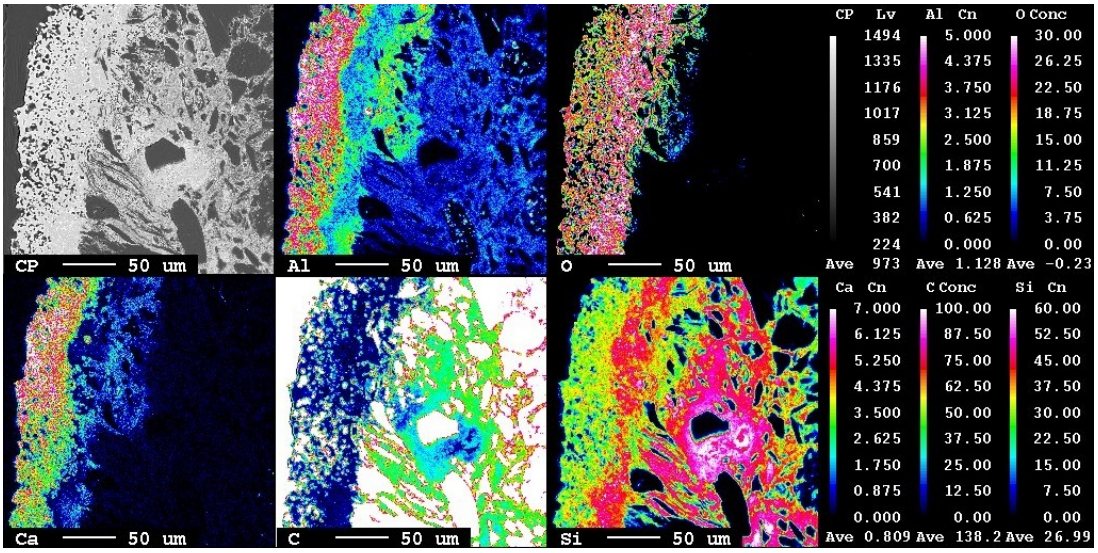

Figure 4.42: X-ray photon mapping of the area in figure 4.41.

4.2.4 Sample V6

Sample V6, with eco binder, fine silicon fractions and layers of approximately 1.5-2.0 cm, was subjected to silicon and slag using the induction furnace. The temperature was cycled twice between 1600°C and 1450°C. These are the same conditions as for the experiment with sample V5.

Visual inspection of sample V6, as in figure 4.43, shows that as the slag has melted, it has poured down one side of the sample. The rest of the sample seems to have been covered by silicon. Both the slag and the silicon seem to have wetted the sample completely.

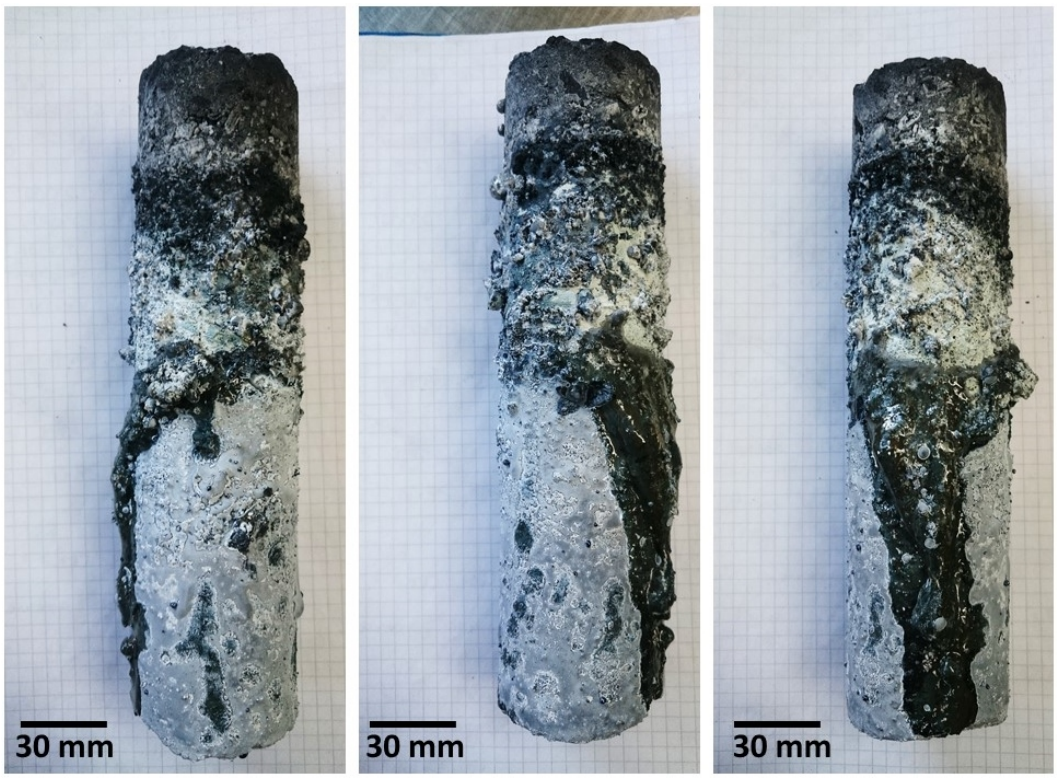

Figure 4.43: Visual inspection in different views of sample V6 after experiment in the induction furnace.

By inspecting sample V6 using CT, it is confirmed that the sample surface has been completely wetted by the silicon and slag. Figure 4.44 shows the orthogonal views of sample V6 in X-Z and Y-Z direction, after exposure to silicon and slag. From these images, some intrusion is observed approximately 1.5 cm from the bottom of the sample.

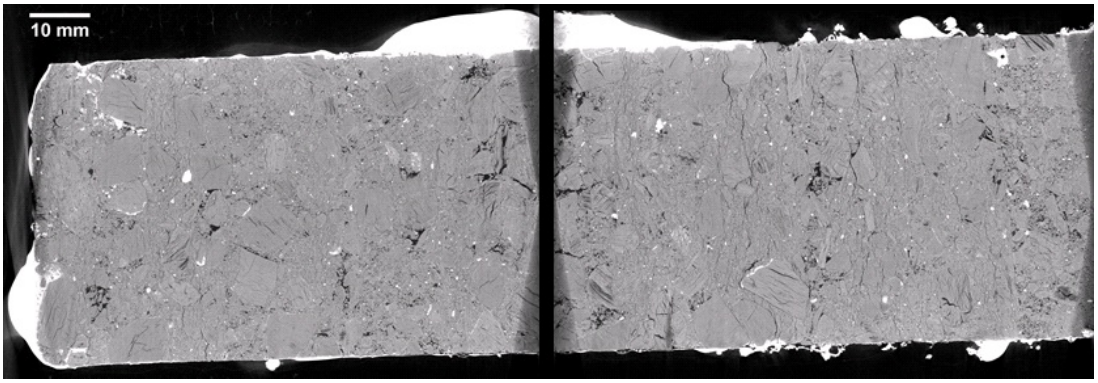

(a) X-Z direction

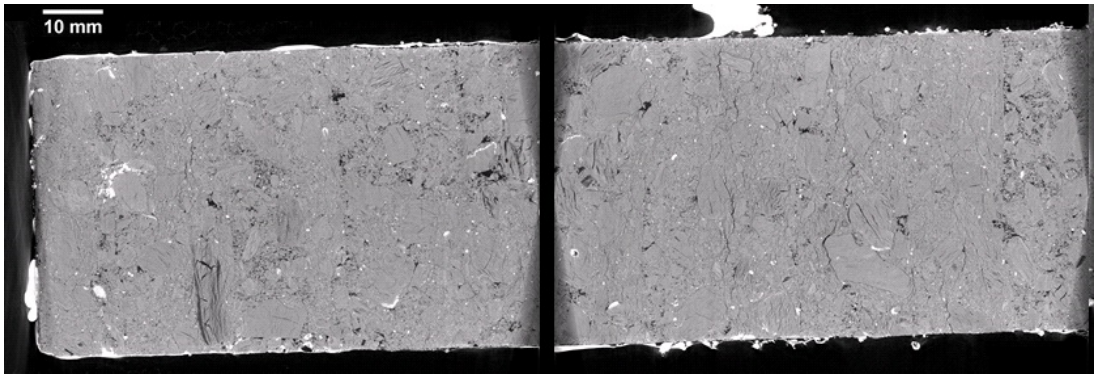

(b) Y-Z direction

Figure 4.44: Orthogonal views of sample V6 after exposure to silicon and slag.

This intrusion can also be investigated using the X-Y cross sections from the CT scans. It is observed that the intrusion had occurred in the bottom part of the second-bottom layer of the sample, where it previously has been observed that the lining is more porous. Figure 4.45 shows the area of intrusion both before and after exposure to silicon and slag.

Allthough only one area with intrusion could be found, approximately 1.5 cm into the sample as shown in figure 4.45, it is observed that the furnace content has eaten away parts of the carbon lining sample surface in other areas as well. This can be seen in figure 4.46, which shows an area 6 cm from the bottom of the sample, were parts of the sample surface seems to have been either transformed or replaced by the furnace content.

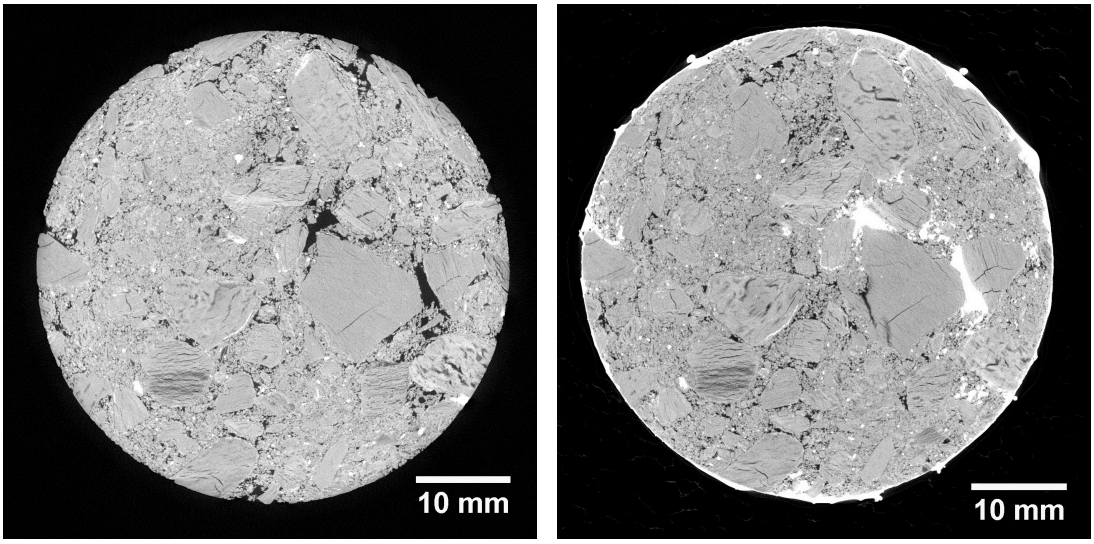

(a) Before furnace experiment **(b)** After furnace experiment

Figure 4.45: Intrusion of furnace content into sample V6, and the intruded area before exposure to silicon.

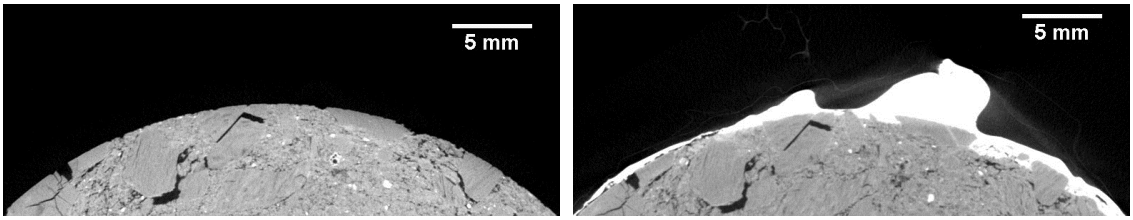

(a) Before furnace experiment **(b)** After furnace experiment

Figure 4.46: 6 cm from the bottom of sample V6, where silicon has transformed and/or replaced the lining sample surface.

When investigating sample V6 using the EPMA, it was attempted to get sections from the intruded area. Figure 4.47 shows the surface and outer 0.5 mm of sample V6 approximately 1.5 cm from the bottom. Mapping of this area using the emmited X-ray photons was performed, and this shows that the surface is surrounded by slag. The mapping can be seen in figure 4.48. It is noted that slag has intruded 600 μm into the sample, which is approximately the same slag intrusion depth as was observed in sample V4. The slag intrusion border is marked with a red line in figure 4.47. Inside this red line, SiC could be found. From the mapping, it can also be oberved that the slag on the surface contains areas with SiC, the most prominent beeing the string of SiC just outside the sample surface, highlighted

wth a blue line in figure 4.47.

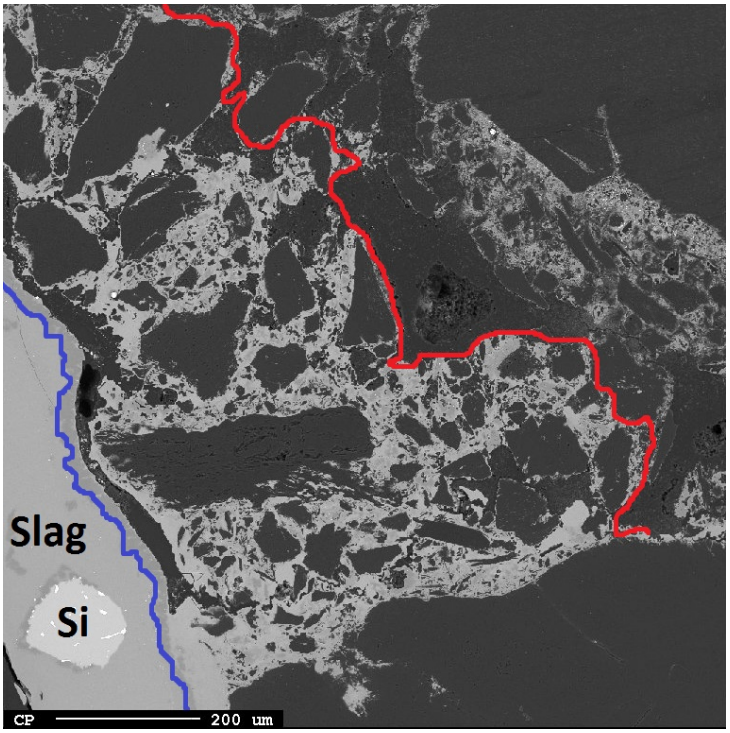

Figure 4.47: EPMA backscattered electron imaging of the surface of sample V6.

EPMA investigations were also performed in the sample interior, such as in figure 4.49a, which shows the middle of the same cross section as figure 4.47 is collected from. In figure 4.49a, it is noted that larger areas of SiC have formed in the sample interior (analysis of the formed SiC is given in table B.6 in appendix B), and it is noted that no unreacted silicon can be found in the sample interior. The brightest phase in both of the images was analyzed, and it was determined that this is iron, not silicon. It is also noted that the SiC formed in the area circled in red is surrounding an area with expoxy, which indicates that it has formed in a pore in the carbon lining. It is also noted that the large areas of formed SiC look quite solid, compared with the silicon carbide found in figure 4.47. In addition to these larger areas of solid SiC, small specks of SiC could be found all through the section. This SiC resembles that found in figure 4.47.

The area circled in blue in figure 4.49a is shown in higher magnification in figure 4.49b, and it is noted that the anthracite grains are covered by a very thin layer of SiC. The density of this layer was measured and it was determined that

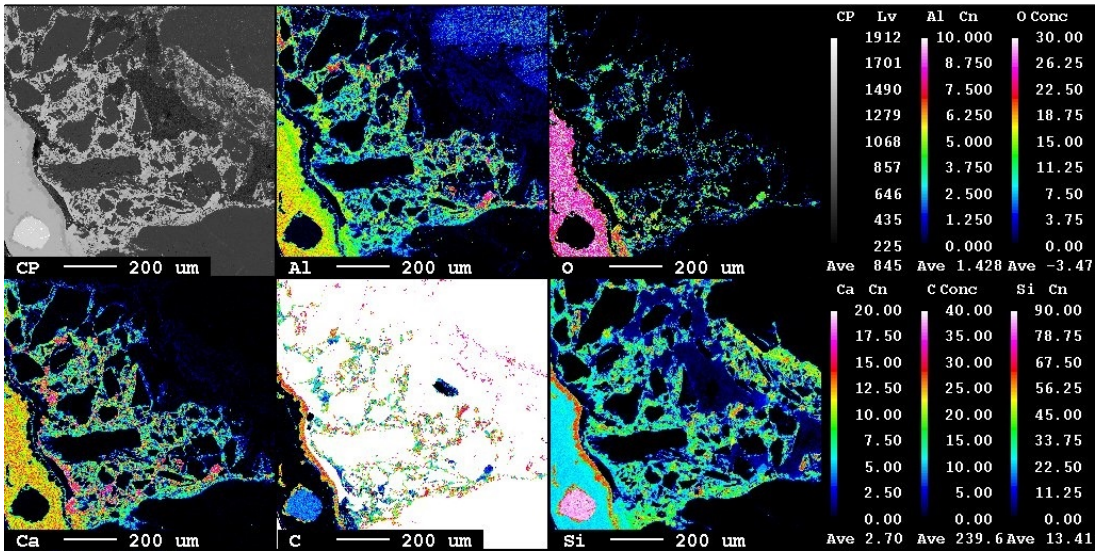

Figure 4.48: X-ray photon mapping of the area in figure 4.47.

the thickness of the SiC layer surrounding the anthracite grains is approximately 0.25 μm.

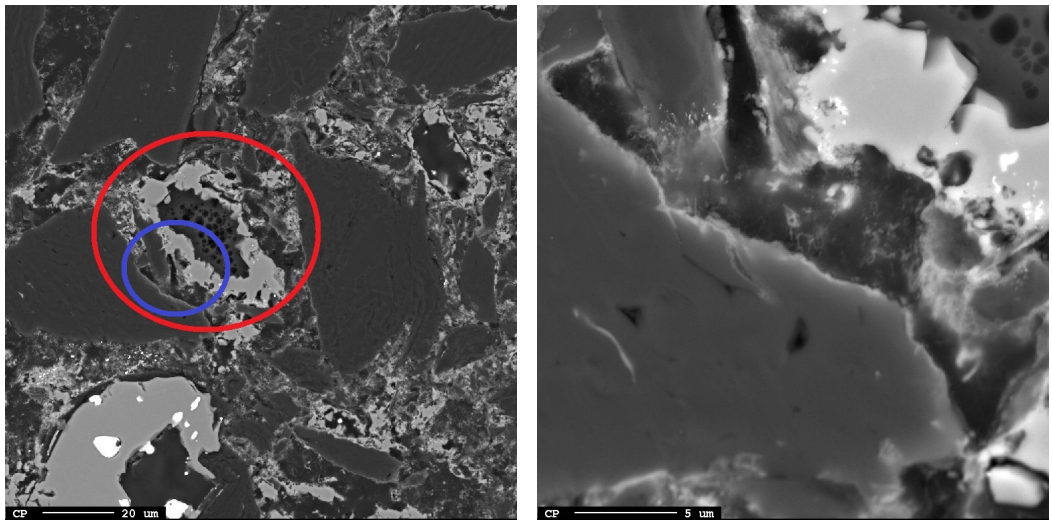

(a) **(b)**

Figure 4.49: EPMA backscattered electron imaging of the interior of sample V6.

4.2.5 Sample V7

Sample V7, with eco binder and fine silicon fractions, was exposed to silicon using the induction furnace, and the temperature was cycled twice between 1600°C and 1450°C. The conditions for this sample were similar to those for sample V6, with the presence of slag being the exeption.

Visual inspection of sample V7, shown in figure 4.50, shows that the bottom half of the sample has been covered by liquid silicon. It is also noted that there seems to have formed an oxide crust between the melted silicon covering the lower half of the sample, and the top of the sample which has been exposed to air. Above this crust, part of the sample is covered by what is assumed to be deposits of condensed SiO(g), while the rest of the sample has been exposed to oxygen. Below this crust, wetting between silicon and the sample surface looks complete.

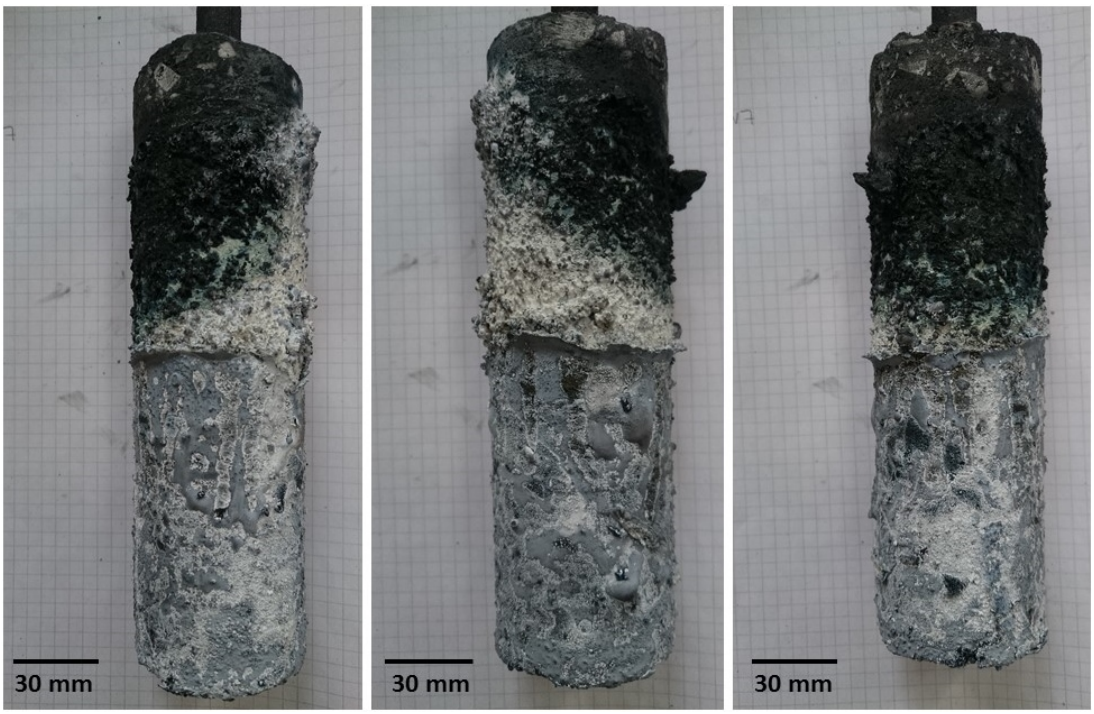

Figure 4.50: Visual inspection of sample V7 in different views, after furnace experiment.

By inspecting sample V7 using CT, it is observed that intrusion has occurred approximately 1.5 cm from the bottom of the sample. Figure 4.51 shows the orthogonal views of sample V7 in X-Z and Y-Z direction, after exposure to silicon.

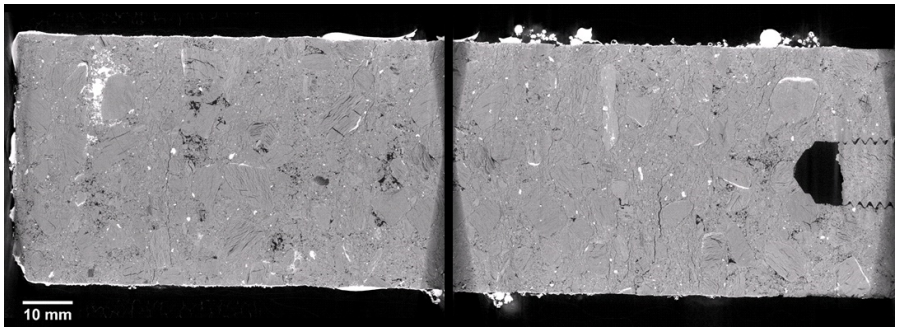

(a) X-Z direction

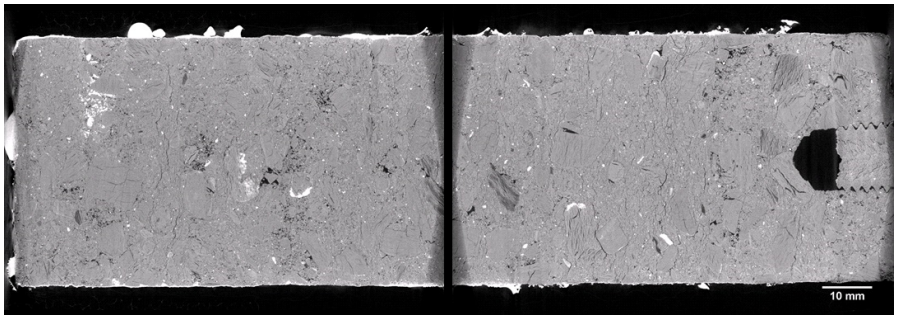

(b) Y-Z direction

Figure 4.51: Orthogonal views of sample V7 after exposure to silicon and slag.

This intrusion can also be seen in the X-Y cross section images, as shown in figure 4.52. It is observed that the intrusion has occurred in the porous bottom part of a layer, and it is noted that this was the case in sample V6 as well.

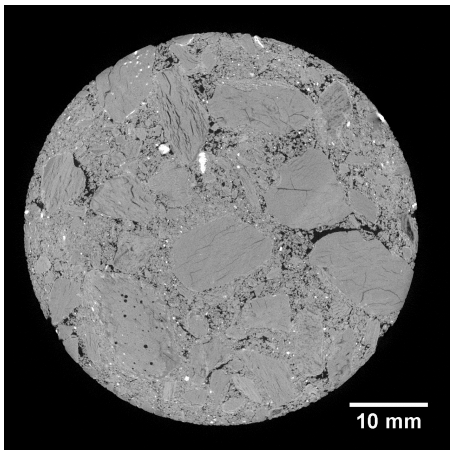

(a) Before exposure to silicon

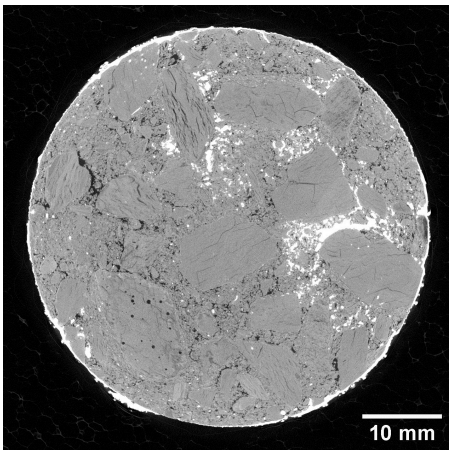

(b) After exposure to silicon

Figure 4.52: Intrusion of silicon into sample V7, and the intruded area before exposure.

Allthough the area shown in figure 4.52 was the only observed area with intrusion into the center of the sample, intrusion was observed in cracks on the sample surface in other areas of the sample as well. This intrusion was observed both in cracks in the binder phase and cracks in anthracite grains on the sample surface. Figure 4.53 shows intrusion into cracks in an anthracite grain, while figure 4.54 shows intrusion into a crack in the binder phase. Both figures show CT scans taken both before and after exposure to liquid silicon.

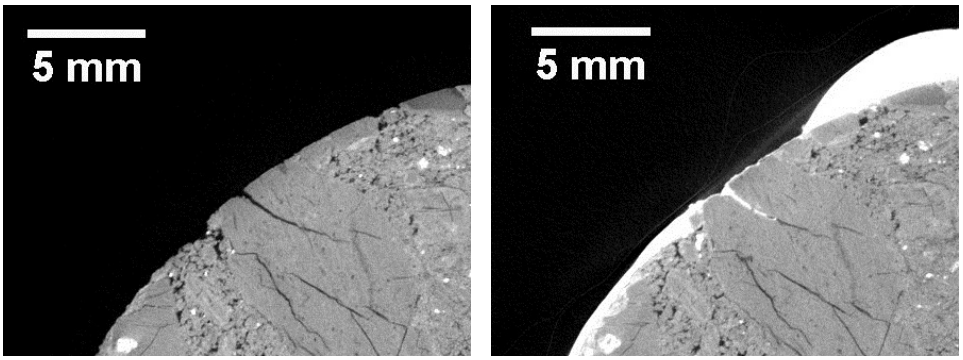

(a) Before exposure to silicon **(b)** After exposure to silicon

Figure 4.53: Intrusion of silicon into an anthracite grain in sample V7, and the intruded area before exposure.

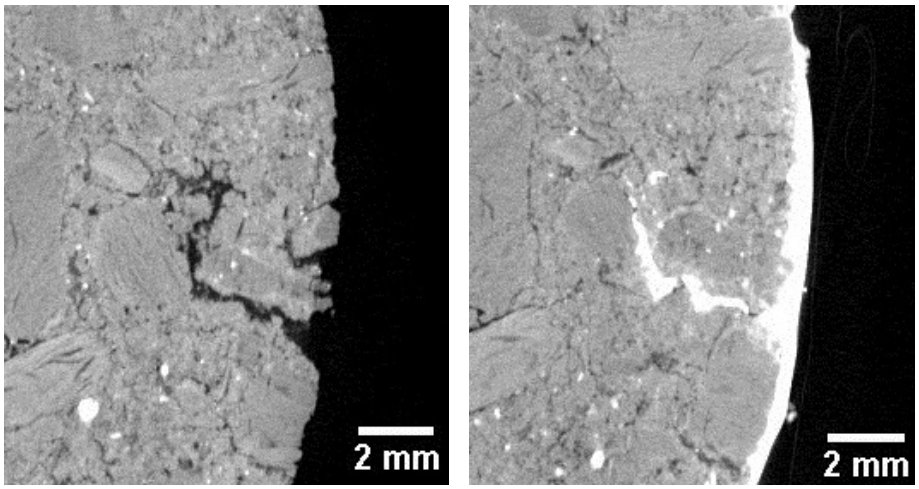

(a) Before exposure to silicon **(b)** After exposure to silicon

Figure 4.54: Intrusion of silicon into the binder phase in sample V7, and the intruded area before exposure.

When inspecting intrusion into cracks in sample V7 on the sample surface using EPMA, it is observed that significant amounts of silicon remain untransformed in the intruded area, which gives potential for expansion of the silicon and spalling of the lining during solidification. Figure 4.55a shows intrusion into a crack in the surface of sample V7, with intruded silicon and formed silicon carbide in the binder phase surrounding the crack. The area circled in red is shown in higher magnification in figure 4.55b.

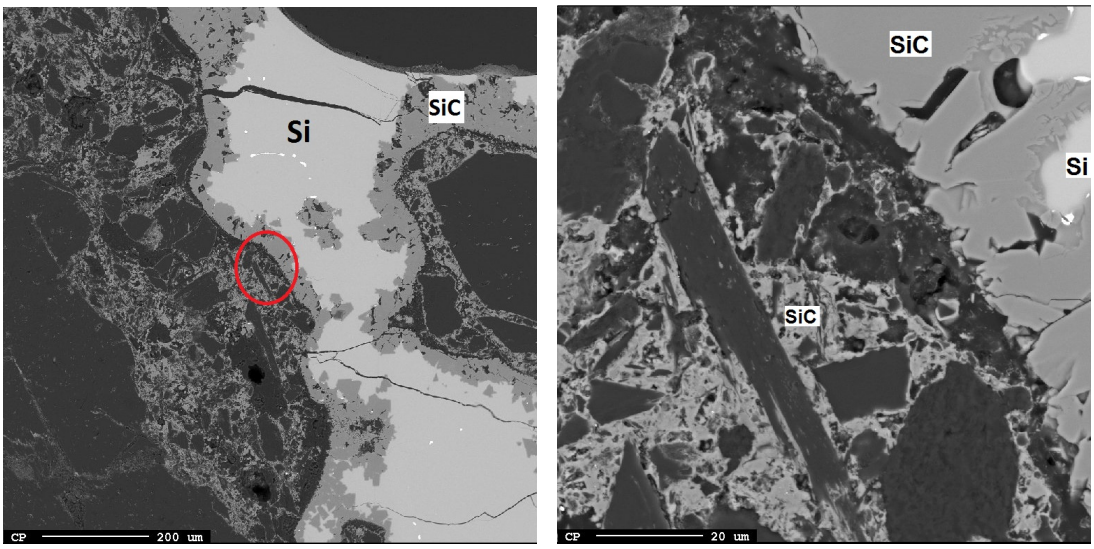

(a) **(b)**

Figure 4.55: Backscattered electron images showing intrusion of silicon into a surface crack in sample V7.

In figure 4.55, it is noted that very solid looking SiC has formed in the interface between the carbon lining sample and the intruded silicon. In addition to this, small specks of silicon carbide can be found inside the lining, similar to the specks of SiC formation in sample V6. This SiC is probably not formed by intruded silicon, but either from reactions with intruded SiO(g) or by reaction with the silicon fractions added in the paste.

The sample interior was also investigated using EPMA, and areas containing silicon and SiC was found. Figure 4.56 shows the middle of sample V7 approximately 1.6 cm from the bottom of the sample, where both silicon and SiC can be found. It is observed that SiC has formed between the intruded silicon and the carbon lining in the area circled in red, and this closely resembles the observations in sample V4. In the area circled in blue, only solid silicon carbide can be found, which is more similar to the areas of solid SiC found in sample V6 in figure 4.47.

Analyses of both areas are given in table B.7 and B.8 in appendix B. In addition to the SiC formed in large lumps, small specks of SiC similar to those in the binder phase of sample V6 is found in the sample interior as well.

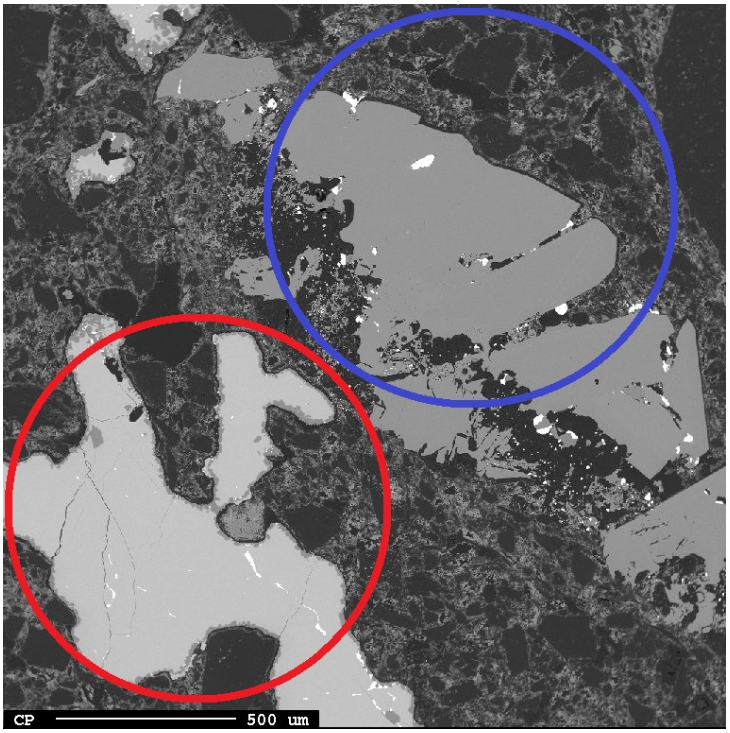

Figure 4.56: Backscattered electron imaging of the interior of sample V7, obtained using EPMA. The red circle highlights a pore containing silicon and formed silicon carbide in the silicon - lining interface, while the blue circle envelopes an area of solid SiC.

4.2.6 Sample V8

Sample V8, made with resin binder and one 8.2 cm thick layer, was subjected to silicon and slag using the induction furnace. In this experiment, the temperature was cycled around the solidification temperature for silicon, such as in the experiment with sample V4.

Visual inspection of sample V8 shows that one side of the sample has been completely covered in slag, while the other has been exposed to liquid silicon. This can be seen in figure 4.57, which shows all sides of sample V8.

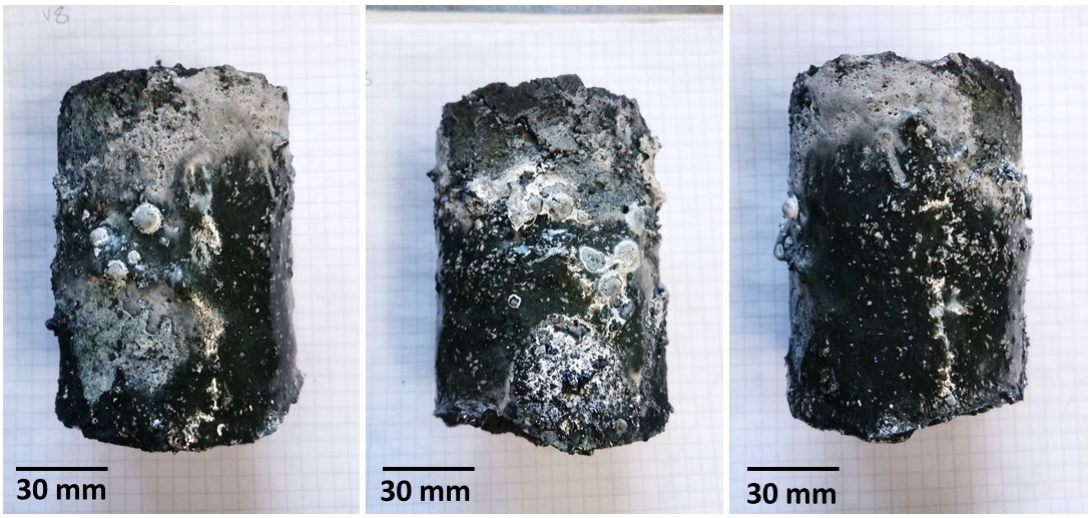

Figure 4.57: Visual inspection of sample V8 from different views.

By inspecting sample V8 using CT, it is observed that the entire lower 3/4 of the sample has been covered by silicon and slag, and that the furnace content has intruded into the lower parts of the sample. The intrusion has occurred only in one side of the sample and over almost half of the sample height. Figure 4.58 shows the orthogonal views of sample V8 in X-Z and Y-Z direction, after exposure to silicon and slag.

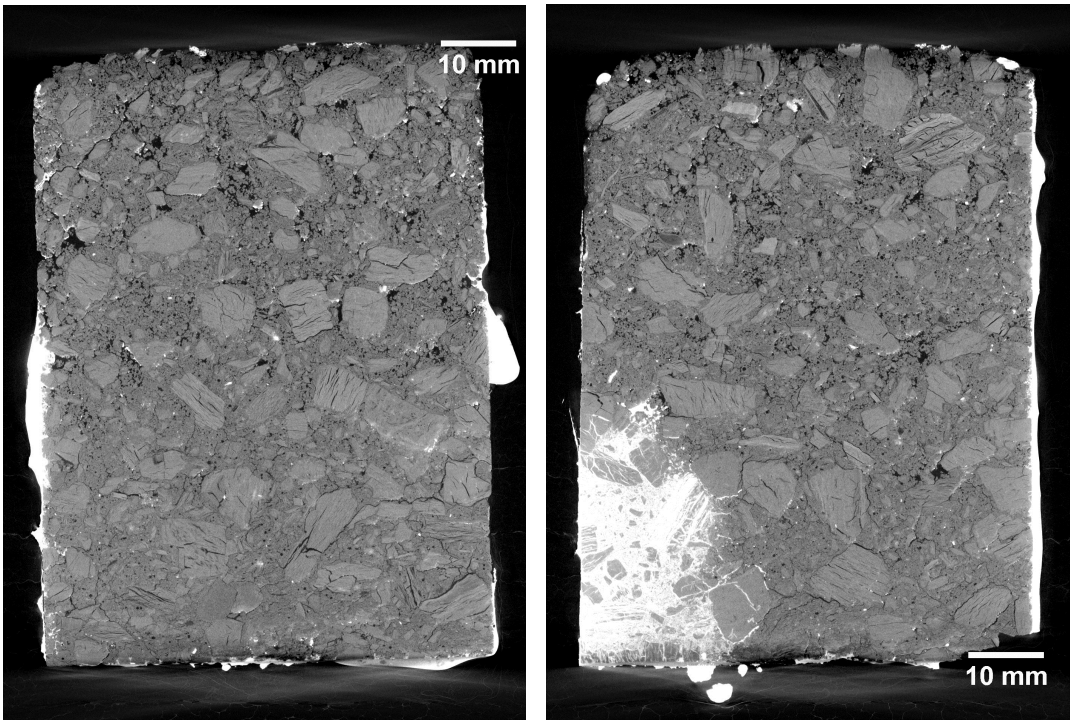

(a) X-Z direction **(b)** Y-Z direction

Figure 4.58: Orthogonal views of sample V8 after exposure to silicon and slag.

When inspecting the intruded area in the X-Y cross sections, it is observed that most of the binder phase in the intruded area has been altered by the intruded furnace content. This can be seen in the cross section scan from 2.7 cm from the bottom of the sample, shown in figure 4.59b. When inspecting the intruded area in the CT scans performed before the furnace experiment as in figure 4.59a, no difference between the intruded part of the sample and the unaffected part of the sample can be observed.

By comparing the orthogonal views from the CT with the visual inspection, it is observed that the intrusion has occurred in the part of the sample which has been exposed to silicon or silicon and slag, and that no visible intrusion has occurred in the section covered only by slag.

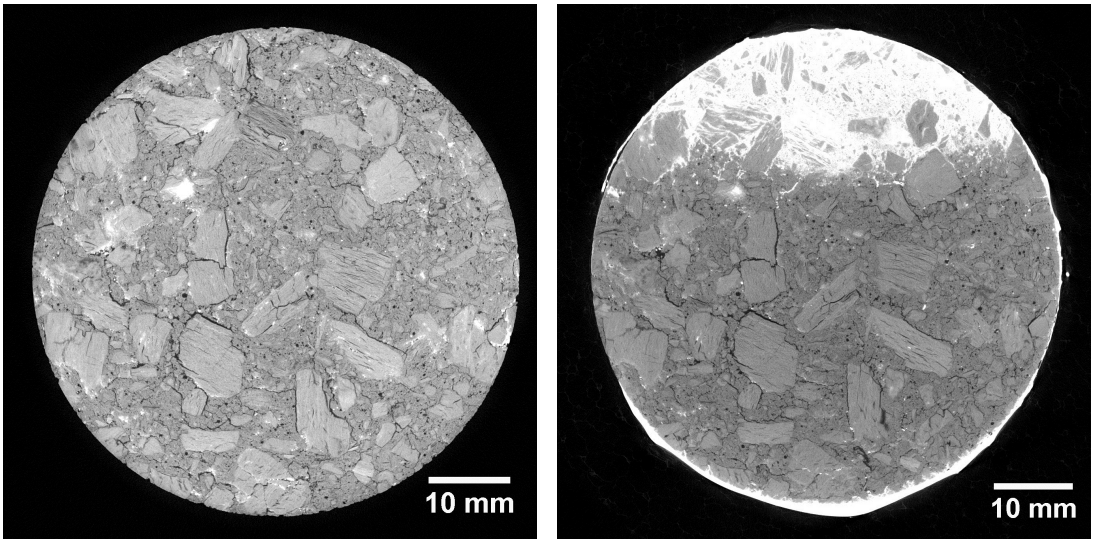

(a) Before furnace experiment **(b)** After furnace experiment

Figure 4.59: Area of intrusion in sample V8, before and after furnace experiment.

As in sample V7, intrusion was observed both in cracked anthracite grains and in cracks in the binder phase. Figure 4.60 shows a cross section from 5.2 cm into the sample which shows examples of both; the right hand circle highlights an anthracite grain with furnace content intruded into cracks in the grain while the left hand circle highlights intrusion into the binder phase.

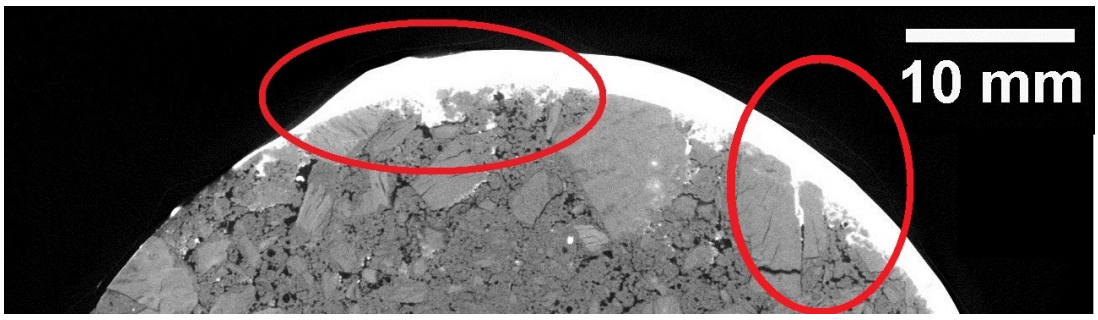

Figure 4.60: Intrusion in anthracite grain and binder phase, 5.2 cm into sample V8.

Investigations of the intruded side of sample V8 using backscattered electron imaging in EPMA show that only silicon is in direct contact with the sample surface and that only silicon seems to have intruded into the sample. Slag is also found in this area, but never close to the surface or intruded into the sample. Figure 4.61 shows the sample surface of sample V8, with SiC both formed in the sample,

and in the surrounding silicon. It is noted that the intruded areas further into the sample contain both silicon and SiC, and resembles the intrusion found in sample V4.

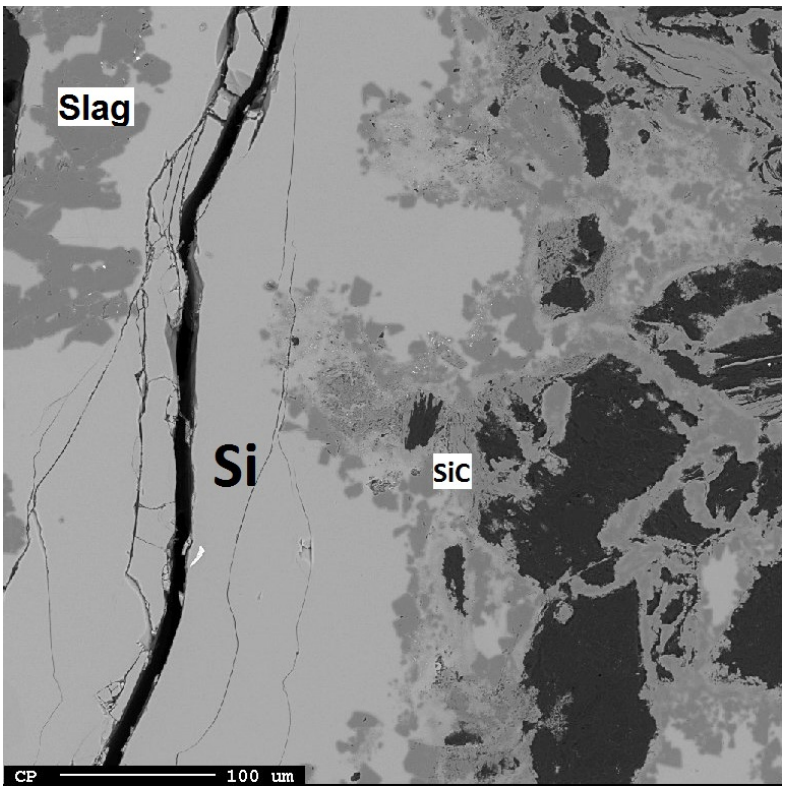

Figure 4.61: EPMA backscattered electron image of V8 sample surface.

Figure 4.62a shows an EPMA image of another area on the surface of sample V8, where a large anthracite grain has been intruded into. It is noticed that this grain has been significantly more affected by the silicon than the other grains, and it was speculated whether the structure of this grain resembles the grains found in sample V4 with altered structure (see figure 4.29b). However, comparison with the CT images of what is believed to be the same grain performed prior to silicon exposure, shows that the intruded grain looks similar to all other grains in sample V8, only with more cracks. The CT image is given in figure 4.62b, note that the two images have different orientations.

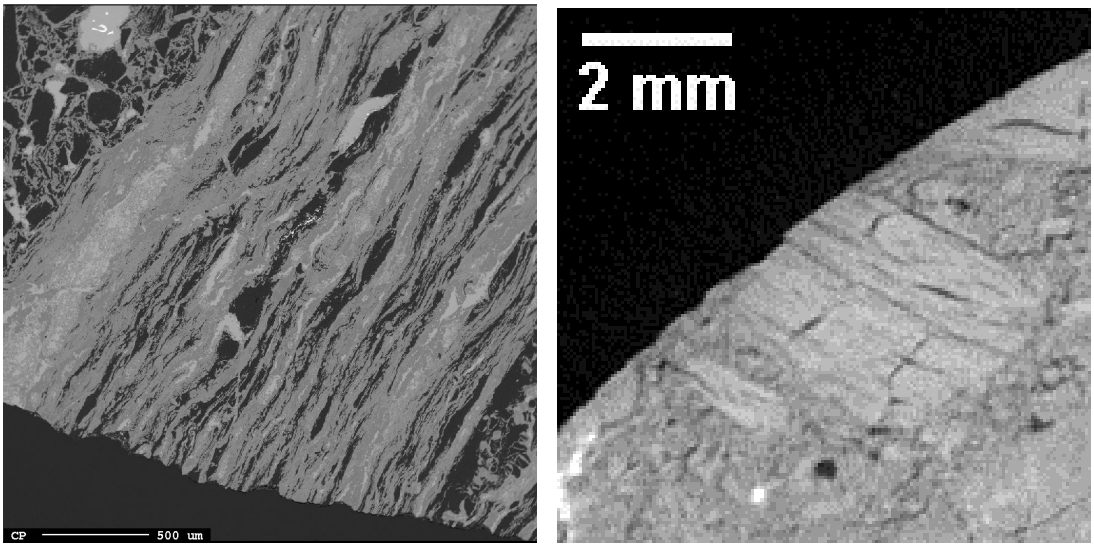

(a) EPMA image **(b)** CT

Figure 4.62: EPMA image of intrusion into an anthracite grain in sample V8, and CT images from the same area prior to silicon exposure.

Figure 4.63 shows the interior of the grain shown in figure 4.62a in higher magnification. It is noted that both silicon and SiC is found inside the grain, while the brightest phase was determined by X-ray photon analysis as iron.

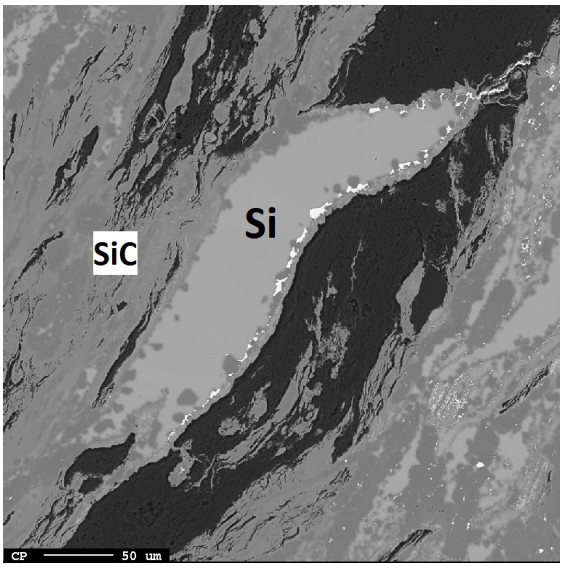

Figure 4.63: Interior of intruded grain in high magnification.

4.3 Entech resistance heated furnace

4.3.1 Sample FS4

Sample FS4, made with tar pitch binder and a solid structure, was heated with silicon from room temperature to 1475°C using the Entech electrical resistance heated furnace. The sample and silicon was held at this temperature for 45 minutes before the experiment was terminated and the sample cooled to room temperature.

Figure 4.64 shows images of sample FS4 taken in different views after the Entech furnace experiments. From these images, large lumps can be observed at the lining sample surface, and only small areas of the lining sample surface seem to have been in contact with liquid silicon. It is also noticed that the top of the sample is covered in a white layer of what is assumed to be condensed SiO(g).

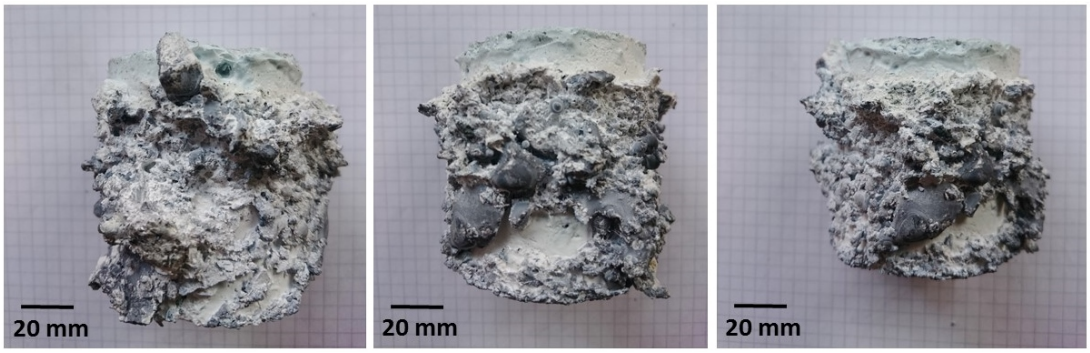

Figure 4.64: Visual inspection of sample FS4 in different views, after exposure to liquid silicon in the Entech furnace.

When investigating the same sample using CT, the assumption that almost no liquid silicon covers the sample surface is confirmed. The cross section images from the CT was processed using ImageJ to obtain the orthogonal views in X-Z and Y-Z direction, and the result from this can be seen in figure 4.65. From the orthogonal images it is noted that only large, unmelted lumps at the sample surface can be observed, similar to the observations in the visual inspection.

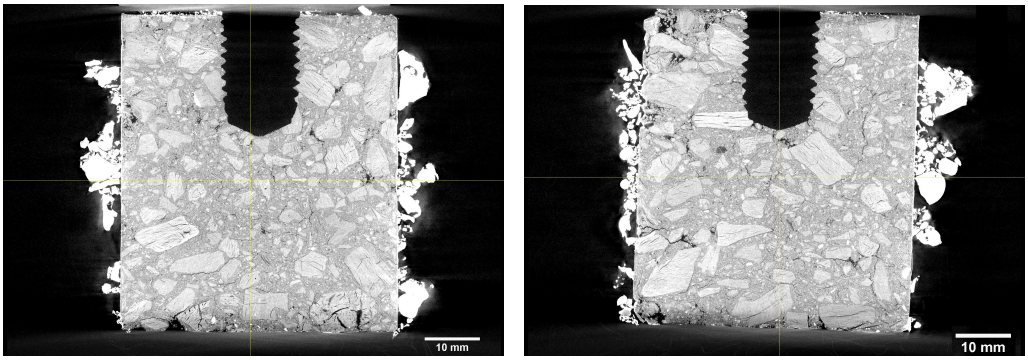

(a) X-Z direction **(b)** Y-Z direction

Figure 4.65: Orthogonal views in X-Z and Y-Z direction of sample FS4 after exposure to silicon in the resistance furnace.

This can also be seen in the images taken in the X-Y plane, as shown in figure 4.66. From these images it is observed that none of the silicon lumps are wetting the surface, and that no visible intrusion or chemical reaction occurs between the carbon lining sample and the silicon. It is also observed that the silicon surrounding the sample surface seems to be sharp and angular/edged in the images taken from the top 2 cm of the sample, see figure 4.66a taken 1.8 cm from the top of the sample. In comparison, the silicon in images taken in the bottom 2 cm of the sample, see figure 4.66b, seem to be smoother and less jagged, and the lumps seem more melted than those in figure 4.66a.

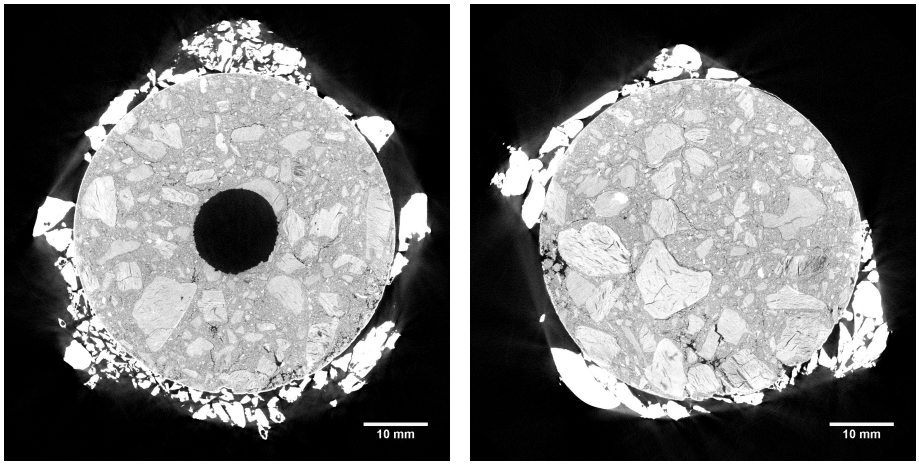

(a) From the top of the sample **(b)** From the bottom of the sample

Figure 4.66: Images of sample FS4 in X-Y direction, figure 4.66a from 1.76 cm from the top, figure 4.66b from 2.0 cm from the bottom of the sample.

Smaller sections of sample FS4 were cut from the sample and prepared for EPMA. Due to the lack of intrusion and reaction visible on the CT scans, all sections were selected from the surface of the sample. Investigation of the sample surface and surrounding silicon show that some reaction has occurred between the surrounding silicon or formed SiO gas and the sample surface. Figure 4.67a shows a backscattered electron image of the sample surface with silicon carbide on the surface of the sample, and figure 4.67b shows the circled area in higher magnification.

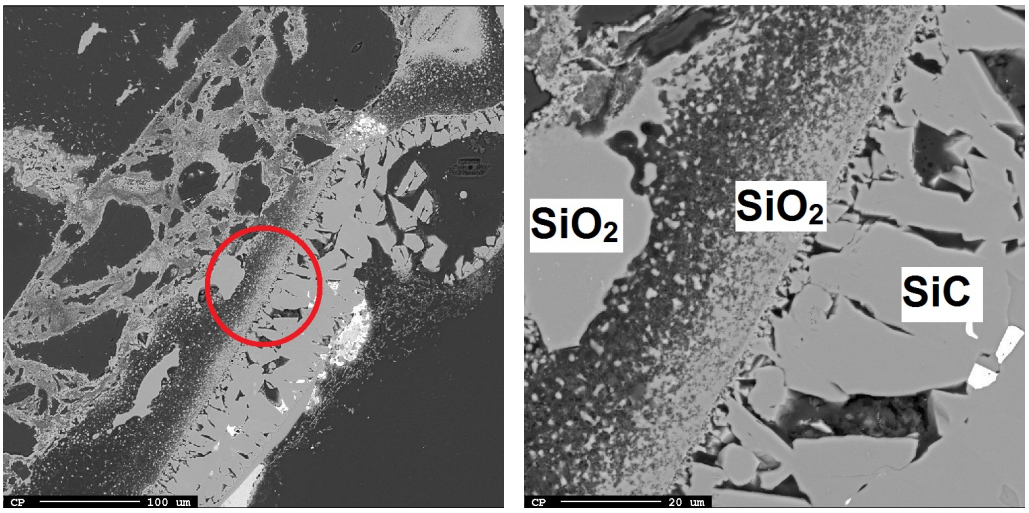

(a) **(b)**

Figure 4.67: EPMA images from the exterior and surrounding furnace content of sample FS4.

Mapping of the area in figure 4.67b using the emitted X-ray photons gives an analysis of the elements present, confirming that the substance in contact with the sample surface is silicon carbide. It also shows that the outer 10 μm of the sample surface has been transformed from pure carbon lining, and that this area of the sample now contain significant amounts of oxygen. The solid areas with altered density were also analyzed, and it was determined that these areas now contain SiO_2. The mapping is shown in figure 4.68.

Backscattered electron images taken from another area of the sample, still using the EPMA, show that the interior of the sample has been affected by the furnace experiment. Figure 4.69a shows an area 3 mm into the sample, where it is observed that the binder phase is transformed and that some of the anthracite grains are surrounded by a layer of conversion product. Figure 4.69b shows the circled area of figure 4.69a in higher magnification, and an analysis performed in the area

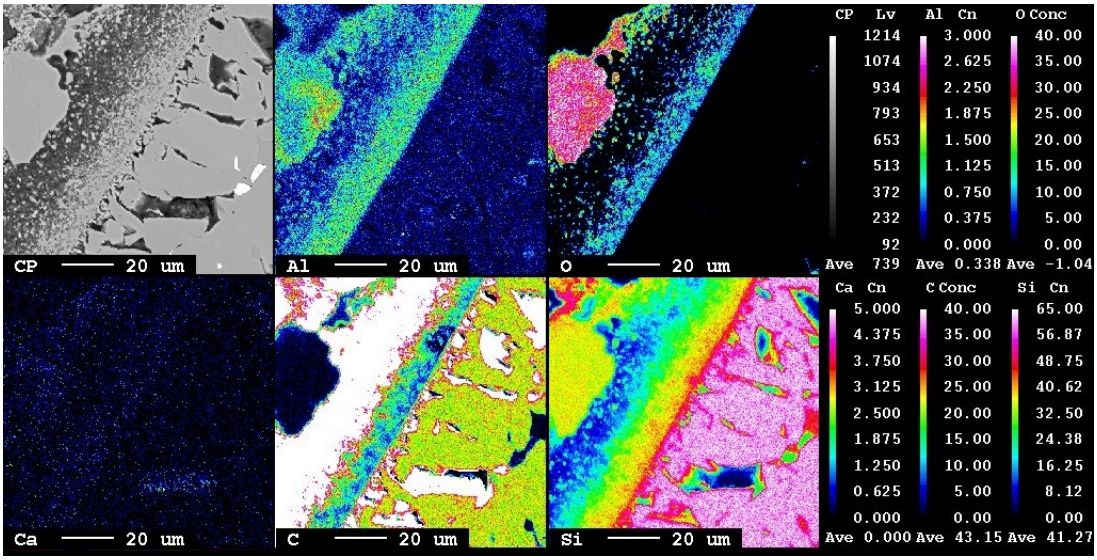

Figure 4.68: Element mapping of the FS4 sample surface using X-ray photons.

marked with a red dot shows that the grains are surrounded by a layer of SiC. The analysis is given in table B.9 in appendix B. Analysis was also performed on the transformation in the binder phase, and this was also determined to be SiC. The structure of this silicon carbide looks more like the SiC found in sample V5 (unintruded sample) than that found in sample V4, V6, V7 and V8 caused by intrusion.

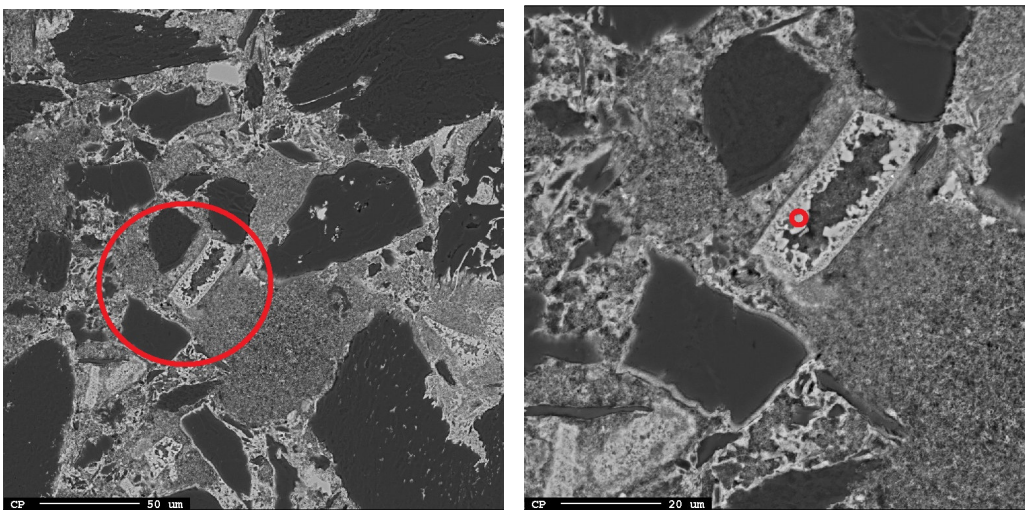

(a) **(b)**

Figure 4.69: EPMA images from the interior of sample FS4.

4.3.2 Sample FS5

For the second experiment performed in the Entech furnace, with sample FS5, modifications to the furnace were made to prevent the oxidation of silicon. A additional lid was manufactured to cover the top of the crucible, and the crucible was moved 6 cm higher in the furnace. These modifications were the only difference between sample FS5 and FS4; the crucible was still only filled with silicon, and the heating profile was similar to the one for sample FS4. The temperature profile for both experiments can be seen in figure 3.8 in section 3.2.1 in the Experimental chapter.

Depsite the modifications on the furnace setup, heavy oxidation of silicon in the crucible seems to have occurred during the experiment. This was evident from the visiual inspection after the experiment, see figure 4.70. From these images, it looks as though only smaller portions of the sample surface have been covered by silicon, and that the silicon has only partially melted. It is also observed that the upper part of the sample, which has not been subjected to liquid silicon, is covered in a layer of what might be condensed SiO(g).

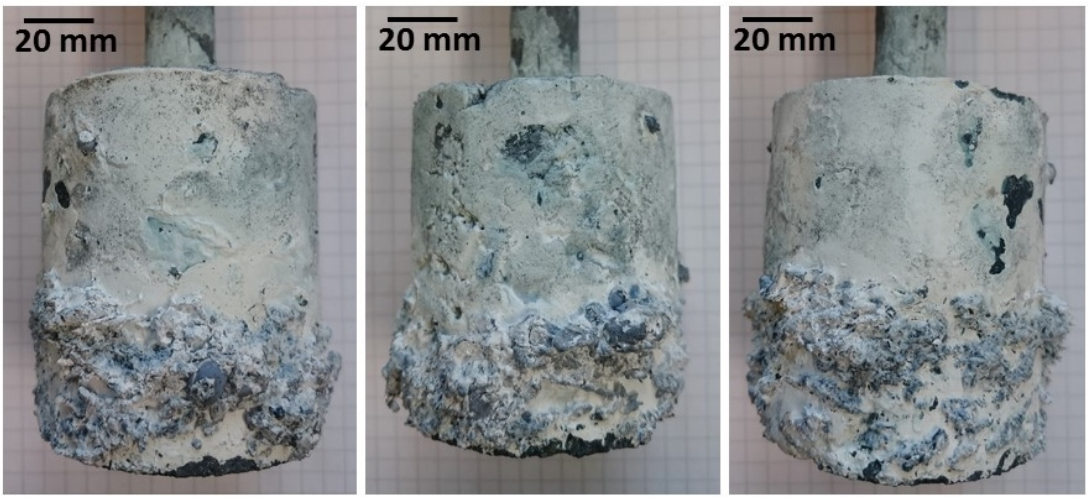

Figure 4.70: Visual inspection of sample FS5 in different views, after exposure to liquid silicon in the Entech furnace.

Inspection of sample FS5 using CT confirms that only very small portions of the sample surface have been covered by silicon. When inspecting the sample surface more closely, it is observed that the outer 1 mm of the sample has increased densities compared with the rest of the carbon lining.

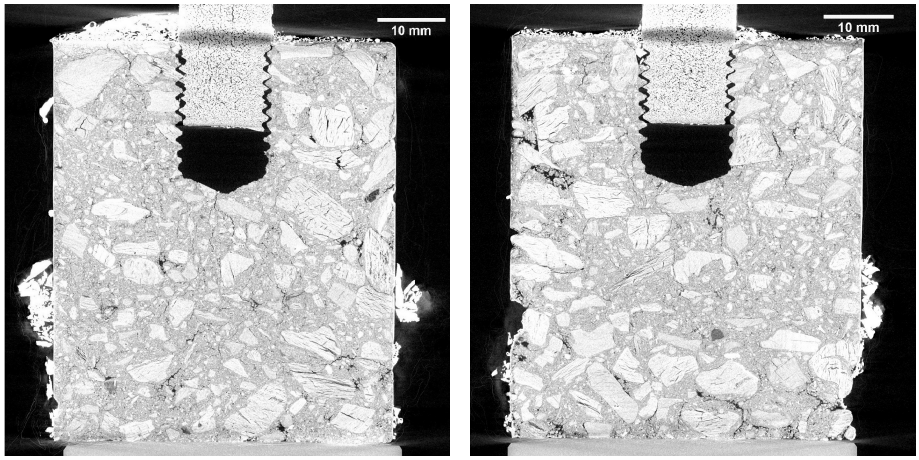

(a) X-Z direction **(b)** Y-Z direction

Figure 4.71: Orthogonal views in X-Z and Y-Z direction of sample FS5 after exposure to silicon in the resistance furnace.

When comparing scans of the areas with increased density with scans taken before exposure to silicon in the Entech furnace, it is determined that the increased density is due to a deposit on the surface rather than transformation of the outer surface layer. This deposit is assumed to be condensed SiO(g). Figure 4.72 shows scans taken 2 cm from the top of sample FS5 both before and after exposure to silicon and SiO(g).

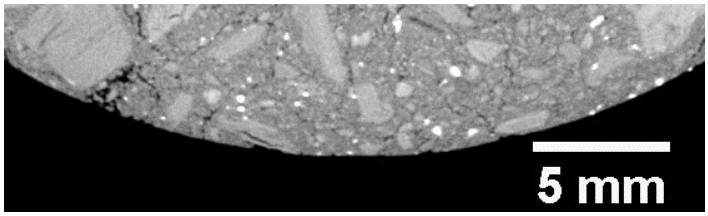

(a) Before furnace experiment

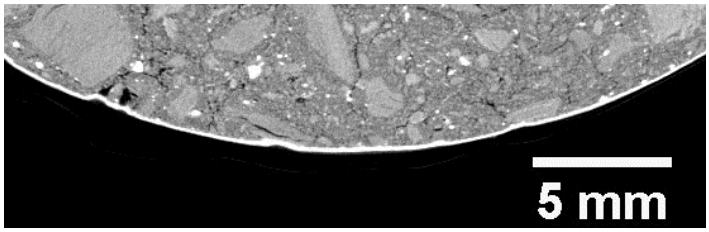

(b) After furnace experiment

Figure 4.72: Deposit of solid layer on the surface of sample FS5, 2 cm from the top of the sample.

When investigating the sample surface using EPMA, both silicon carbide and silicon oxide was found surrounding the surface. Figure 4.73 shows an image obtained from the backscattered electrons, showing the sample surface and the surrounding components. The numbers on the figure are explained below.

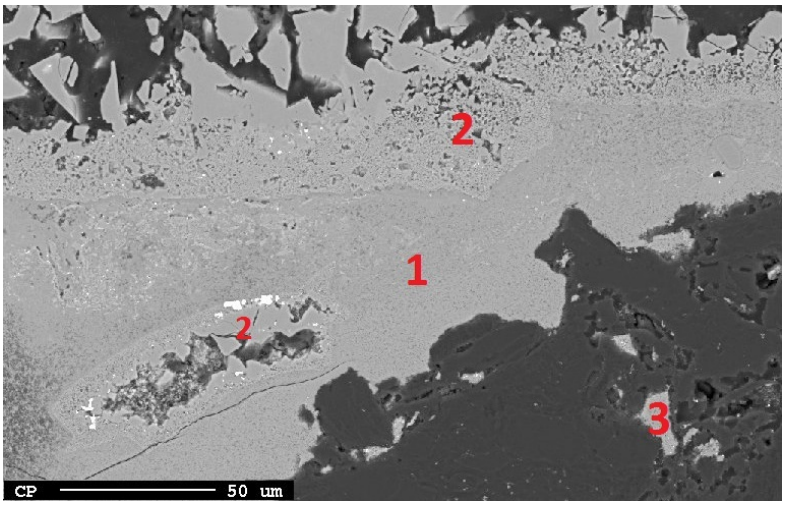

Figure 4.73: EPMA images from the exterior and surrounding furnace content of sample FS5. Number 1 and 3 marks areas with SiO_2, while number 2 marks areas with SiC.

The different species surrounding the sample was analyzed using the emitted X-ray photons to map the sample surface. This mapping is shown in figure 4.74. From this, it is possible to determine that there is a large amount of oxygen present in the silicon lying directly on the sample surface, shown as number 1 in figure 4.73. This is probably the deposit of condensed SiO(g) observed in figure 4.72. It is also noted that the area marked with number 2 contains significant amounts of carbon, and an analysis of this area show that this phase is silicon carbide. Allthough no intrusion could be observed using the CT, investigation using the EPMA shows that SiO_2 is present also inside the carbon lining sample, such as in the area marked with number 3 in figure 4.73.

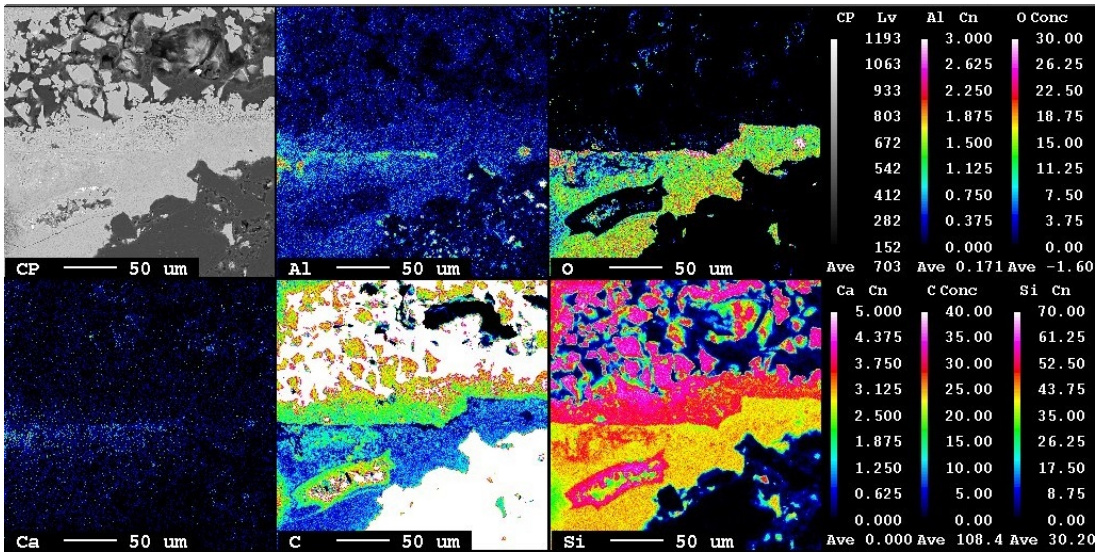

Figure 4.74: Element mapping of the FS5 sample surface using X-ray photons.

4.3.3 Sample FS6

Sample FS6 was exposed to silicon and slag using the same furnace modifications as for sample FS5. Slag was added to prevent the oxidation of silicon that was observed on the surface of sample FS4 and FS5, which is assumed to have occurred during heating in the Entech furnace. It can be seen from figure 3.8 in section 3.2.1 that this addition increased the heating rate of the furnace as the temperature got above 1000°C, and it also increased the maximum temperature from 1475°C to 1500°C during the experiment.

From the visual inspection, see figure 4.75, it looks as though the slag has mixed slightly with the silicon. It is also observed that the section of the sample that has been above the slag has been shielded from any SiO(g). Even though lumps of unmelted furnace content can be observed at the sample surface, it looks as though some of the slag and the silicon has melted almost completely.

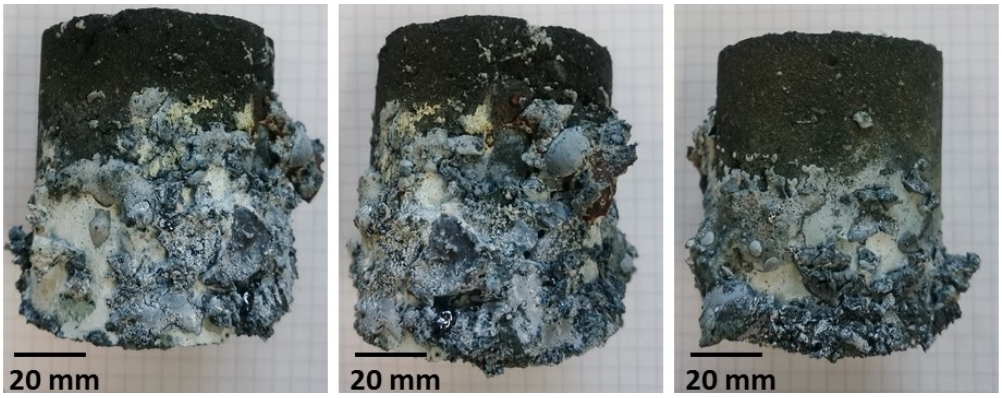

Figure 4.75: Visual inspection of sample FS6 in different views, after exposure to liquid silicon and slag in the Entech furnace.

During inspection of the CT scans from sample FS6, it was observed that very little of the furnace content is in direct contact with the sample surface. As for the other two experiments in the Entech furnace, much of the furnace content is concentrated in big lumps. In the areas were the furnace content is in direct contact with the sample surface, the wetting of the surface seems sufficient, but no intrusion of furnace content into the sample can be observed from the CT images.

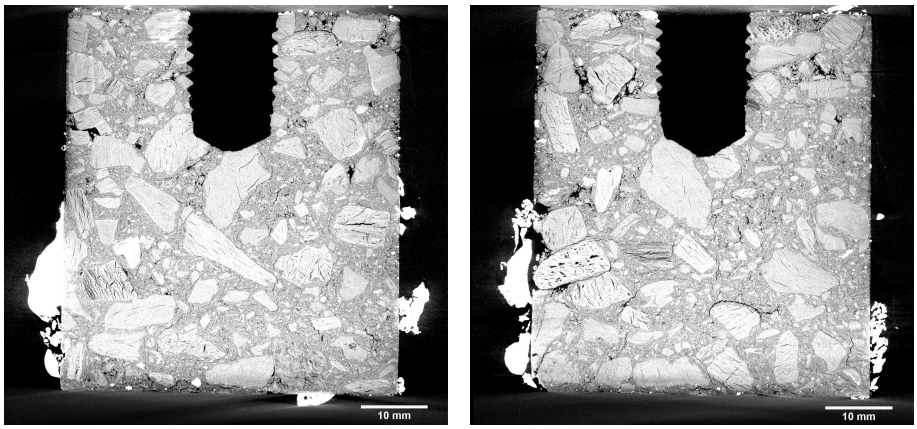

(a) X-Z direction **(b)** Y-Z direction

Figure 4.76: Orthogonal views in X-Z and Y-Z direction of sample FS6 after exposure to silicon and slag in the resistance furnace.

When inspecting the X-Y cross sections from the sample, the same trend as in the orthogonal views can be observed; while some areas show good wetting between melted silicon+slag and the sample surface, other areas are only surrounded by unmelted lumps of furnace content. One example of each area is shown in figure

4.77a and 4.77b, respectively. In figure 4.77a, it is observed that while the silicon has wetted the surface, it has not wetted the inside of the open pore.

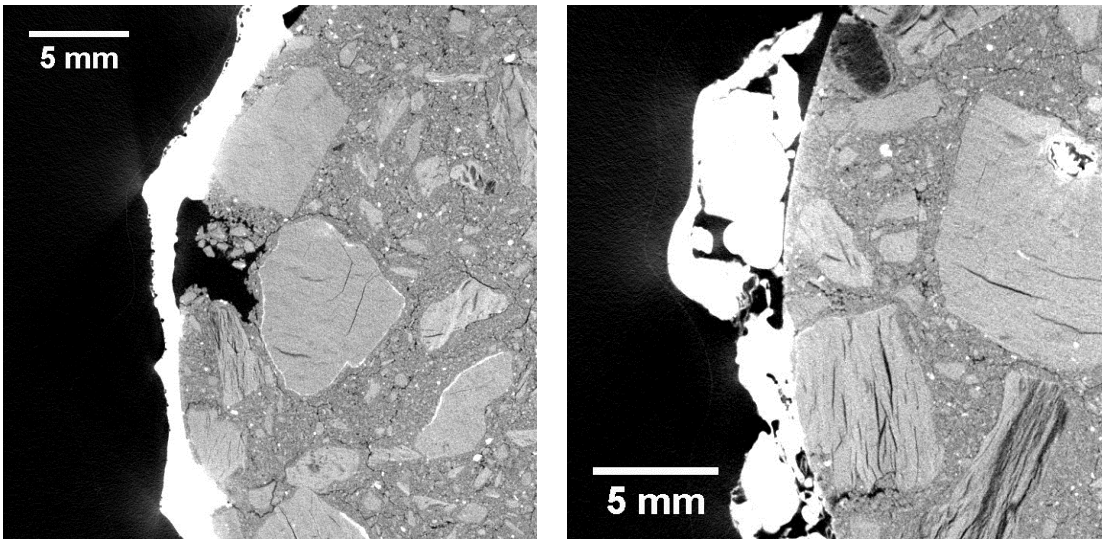

(a) Melted **(b)** Unmelted

Figure 4.77: Different sections of sample FS6 covered by unmelted and melted furnace content.

When investigating sections of sample FS6 in EPMA, it was observed that the investigated area had not been wetted by the liquid silicon. It is assumed that the investigated section is more similar to the area in figure 4.77b than figure 4.77a. Figure 4.78a shows the surface of the carbon lining with surrounding furnace content, where the lining sample surface has been highlighted by a red line. Figure 4.78b shows the circled area in figure 4.78a in higher magnification. Mapping of this area was performed by using the emitted X-ray photons and the result is given in figure 4.79. From this, it is possible to determine that the sample surface has been in contact with some silicon and silicon dioxide, and that there is a layer of silicon carbide surrounding the silicon further from the sample surface. The black strip running across the image is not carbon, but a void filled with epoxy. It is also observed that the mapping of this area contains no Ca or Al, meaning that this area has not been exposed to slag. The sample surface is again marked by a red line.

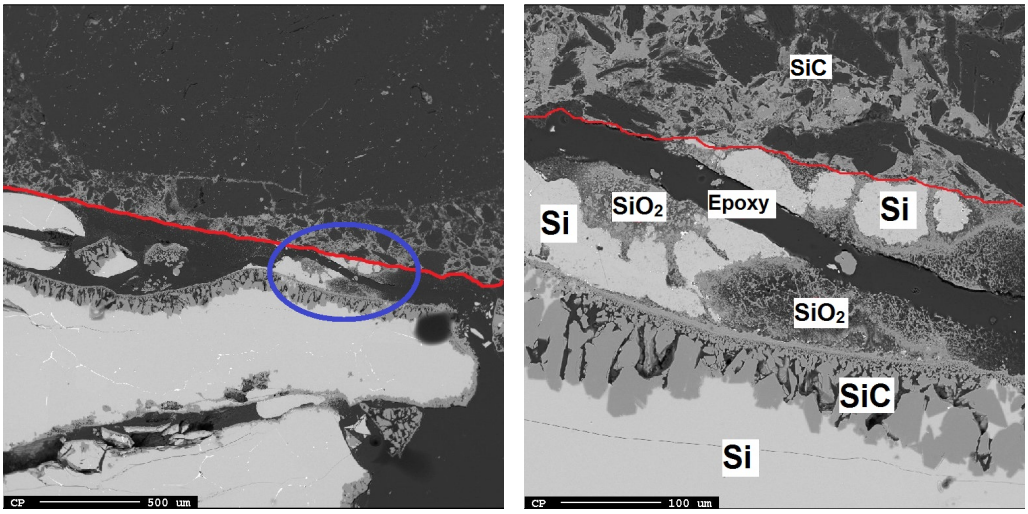

(a) (b)

Figure 4.78: EPMA images from the exterior and surrounding furnace content of sample FS6.

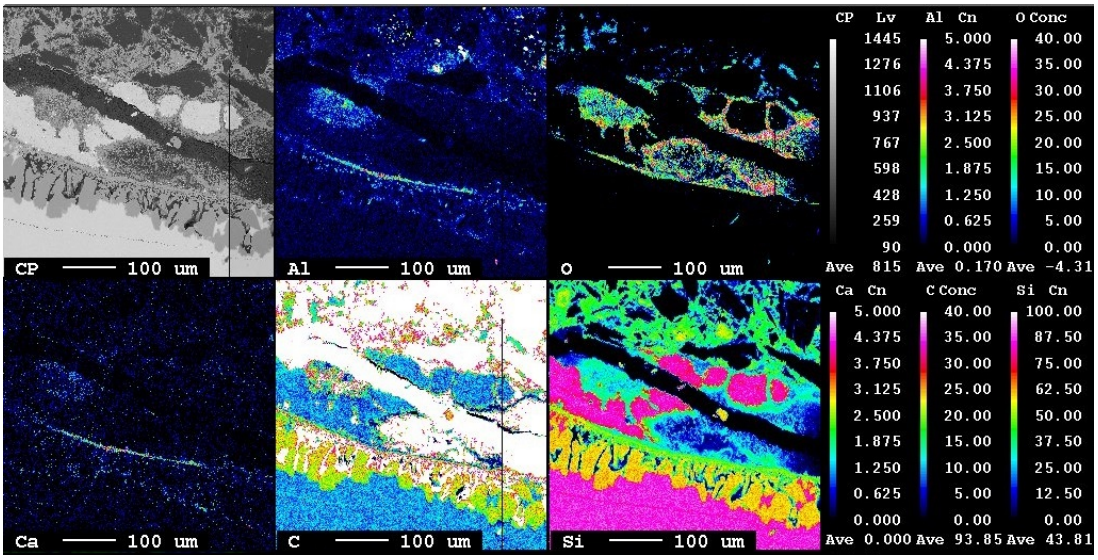

Figure 4.79: Element mapping of the FS6 sample surface using X-ray photons.

From these images, it is observed that SiC has formed in the binder phase, similar to the observations in V5 and FS4.

4.4 Sessile drop furnace

Three experiments were conducted in the sessile drop furnace to investigate wetting on, and intrusion into, different constituents of the carbon lining. One substrate was made from an anthracite grain, and contains only pure calcined anthracite, while one substrate was cut from an area of the lining with only tar pitch binder phase and small fractions of anthracite, to investigate intrusion into the binder phase. The last substrate was made with the mixed tar pitch lining containing both larger anthracite grains and binder phase. All three substrates were subjected to pure silicon with Ar as the shielding gas. After furnace experiment, the substrates were cut into semi cylinders and cast in epoxy for inspection using EPMA.

4.4.1 Anthracite grain

From images captured during the sessile drop experiment with silicon on anthracite, it is observed that the wetting between the silicon and the anthracite substrate has been good, but not complete. Figure 4.80 shows melting of the silicon on anthracite, from beginning of melting to the termination of the experiment. It is observed that the substrate is not 100% level, making it somewhat difficult to measure the final contact angle, θ_f, between the silicon and anthracite. The angle has been determined at approximately $\theta_f = 40°$.

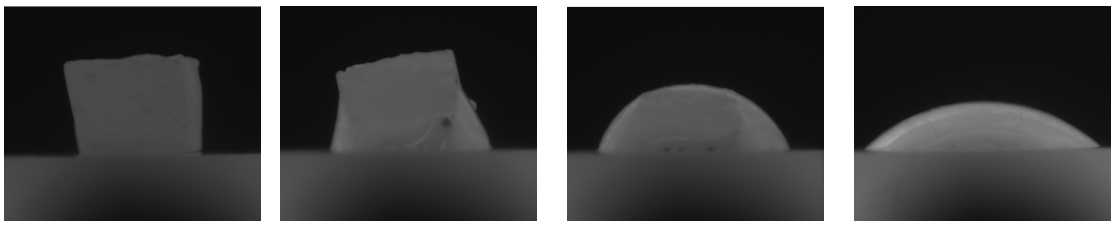

(a) T=1434°C t=15 min 0 s **(b)** T=1448°C t=17 min 50 s **(c)** T=1450°C t=18 min 18 s **(d)** T=1480°C t=24 min 34 s

Figure 4.80: Images from the sessile drop experiment with silicon on anthracite.

An image was obtained using an optical microscope, to determine the intrusion depth of silicon into the anthracite substrate. Figure 4.81a shows the substrate in 2.5x magnification, and it is noted that intrusion has occurred into cracks in the grain, and that wetting has been very good between silicon and the anthracite. Figure 4.81b shows the sample surface in 20x magnification, and it is observed that a third phase (apart from silicon and carbon) has formed on the anthracite surface. The same phase can be found inside the cracks, and is assumed to be SiC.

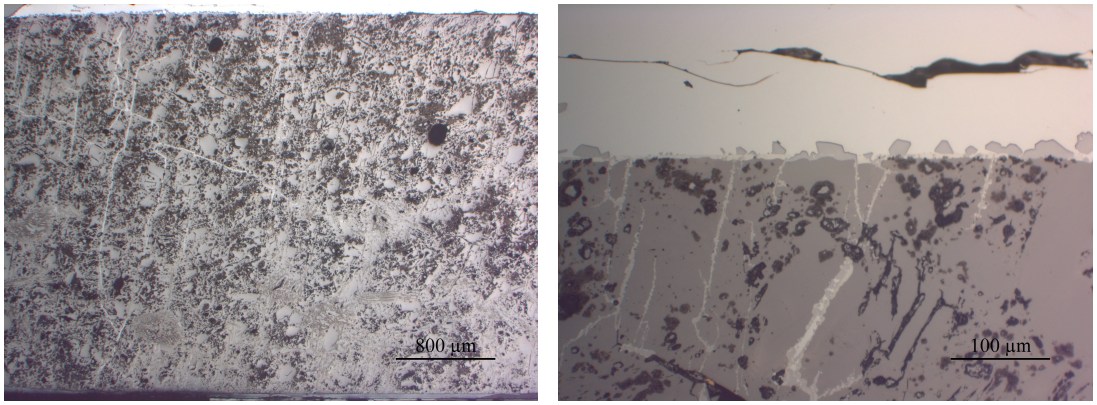

(a) 2.5x magnification **(b)** 20x magnification

Figure 4.81: Investigations of the anthracite substrate using an optical microscope.

This formed phase at the substrate surface was analysed using the EPMA. The analysis is given in table B.10 appendix B, and confirms that the phase is indeed SiC. An analysis was performed on the silicon carbide found inside the cracks of the anthracite grain as well, which is given in table B.11. This shows that the SiC inside the grains has significantly larger percentage of silicon than the SiC on the substrate surface. Backscattered electron images of the SiC on the substrate surface and inside the grain cracks were obtained using the EPMA, and given in figure 4.82.

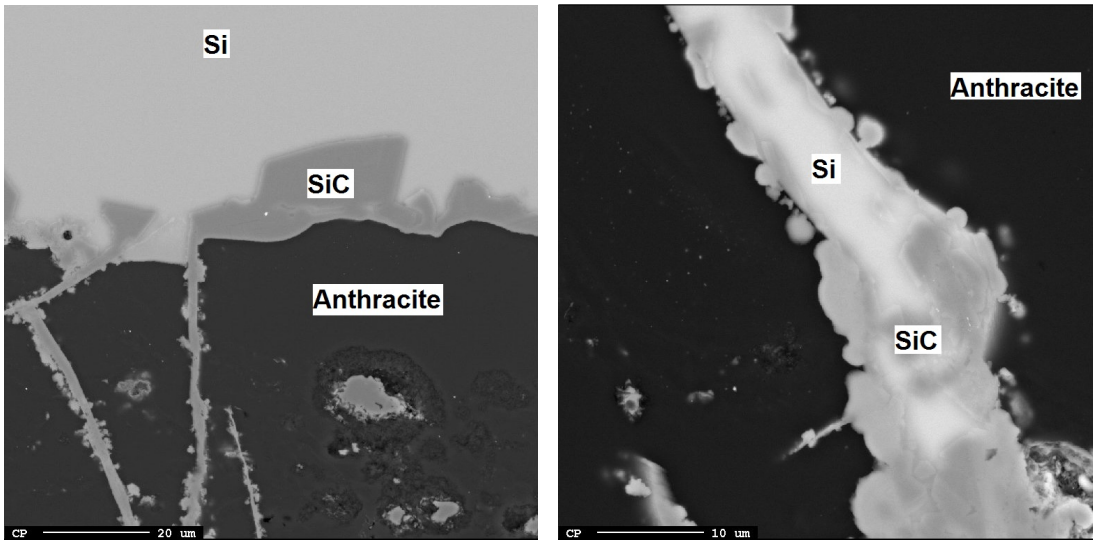

(a) Substrate surface **(b)** Inside crak

Figure 4.82: EPMA imaging of the SiC formed in and on the anthracite substrate.

4.4.2 Binder phase

From the images captured by the furnace camera during the experiment with silicon on the binder phase substrate, it is observed that the wetting between silicon and binder phase has been almost complete. The final contact angle, θ_f is measured at $\theta_f = 10°$. It is also noted that a peak seems to have formed during melting.

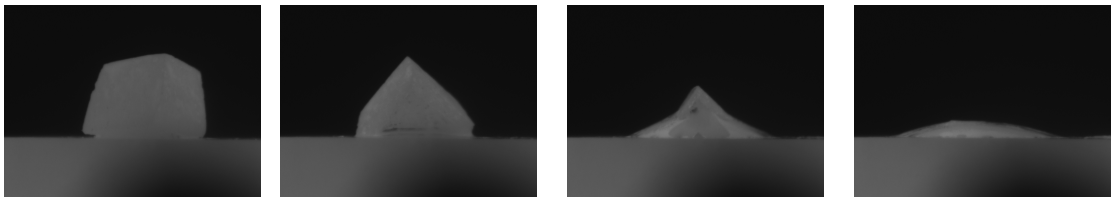

(a) T=1442°C t=15 min 22 s **(b)** T=1445°C t=16 min 0 s **(c)** T=1446°C t=16 min 19 s **(d)** T=1447°C t=16 min 25 s

Figure 4.83: Images from the sessile drop experiment with silicon on carbon lining.

The substrate was made by cutting a piece from an area of the mixed carbon lining with few large anthracite grains. When inspecting the substrate using optical microscopy after the experiment, it was noted that the selection of the substrate has been partially successful; the substrate contains only 4 grains larger than 800 μm, with lengths of 850μm, 890μm, 900μm and 1100μm. It is noted that the intrusion has traveled almost completely through the subsrate, leaving only 300 μm of the total substrate height of 3000μm unintruded. Figure 4.84a shows an image of the binder substrate captured using the optical microscope at 2.5x magnification, where the intrusion is marked by a red line. Figure 4.84b shows the surface in 20x magnification, and it is noted that nearly all of the binder phase looks transformed and that the anthracite grains are covered in SiC.

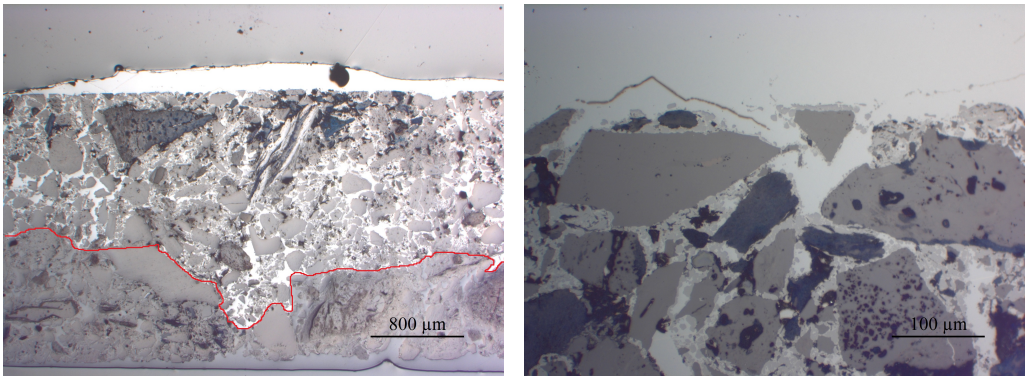

(a) 2.5x magnification **(b)** 20x magnification

Figure 4.84: Investigations of the binder phase substrate using an optical microscope.

The substrate was investigated using backscattered electron imaging in the EPMA, and analysis confirms that almost all of the binder phase in the intruded areas has been transformed to silicon carbide. Figure 4.85 shows an image from the surface, where it is noted that all of the binder phase is gone and that the anthracite grains have started transforming as well.

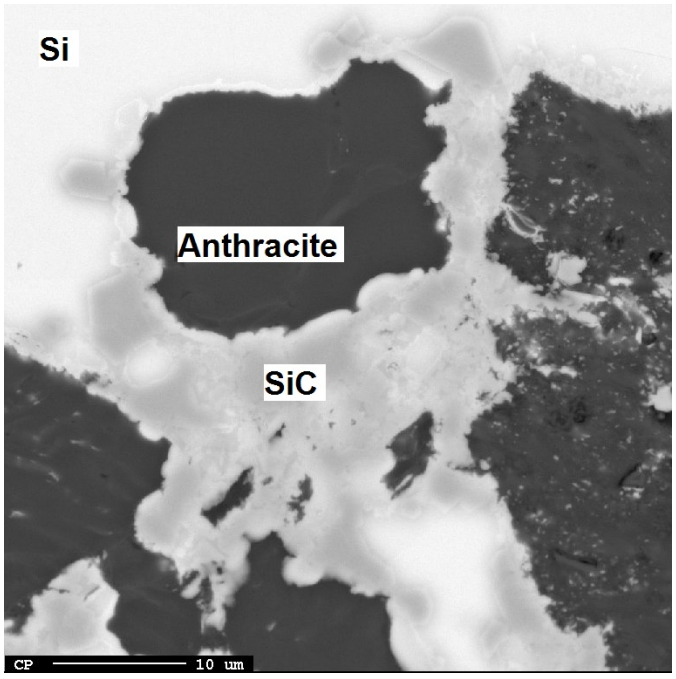

Figure 4.85: Backscattered electron imaging of the binder substrate using the EPMA.

4.4.3 Carbon lining sample

The last experiment was conducted with silicon on a substrate cut out from a section of lining containing both anthracite grains and binder phase. This experiment was terminated before all of the silicon was melted due to unexpexted and vigorous movement of the silicon piece on the substrate as the melting started. Images taken during the experiment are shown in figure 4.86, where it can be seen that the silicon starts melting in figure 4.86b, and starts tipping in figure 4.86c, only 50 seconds after figure 4.86b. The experiment was terminated shortly after the image in figure 4.86d as captured. During visual inspection of the substrate after cooling, it was noted that the whole substrate surface was covered in silicon, and it was decided to further investigate the substrate using optical microscope and EPMA.

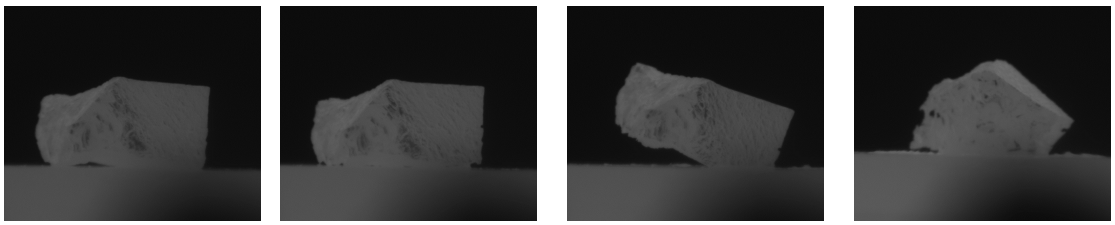

(a) T=1433°C t=13 min 50 s **(b)** T=1434°C t=14 min 10 s **(c)** T=1438°C t=15 min 01 s **(d)** T=1440°C t=15 min 27 s

Figure 4.86: Images from the sessile drop experiment with silicon on carbon lining.

Investigation of the substrate using the optical microscope shows that intrusion has been substantial in this substrate as well, but less than the intrusion observed in the binder substrate. This could be due to the larger grains in the bottom of substrate slowing down the intrusion, but also due to the fact that this experiment was terminated 5 minutes earlier than the experiment with binder phase. Figure 4.87a shows the carbon lining substrate in 2.5x magnification, where the intrusion depth is marked with a red line. Figure 4.87b shows the surface of the substrate in 20x magnification, where it can be seen that the binder phase has been transformed while the anthracite grains look unaffected.

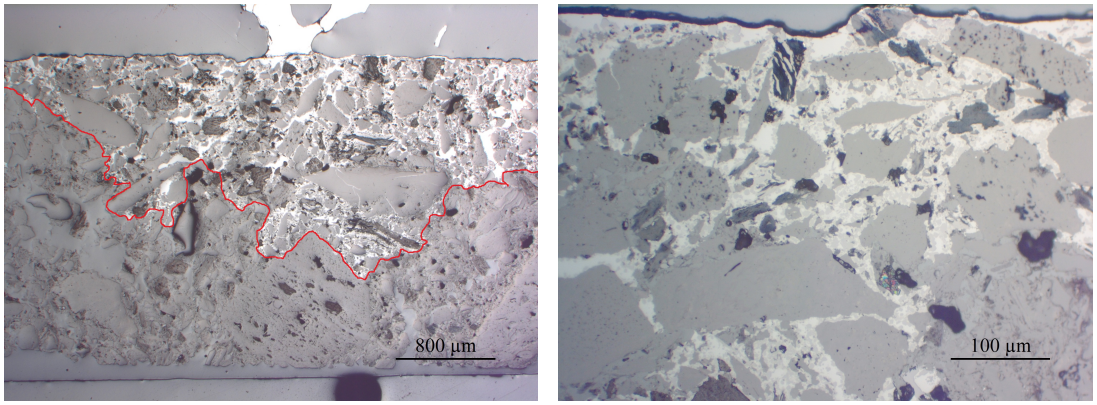

(a) 2.5x magnification **(b)** 20x magnification

Figure 4.87: Investigations of the carbon lining substrate using an optical microscope.

The carbon lining substrate was investigated using backscattered electron imaging in EPMA, which confirmed that most of the binder in the intruded area was transformed to SiC. It was observed that while the larger grains in the interior of the substrate look unaffected, the grains at the surface are partially transformed to SiC. Figure 4.88 shows an image from the substrate sample, showing how the anthracite grains in this area are partially transformed and surrounded by SiC.

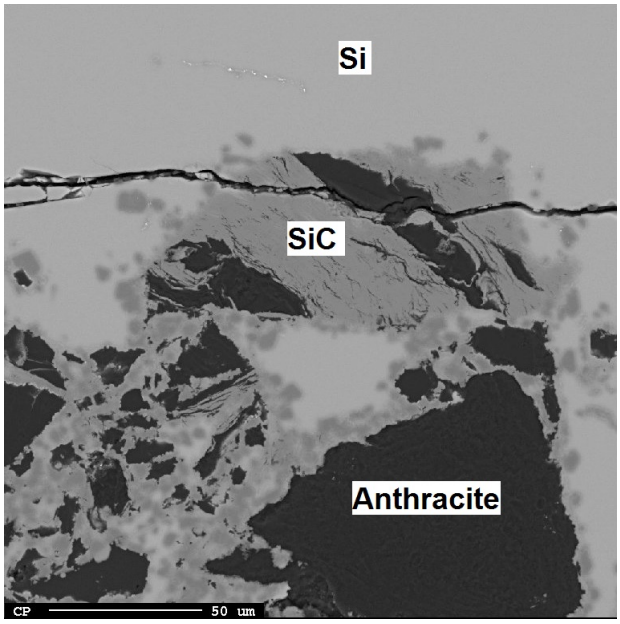

Figure 4.88: Backscattered electron imaging of the carbon lining substrate using the EPMA.

Chapter 5

Discussion

This chapter will provide a discussion of the previously presented results, and has been divided into three sections: one which discusses the internal morphology of the different samples, one which discusses the observed wear mechanisms, and one which discusses the choice of furnaces and investigation methods used in the experimental work.

5.1 Internal morphology

In the CT scans performed prior to the furnace experiments, it was observed that the density in the layered samples varied depending on position relative to the ramming layers. The top of the layers in each sample was more densely packed than the rest of the sample, and the bottom of each layer was more porous and loosely packed. This was the case for all three types of layered samples, despite the difference in binder type, layer height and ramming tool. Figure 5.1 shows the density variations in sample V5, both in the CT images showing the orthogonal view in X-Z direction, and in the density calculations performed for each cross section and plotted as a function of height.

It was also observed that the density variations increased as the thickness of the layers increased. The most significant difference between the density at the top of a layer and the density at the bottom of a layer was found in sample V8, which contained a single layer of 8.2 cm. In this sample, the density varied from 1452 kg/m^3 at the top of the sample to 1436 kg/m^3 in the bottom of the sample, which can be seen in figure 4.11. In sample V4 and V5, where the layers were approximately 6-6.5 cm, the density varied between approximately 1450 kg/m^3 in the top of the layers to 1436 kg/m^3 in the loosely packed layer bottom sections.

In sample V6 and V7, which had the thinnest layers of approximately 2 cm, the density variations were significantly smaller, only from 1443 kg/m^3 at the layer tops to approximately 1437 kg/m^3 in the layer bottoms.

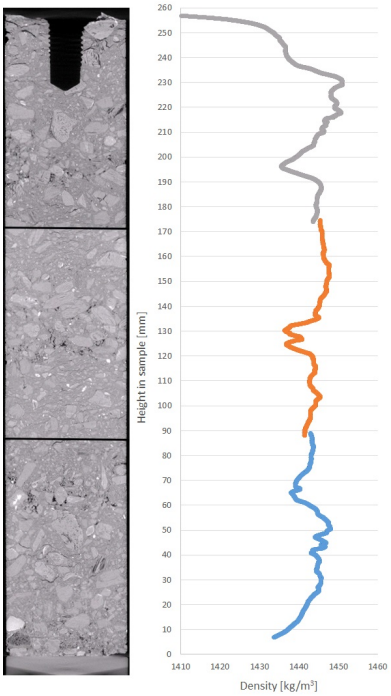

Figure 5.1: Density variation across the height of sample V5, showed both in the orthogonal view (left hand side) and in the density calculations for each cross section plotted as a function of height (right hand side).

When the FS samples were investigated using CT, no significant density variation could be observed through the height of the sample. It was, however, noted that variations could be observed across the X-Y cross sections. It was observed that segregation of the larger grains from the rest of the paste had occurred during preparation of the samples, and that the larger grains had accumulated in one side of the sample, see figure 4.15 in the Results chapter. This phenomenon was illustrated in figure 2.9 [22] in the Theory chapter, which showed that larger particles of a dry mix collects towards the edges of the container as segregation occurs during filling. Similar segregation was observed in the preliminary project work and, as with the samples in the project work, it was determined that the segregation did not impact the density variation across the height in FS4-FS7.

Table 5.1 shows the sample structure, average density and density variation of all

the samples, showing that the variation of density is dependent on the layer thickness, and that the FS samples without the layering has the smallest variation. It is noted that, even in the samples with very visible density variation from the CT images, the measured density variation is quite small.

Table 5.1: Internal structure, average density, ρ_{ave} and density variations for all samples.

Sample no.	Structure	$\rho_{ave}[\frac{kg}{m^3}]$	ρ variation $[\frac{kg}{m^3}]$	ρ variation [%]
$V8$	8.2 cm layer	1441	16	1.11
$V5$	6.5 cm layers	1442	15	1.04
$V4$	6.5 cm layers	1439	13	0.90
$V7$	2 cm layers	1440	10	0.69
$V6$	2 cm layers	1441	10	0.69
$FS5$	Solid	1434	4.3	0.30
$FS4$	Solid	1443	4.1	0.28
$FS6$	Solid	1442	3.0	0.21
$FS7$	Solid	1436	2.7	0.19

The density variations (%) in the layered samples were plotted against the layer thickness, and the plot is given in figure 5.2. This shows that there is a linear correlation between the layer thickness and the density variation in a sample.

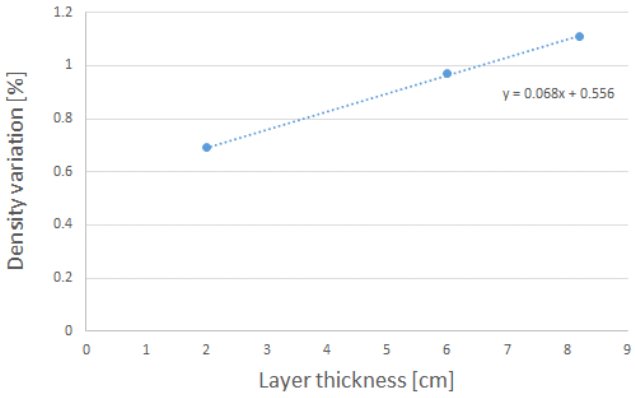

Figure 5.2: Density variation (%) plotted as a fuction of layer thickness, for the layered samples V4-V8.

The average density of each sample was measured before the experiments, and it was noted that the average densities of the layered samples varied quite little,

from 1439 kg/m^3 to 1442 kg/m^3. The density of the eco binder was slightly less compared to the other binders, but the density of the added silicon fine fractions in the paste for sample V6 and V7 seem to have cancelled out this density difference. It was observed from the CT cross sections that the density of the binder+fine fractions in sample V6 and V7 looked higher than in the rest of the samples, but this density difference can not be observed in the average densities for the samples.

Unlike the observations for the density variations, the amount of cracks that could be detected in the different carbon lining samples did not depend on layer thickness or structure. The amount of cracks that could be found in the layered samples V4 and V5 was the same amount as in the FS samples, which were were made from the same paste, but with different tools and giving different structures. It is noted that the FS samples were baked with faster heating rates than the layered samples made with the same paste. When carbon lining is heated, gases form inside the lining due to the carbonization of the binder, as the volatiles in the binder vaporize. As the gases force their way out of the lining, the lining expands to allow the gas to escape, before shrinking down to approximately original size again. When this volume change occur, cracks form in the lining. If the lining is heated faster, a larger volume of gas is formed and has to leave the lining at the same time. This leads to bigger volume changes, which again lead to more cracks in the lining. From this, it would be expected to find more cracks in the FS samples. However, the FS samples, which were baked faster than the layered samples, were also smaller than the layered samples, which could have cancelled out the effect of the difference in heating rate.

The biggest difference in regards to the formation of cracks was observed between the samples with different binder types; very few cracks were observed in the resin sample, while the samples with eco binder contained some cracks randomly distributed in the samples. The tar pitch samples, both layered and FS, had the most cracks of the three lining types, and the cracks in these samples were often longer than those found in the samples with eco binder. The layered samples with tar pitch binder and the layer samples with eco binder was baked using the same temperature profile, and from this, it could be assumed that using eco binder decreases the amount of cracks in the carbon lining. However, it is noted that both sample V4 and V5 (tar pitch) and V6 and V7 (eco) were cut from larger rammed carbon lining lumps, and that the crack formation might depend on the position in the lump from where the different samples have been collected. For instance, the edges of a big sample might have to expand more because more gas has to travel through this area. It was not noted from which part of the bigger lumps sample V4-V7 were collected from, but it is a possibility that V4 and V5

are both from the edge of the tar pitch carbon lining lump, while V6 and V7 both are collected from the middle of the eco carbon lining lump. This speculation is supported by the fact that sample V8, which was cut from the middle of a bigger carbon lining sample, had the fastest heating rate of all the layered samples but the least amount of cracks. This uncertainty makes it difficult to conclude on how the choice of binder phase influence the crack formation.

The extent of grain crushing in those of the layered samples prepared using the star shaped ramming head, sample V4, V5 and V8, was significant and in the samples prepared with this tool, almost all the larger anthracite grains were crushed in the top 2-3 mm of each ramming layer. This was also observed in the preliminary project work [5], where all the layered samples were prepared using this tool, and it was then assumed that the ramming head was the main cause of the grain crushing. By comparing the top of the ramming layers in the samples prepared with the star shaped ramming head to the same areas in the samples prepared with a flat ramming head, this assumption was confirmed; in sample V6 and V7, prepared with a flat ramming head, almost no crushed grains could be observed. The few examples of crushed grains found in sample V6 and V7 could be caused by the edge of the ramming head. It is also a possibility that thermal cracking could have occurred when the grains were calsined, but from the CT cross section scans it looks as though the grains have been crushed and not just cracked. Figure 5.3 compares the top of a ramming layer in sample V5 with the top of a ramming layer in sample V7.

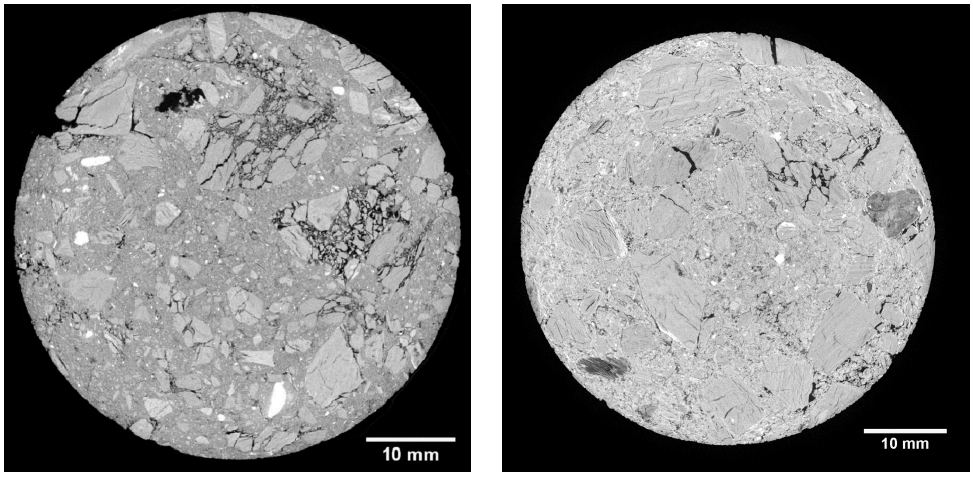

(a) V5 **(b)** V7

Figure 5.3: Cross sections from the top 1 mm of a ramming layer in sample V5 (star shaped ramming head) and V7 (flat ramming head).

No significant grain crushing was observed in the FS samples. This was expected, as these samples were compressed with a flat tool providing equal force across the sample cross section. This flat ramming tool was not the same as that used on sample V6 and V7, as the ramming tool used in sample V6 and V7 had a smaller area of impact. Still, the FS samples and sample V6 and V7 had about the same amount of crushed grains. Figure 5.4 compares the top section of sample FS4 with the top of a ramming layer in sample V6, and it is noted that both cross sections show only two cracked grains.

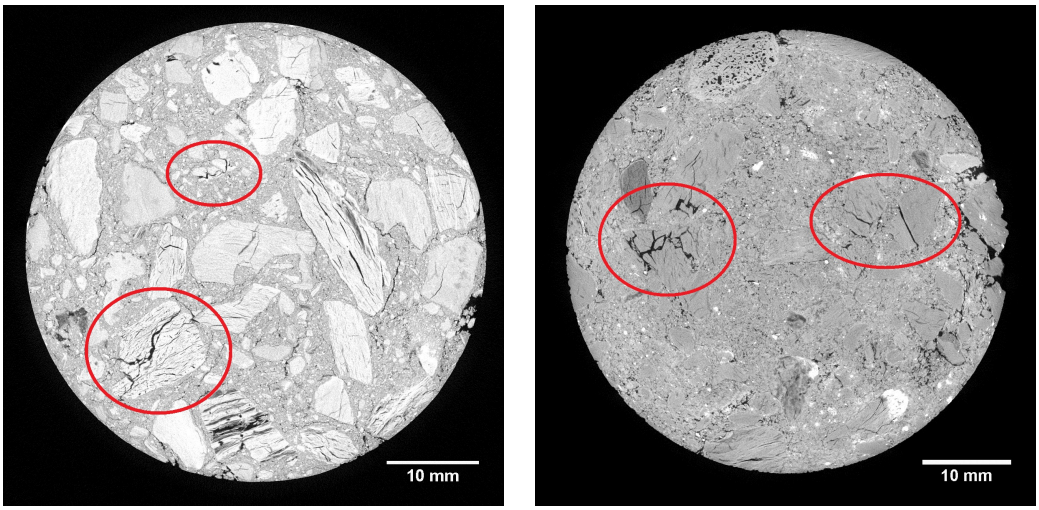

(a) FS4 **(b)** V6

Figure 5.4: Cross sections from the top 1 mm of a ramming layer in sample FS4 and V6.

5.2 Wear of carbon lining

5.2.1 Intrusion

Intrusion could be observed in both of the layered samples cycled around the solidification temperature of silicon, sample V4 and V8. In sample V4, intrusion was observed in the entire bottom 1/3 of the sample. The intrusion in this part had occurred all through the sample, and it was difficult to determine whether the amount and location of intrusion depended on the layered structure. When inspecting parts of the sample surface of sample V4 using EPMA, it was confirmed that only silicon had intruded into the center of the sample, while the maximum slag intrusion depth was approximately 500μm. Figure 5.5 shows a backscattered electron image of the surface of sample V4, where it is observed that slag covers the entire sample surface in this area, while only silicon can be found further than 500μm into the sample. The red line marks the transition between the slag on the exterior of the sample and the silicon in the interior of the sample.

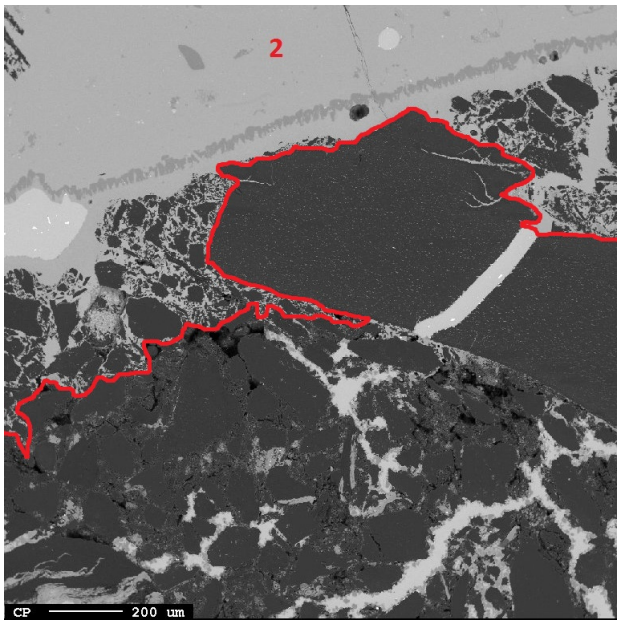

Figure 5.5: Backscattered electron image of sample V4 sample surface, showing the transition between slag and silicon.

In sample V8, the intrusion had occurred only in one side of the sample, and after comparing the CT scans with the visual inspection of the sample surface it was concluded that no visible intrusion had occurred where the sample was covered by slag. This concurred with the observations from V4, where no slag had intruded

further than 0.5 mm into the lining sample. In both sample V8 and sample V4, intrusion only occurred in the bottom parts of the lining sample and as in sample V4, it is difficult to determine whether the sample structure has had any impact on the intrusion in sample V8. Sample V8 was subjected to silicon and slag with the densest part of the sample facing down towards the crucible bottom. As an effect of this, intrusion has only occurred in the densest part of the sample. It is assumed that intrusion would have occurred in the porous part as well, if this had been covered by liquid silicon.

In the previously performed project work [5], no intruison occurred while using the induction furnace. This was assumed to be due to induction forces affecting the furnace content, as described in section 2.7.1, and thus preventing intrusion. It was observed in the experiments with sample V4 and V8, that as the temperature in the crucible was decreasing, the furnace power was turned off for short periods of time. This led to the assumption that the intrusion could have been caused by two phenomenons:

- The intrusion occurred as the silicon surrounding the lining sample solidified, which may have pushed the silicon into the sample.
- The intrusion occurred when the furnace power was switched off and the furnace was free of the induction forces.

To determine the cause of intrusion in sample V4 and V8, sample V5 was cycled from 1600°C to 1450°C while exposed to silicon and slag. Sample V5 was prepared in the same way as sample V4, and by cycling the temperature above the solidification temperature, the sample was exposed to silicon without induction forces present, while the silicon remained liquid throughout the experiment. Visual investigations of sample V5 after the furnace experiment showed that the bottom 3/4 of the sample had been covered by the furnace content, and it appeared as though the bottom half was exposed to liquid silicon. During investigation of the CT scans it was observed that no intrusion had occurred anywhere in this sample during temperature cycling above the solidification temperature of silicon. From this experiment, it would appear that the cause of intrusion in sample V4 and V8 was the solidification, not the furnace effects. However, from the CT scans of sample V5, it was also observed that a gap had formed between the furnace content and the sample surface, which could have prevented intrusion into the sample. Due to this, it was decided to test temperature cycling above the solidification temperature with two additional samples.

V6 and V7 were exposed to the same conditions as sample V5, with temperature cycling above the solidification temperature of silicon. Sample V6 was exposed to

silicon and slag, while sample V7 was exposed only to liquid silicon. Given the results from V5, intrusion should not have occurred in any of these samples, but from the CT scans, intrusion was observed in both. In both of the samples, intrusion had occurred 1.5 cm from the bottom of the sample, in what was assumed to be the bottom of the second-bottom ramming layer. This assumption was confirmed during inspection of the cross section scans, which showed high porosity and accumulation of larger anthracte grains in the intruded areas. Figure 5.6 shows the orthogonal view of sample V7 *after* exposure to liquid silicon compared with the calculated cross section densities from *before* exposure to silicon. This shows how intrusion has occurred in the porous bottom of the second-bottom layer.

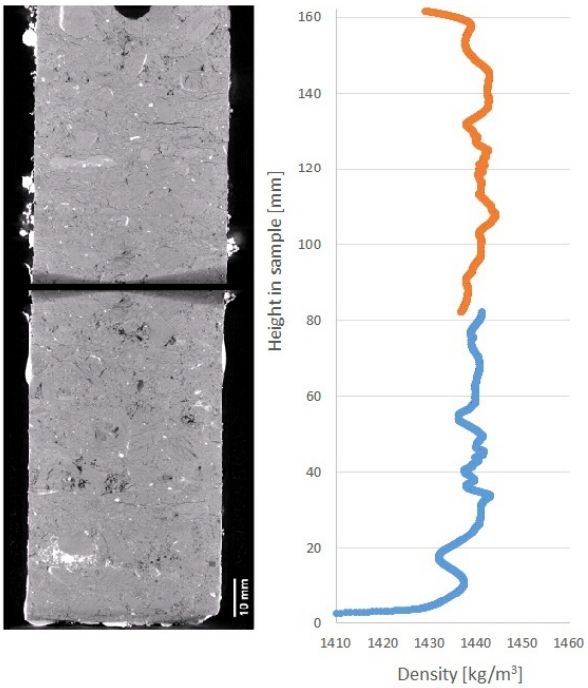

Figure 5.6: Orthogonal view in X-Z direction of sample V7 taken after exposure to silicon (left hand side) compared with the calculated cross section densities from before exposure to silicon (right hand side).

The intrusion into sample V6 and V7, cycled above the solidification temperature of silicon, was not as complete as in sample V4 or V8 which was cycled around the solidification temperature. Figure 5.7 compares the intrusion in sample V4 and sample V6 by showing cross section images from the most intruded areas. It was observed that the intrusion in sample V6 filled only voids and cracks in the sample, while the intrusion in sample V4 had occurred into the entire binder phase.

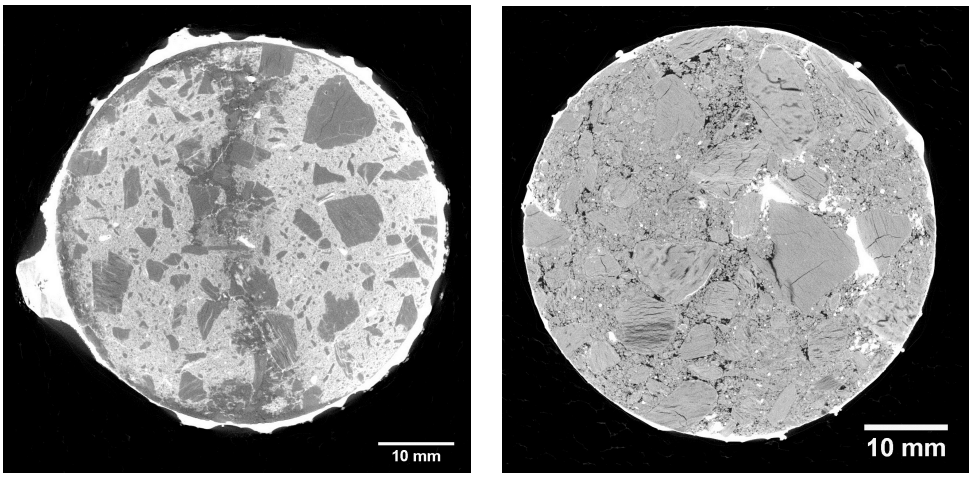

(a) V4 **(b)** V6

Figure 5.7: Intrusion into sample V4 and V6.

It was observed that slightly more intrusion had occurred in sample V7, exposed only to liquid silicon, than in sample V6 which was exposed to both silicon and slag. Figure 5.8 compares the intrusion into sample V6 with the intrusion into sample V7. It was also observed that the slag surrounding sample V6 had intruded 600 μm into the sample, and that only silicon was found towards the center of the sample. This was similar to the observations in sample V4.

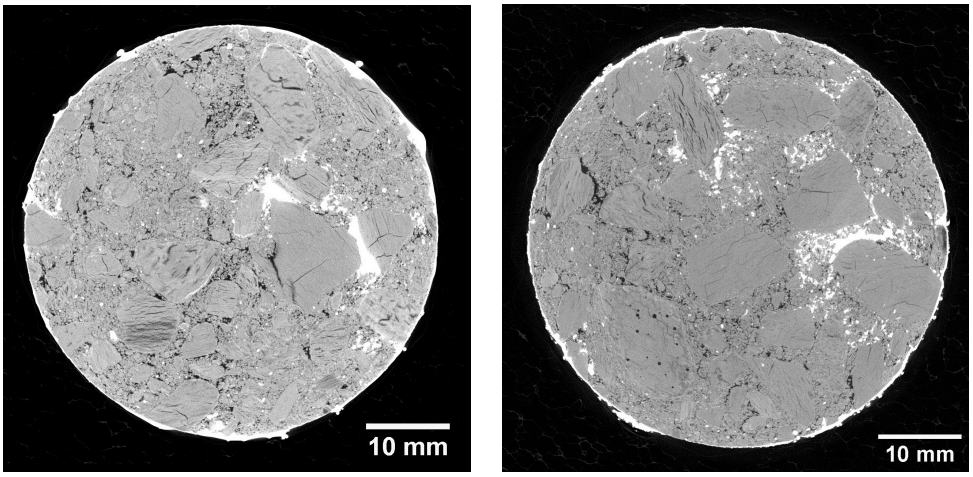

(a) V6 **(b)** V7

Figure 5.8: Intrusion into sample V6 and V7.

As the intrusion into sample V6 and V7 occurred to a lesser extent than in sample V4 and V8, it became easier to see what effect the sample morhology had on the intrusion. As previously mentioned, the intrusion occurred only in the porous bottom area of the second-bottom layer, where the samples had increased porosity. CT can only be applied to investigate the samples after completion of the experiment, and it is thus hard to speculate where the first intrusion of silicon into sample V4 occurred. It is speculated that the intrusion in sample V4 started in the porous bottom sections of layers in sample V4 as well, before spreading vertically inside the sample. As there is no way to determine if this was the case just by investigating images from after the experiment, this would only be speculations.

Due to the intrusion in both sample V6 and V7, it is assumed that intrusion would have occurred in V5, and that the intrusion was prevented by the formation of the gap between the carbon lining surface and silicon+slag. The gap could not be observed in the section that was analyzed using EPMA, shown in figure 5.9, but it was observed that a layer of SiO_2 had formed between the lining surface and the slag. The transition between slag and silicon oxide has been marked by a red line in the figure. It is speculated whether the formation of SiO_2 might have protected the sample from intrusion. Another explanation might be that the sample has been more exposed to oxygen than the other samples, which might have influenced the surface layer and prevented wetting from the liquid furnace constituents. There is no sure way to determine the cause of the observed gap, but as the experiments with sample V4, V6 and V7 showed that intrusion should have occurred in sample V5, it is assumed to be the cause of lack of intrusion into sample V5.

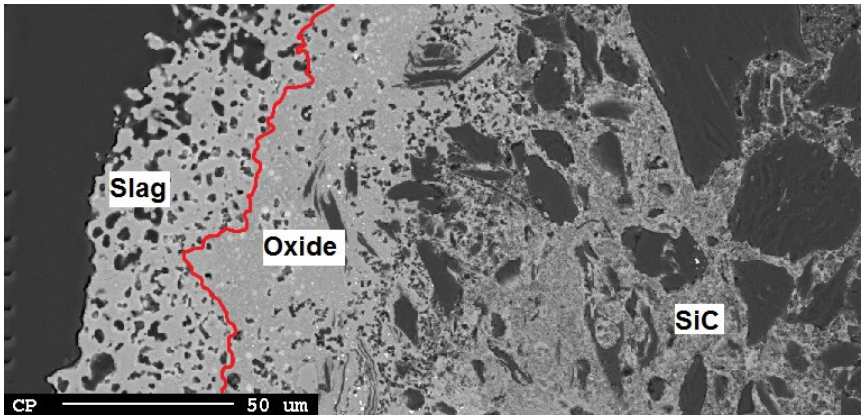

Figure 5.9: Backscattered electron image of sample V5 sample surface, showing how SiO_2 has formed between the slag and the sample surface.

CT scans of the FS samples that were exposed to silicon using the Entech furnace showed that very little melted furnace content could be found on the sample surface, and that no intrusion into any of the samples could be observed in the CT images. Investigation of the sample surfaces using EPMA showed that silicon could be found inside some of the samples, but always as silicon oxide or silicon carbide and never as pure, unreacted silicon. This could be due to reaction with SiO(g), and not intrusion of liquid silicon, more on this in section 5.2.2.

Compared with the experiments performed with sample FS4-FS6 in the Entech resistance furnace, the experiment with FS7 in the induction furnace gave much better melting of the furnace content, and thus much better wetting between the silicon and the carbon lining sample. This was probably due to the rapid heating rate, giving the silicon much less time to oxidate before melting. Even though the sample surface was sufficiently wetted by the silicon and slag, none of the furnace content had intruded into the samples. This was confirmed by the EPMA, where no intrusion of silicon or slag could be observed in the sample.

Intrusion occurred in all three sessile drop experiments, and in both of the carbon lining substrates (with larger anthracite grains and without larger anthracite grains), the intrusion of silicon primarily affected the binder phase. In the anthracite substrate, silicon intruded into cracks in the grain, almost through the entire substrate.

Table 5.2 gives an overview of all of the samples, where the furnace type, binder phase, temperature profile and location of intrusion has been given for each sample. The samples are listed in order from most intruded to least intruded, after a rough calculation of area of intrusion vs total area of the sample.

No significant trend was observed on how the choice of binder phase influences the degree of intrusion, and intrusion was observed to different extents in all three binder types. Experiments where the type of binder is the only changing factor (i.e. layer thickness, temperature profile and furnace type should be the same for all samples) would have to be conducted to investigate this. The results in this report does not give a sufficient basis to conclude on binder type influence, and from these results it would seem that furnace choice and temperature profile are the main influencing factors when it comes to intrusion.

Table 5.2: Sample overview with furnace type, binder phase, temperature profile and location of intrusion. The samples are listed in decreasing order of intrusion.

Sample no.	Binder phase	T profile	Intrusion
*V*4	Tar pitch	Cycled $<$ 1416°C	Binder phase
Binder	Tar pitch	1480°C	Binder phase
Paste	Tar pitch	1450°C	Binder phase
*V*8	Resin	Cycled $<$ 1416°C	Binder phase
*V*7	Eco	Cycled $>$ 1416°C	Voids
*V*6	Eco	Cycled $>$ 1416°C	Voids
Anthracite	-	1480°C	Cracks
*FS*4	Tar pitch	1500°C, 45 min	No intrusion
*FS*5	Tar pitch	1500°C, 60 min	No intrusion
*FS*6	Tar pitch	1500°C, 60 min	No intrusion
*FS*7	Tar pitch	1500°C, 60 min	No intrusion
*V*5	Tar pitch	Cycled $>$ 1416°C	No intrusion

5.2.2 Chemical wear

Chemical reactions between the carbon lining and liquids or gases in the furnace were observed in all samples except two, sample FS7 and sample FS5. The formation of the oxide deposit on sample FS5 will not be discussed further in this section. Two different types of reactions were found; reaction with silicon producing SiC, and reaction with SiO(g) producing SiC. These two reactions were given in section 2.4.1 in the Theory chapter as equation 2.15 and 2.16:

$$\mathrm{SiO(g) + 2C(s) = SiC(s) + CO(g)} \tag{2.15}$$

$$\mathrm{Si(l) + C(s) = SiC(s)} \tag{2.16}$$

It is noted that both of the reactions are reactions of conversion, and not consumption.

In the two samples cycled around the solidification temperature of silicon, sample V4 and V8, the intrusion of silicon had led to transformation of the carbon lining to silicon carbide. This was observed both in the CT images and by inspecting the samples in EPMA. Figure 5.10 shows the intrusion into sample V4 in a CT cross section image as well as in a backscattered electron image obtained in the EPMA.

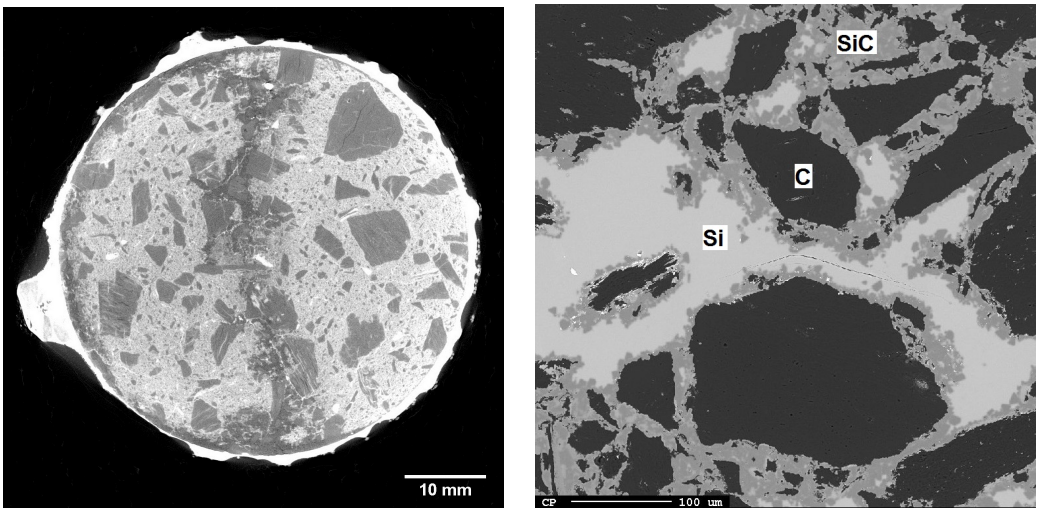

(a) CT **(b)** EPMA

Figure 5.10: Images of conversion in sample V4.

By X-ray photon analysis, it was confirmed that the product of this conversion reaction between intruded liquid silicon and solid carbon lining was silicon carbide. This reaction had turned almost all the binder phase in the intruded areas to SiC, and in the most affected areas, the anthracite grains had started to transform to SiC as well. It is noted that significant amounts of unreacted silicon was found in the sample interior as well, increasing the risk for spalling.

The same reaction between silicon and carbon from the lining had occurred in the sessile drop substrates. In the two substrates containing binder phase, the binder phase was the primary conversion reactant, while the anthracite grains looked mostly unaffected. In the anthracite substrate, reaction had occurred in the interface between silicon and anthracite as a topochemical conversion of the anthracite grains. The reaction in the anthracite substrate had occurred in much lesser extent than in the two other substrates. This confirms again that liquid silicon first and foremost attacks the binder phase and not the anthracite grains, as was observed by Tangstad in her studies with silicon on carbon linings [38]. Figure 5.11 shows backscattered electron images of the carbon lining paste substrate and the anthracite substrate, where the conversion product in both of the substrates is silicon carbide.

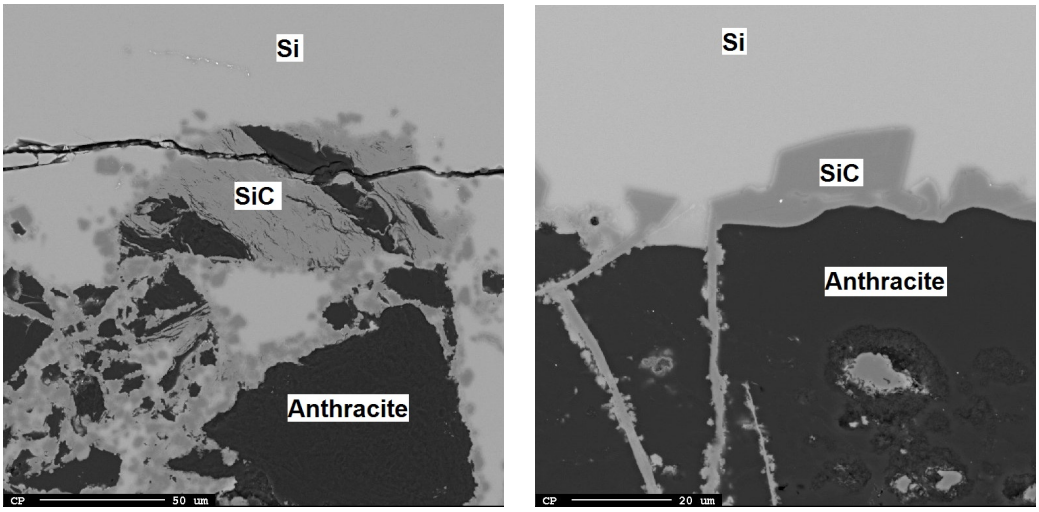

(a) Carbon lining sample **(b)** Anthracite

Figure 5.11: Conversion in carbon lining substrate and anthracite substrate.

In the section of the surface of sample V6 that was inspected using the EPMA, it was noted that the sample had been surrounded by slag. It was also observed that no reaction seemed to have occurred where the slag was present, and that no slag was found further than 0.6 mm into the sample. Further in than this, the sample contained only SiC apart from the original carbon lining. It is assumed that the reaction transforming carbon lining to SiC in sample V6 was due to intruded silicon, the added fine fractions of silicon or possibly SiO(g), not intruded slag.

In sample V7, exposed only to silicon, it was observed that SiC had formed along the interface between intruded silicon and the carbon lining, and that the anthracite grains looked unaffected by the silicon. It was also observed that SiC had formed inside the lining, and that this SiC looks slightly different from the very solid SiC found at the interface between silicon and the lining. Figure 5.12 shows conversion in a crack in sample V7, where silicon carbide can be found both at the interface (blue circle) and inside the lining (red circle). The SiC found inside the lining, in the red circle, could either have formed from the added silicon fines, or from reaction with intruded SiO(g).

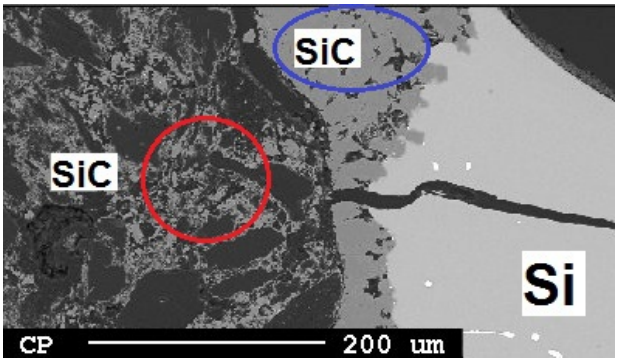

Figure 5.12: Backscattered electron image of conversion in sample V7.

In sample V5, FS4, and FS6, no intruded silicon or slag was observed, but conversion of the lining to silicon carbide could be observed in all these samples. Due to the lack of liquid intrusion, it is assumed that the conversion of the lining in these samples has been caused by SiO(g). It was noted that the SiC formed in these samples formed in scattered specks, similar to the SiC formed inside the lining of sample V7 in figure 5.12 (red circle) which was assumed to be formed either by the added silicon fines or by SiO(g). The structure of the silicon carbide formed scattered in the lining seemed different than that of the SiC formed in the interface between intruded silicon and the carbon lining as in V4, V6, V7 (blue circle figure 5.12), V8 and the sessile drop samples, which was more solid. This supports the assumption that the two silicon carbides have been formed by different reactions. Examples of the two different SiC appearances are given in figure 5.13a from sample FS4 and 5.13b from the sessile drop experiment with silicon on anthracite, respectively.

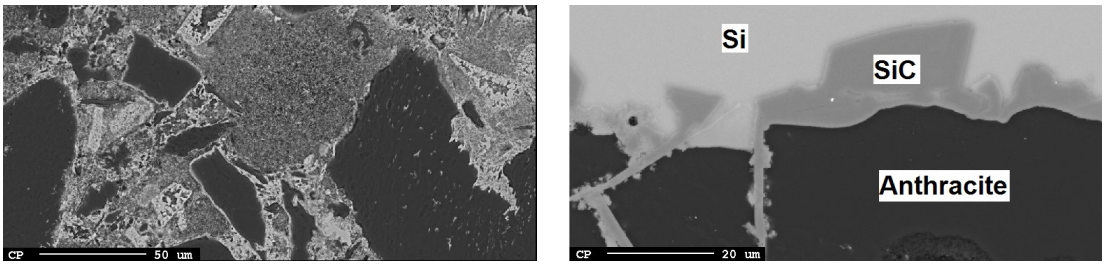

(a) FS4 **(b)** Anthracite substrate

Figure 5.13: SiC formed in sample FS4 and the anthracite substrate.

5.2.3 Spalling

As mentioned in the Theory chapter, section 2.4.4, two types of spalling can occur; spalling due to thermal stresses or spalling due to intrusion of silicon [3].

In the samples with heavy intrusion, it was difficult to determine whether the intrusion had led no any expansion of cracks or voids that could potentially lead to spalling. It is, however, noted that both sample V4 and sample V8 contained large amounts of unreacted silicon. Allthough no visible cracking of the samples was observed due to this intruded silicon, spalling might have occurred if the silicon had been allowed to solidify and melt several times, or if the duration of the experiment had been longer.

In the less intruded samples, V6 and V7, it was observed that some crack expansion had occurred, but due to the narrow width of the cracks in these samples, this crack expansion looked far from critical. The intrusion into the cracks in these samples had probably been more critical if the cracks had been wider to begin with, allowing more silicon to intrude.

When inspecting the sample surfaces using EPMA, it was noted that in all the samples where slag surrounded the surface, strings and pieces of SiC could be found in the slag. This was also observed by Steenkamp in her experimental work [3], where converted pieces of the lining were separated from the rest of the lining and found in the slag. This indicates that the chemical reactions transforming the lining to SiC, which was found in the EPMA investigations, might be critical for lining performance, as the lining thickness would decrease. Figure 5.14 shows an example of SiC in the slag, from the surface of sample V4.

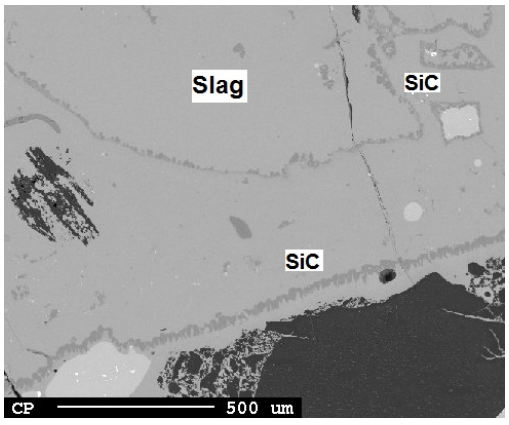

Figure 5.14: SiC in the slag around the sample surface of sample V4.

One explanation of this SiC spalling is that the slag tears the silicon carbide from the lining, where it collects in threads and pieces. Another explanation might be that the spalling of SiC is caused by the furnace forces. In the experimental work, SiC threads in the slag only occurred in the samples exposed to silicon and slag in the induction furnace, as the slag in the Entech furnace still remained mostly lumpy and unmelted. The experimental work performed by Steenkamp was also performed in an induction furnace. As two different compounds in an induction heated furnace is heated to different extents, thermal stresses might have occurred between the carbon lining and the formed SiC, which might have been the cause of the observed spalling of SiC.

5.3 Evaluation of experimental setup

The experimental work was performed in three different furnaces; an induction furnace (IF-75), an electric resistance heated furnace (Entech) and a sessile drop furnace. Each of these furnaces proved to have both advantages and disadvantages in the experiments with silicon and slag.

The induction furnace provides fast heating rates and high maximum temperatures in the furnace. In the experiments performed using the induction furnace, all of the silicon and slag was completely melted, except small areas with crusts in the transition between silicon/slag and air. This gave good wetting in all of the experiments conducted the induction furnace, and intrusion into several of the samples. However, the induction furnace proved to have one major disadvantage. To heat the furnace content, the induction furnace creates eddy currents and induction forces in the furnace content itself, as explained in section 2.7.1, which could prevent intrusion of silicon into the carbon lining.

In the preliminary project work, where no intrusion occurred in any of the samples, it was speculated that induction forces could be the reason for the lack of intrusion. The experiments performed in the experimental work for this thesis supports this assumption, as intrusion only occurred in experiments where the furnace power was switched off for longer periods of time (as the furnace temperature was cycled). It is also noted that more intrusion occurred in the samples that were cycled over bigger temperature intervals, where the furnace power has been off for even longer. This supports the assumption that the induction forces influence the intrusion, but it has to be noted that the solidification of silicon might have influenced these results.

Figure 5.15 shows cross section scans from three different experiments; sample FS7 was held at 1500°C and was not subjected to temperature cycling, sample V7 was cycled between 1600°C and 1450°C (150°C interval) and sample V4 was cycled between 1600°C and 1350°C (250°C interval). It was observed that no intrusion occurred in sample FS7, while sample V4 experienced the heaviest intrusion.

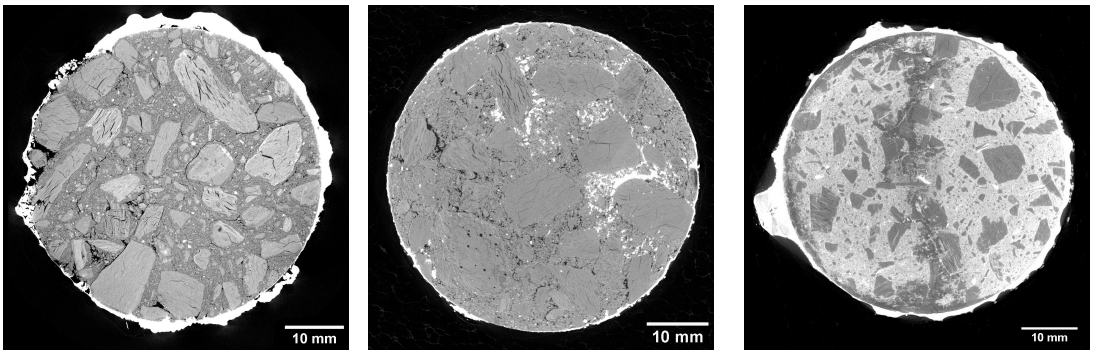

(a) Sample FS7 **(b)** Sample V7 **(c)** Sample V4

Figure 5.15: Difference in intrusion of sample FS7, sample V7 and sample V4.

The Entech resistance heated furnace heats the furnace content without inducing any forces in the furnace, or by otherwise impacting the furnace content in any other way than supplying heat through conduction and convection. This advantage makes it preferable to the induction furnace in experiments investigating intrusion. However, a number of problems were encountered using the Entech furnace and most of these were related to the amount of oxygen present and the slow heating rate.

Oxidation of silicon occurs quite easily [26], and oxidation of the silicon was observed in all of the Entech experiments. Figure 5.16 was presented in the Theory chapter, and shows at which temperatures and oxygen partial pressures silicon oxidates passively (to SiO_2(s)) and actively (to SiO(g)). The maximum temperature (1500°C) in the Entech furnace has been marked with a red line, and the relevant temperature area for the experiments conducted in the Entech furnace is on the left hand side of this line.

Figure 5.16 shows that both passive and active oxidation could occur in the temperature range of the experiments, and that below 1000°C, passive oxidation dominates for all oxygen partial pressures. When silicon oxidates passively, a layer of SiO_2(s) forms on the surface, and could prevent melting of the silicon.

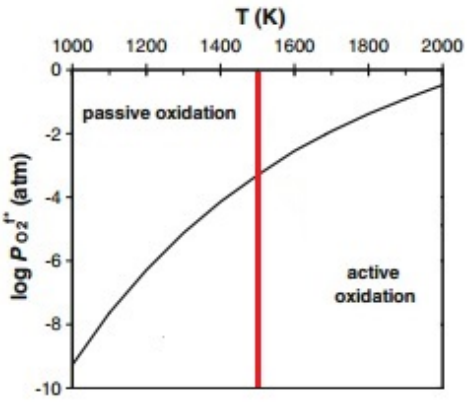

Figure 5.16: The domains of active and passive oxidation of silicon at different oxygen partial pressures and temperatures, after Drevet and Eustathopoulos [26]. P_{O_2} is the partial pressure of oxygen in the furnace, T is the temperature in the furnace.

As shown in the Experimental chapter, the heating rate of the Entech furnace was quite fast up to approximately 1000°C, before it slowed significantly until reaching approximately 1450°C. After reaching this temperature, the heating rate fell below 1°C/min, and only one of the three experiments performed in the Entech furnace reached the goal temperature of 1500°C. When comparing the heating rate with that obtained in the induction furnace, as shown in figure 3.10 in section 3.2.2, it was observed that the silicon in the induction furnace melted in approximately 36 minutes while the silicon in the resistance furnace used 112 minutes, more than three times longer. This gave the silicon significantly more time to oxidate in the Entech furnace compared with the induction furnace, and it is concluded that the Entech furnace was unsuited for melting silicon without any shielding gas.

The sessile drop furnace would, in theory, be the best furnace for investigations of intrusion of silicon into carbon linings. In this furnace, rapid heating rates are obtained without the interfering induction forces, and intrusion was observed in all experiments performed in this furnace. However, the sessile drop furnace has several disadvantages making the experiments performed in this furnace uncomparable with industrial conditions. The exeriments in this furnace were all performed using argon as the shielding gas, and the study performed by Tangstad [38] showed that the intrusion depth was influenced by the choice of shielding gas. It would be impossible to recreate the gaseous environment of a silicon furnace (SiO and CO [11]) in a sessile drop furnace, and any other shielding gas would give different results. Another disadvantage with the sessile drop furnace is that only small carbon lining samples can be investigated. As the substrates has to be cut very

thin, they have to be polished to prevent the silicon from running straight through cracks in the substrate. This creates a surface which cannot be directly compared with industrial linings.

One of the motivations behind the addition of slag in the experiments was to prevent oxidation of silicon. In the Entech furnace experiments, it was observed that this attempt was futile, as the silicon was oxidized even after the addition of slag on top of the silicon. In the induction furnace, the heating rate proved to be so fast that the addition of slag to prevent oxidation was unnecessary.

The other reason for adding slag was to investigate intrusion of, and reaction with, slags as well as silicon. In the experiments, it was observed that slag hardly intruded into the samples, and that no direct reaction between the slag and the lining seemed to occur. Sample V8 even showed that slag most likely prevented intrusion of silicon into the sample. It was observed that spalling of formed SiC occurred in the slag, which could be detrimental for the lining performance. It was observed that the slag composition varied, and that it did not completely match the original slag composition. There is a chance that intrusion of slag into carbon linings depends on the composition of the slag, and that other slags could have intruded into the lining.

The methods chosen to analyze the carbon lining wear in this thesis were CT and EPMA. The advantage of using CT was that it allowed inspection of the sample interior without destroying the sample, giving the opportunity to compare pristine and silicon exposed samples. It proved useful for investigation of density variations, grain crushing, crack formation, intrusion and, to a certain extent, conversion of the lining. The disadvantages of CT were that the chosen resolution of the images made it impossible to investigate sample areas smaller than approximately 1 mm. In several of the samples that were defined as unreacted after CT investigation, investigations using EPMA showed intrusion and conversion in the outer 500-600 μm of the sample. If CT had been the only method of investigation, this would not have been possible to determine. This might have been the case for several of the experiments in the preliminary project work, as none of these samples were further investigated using EPMA. It is noted that the resolution of the CT images can be improved by longer scan times or by using smaller samples. Another disadvantage with the CT is that it cannot with certainty perform qualitative analyses of different phases in a sample. It is theoretically possible to measure the density of a phase using the CT and compare the obtained value with litterature values to determine the composition, but this could be very inaccurate.

One of the advantages of using EPMA as a tool for lining wear investigation is that it can show areas of a sample in very high magnifications, which made it possible to find reactions in nearly all of the samples. It is also a major advantage to be able to use the characteristic X-ray photons to perform qualitative analyses, and when using the X-ray photons for mapping, it gives a good idea of the amount of an element in a specific area as well. One disadvantage of using EPMA was that the EPMA only allow surface inspection, and when using larger samples such as in this experimental work, that makes EPMA a destructive test method. Another disavantage is that the sample size is quite small, which would make it very time consuming to investigate an entire sample of the size of the samples used in this thesis.

Using CT and EPMA together gave very good results; the CT was used to find points of interest in the samples, and the EPMA was used to investigate these areas more closely and perform qualitative analyses.

Chapter 6

Conclusions and suggested further work

6.1 Conclusions

In this thesis, carbon lining samples were made using different binders and different installation techniques giving different internal structures. The samples made with a layered structure had uniform density in the cross sections, but showed variations in the average cross section densities dependent on position relative to the layers. Density measurements showed that the top of each ramming layer had increased density, while the bottom of each layer was less dense i.e. less packed together by the ramming. With increasing layer thickness, the density variation across the height of the sample increased. No such density variations were observed in the solid, unlayered samples. It was also observed that different installation tools influenced the degree of grain crushing, and that a flat ramming tool gave the least amount of grain crushing. The amount of cracks in the samples was influenced by the choice of binder phase, and the tar pitch binder samples had significantly more cracks than the resin samples and the eco binder samples.

The samples were subjected to silicon and slag using an induction furnace, a resistance heated furnace and a sessile drop furnace. In the resistance heated furnace, wetting and intrusion were prevented by oxidation of silicon, and no intrusion was observed in these samples. Intrusion was observed in samples from both the induction furnace and the sessile drop furnace.

Three temperature profiles were used for the experiments in the induction furnace, and they all gave different degrees of intrusion. One sample was heated to 1500°C and held at this temperature for 60 minutes, which gave no intrusion into the sample. Moderate intrusion was observed in the samples cycled above the solidification temperature of silicon, while heavy intrusion was observed in the samples

cycled around the solidification temperature of silicon. From this it was concluded that the temperature cycling was a necessary prerequisite for intrusion in induction furnace experiments. It was also observed that only silicon intruded into the center of the samples, while slag had a maximum intrusion depth of 0.6 mm.

It was observed that the installation technique had influenced the intrusion of silicon, as the intrusion first occurred in the porous layer bottoms. With sufficient amounts of intrusion, the binder phase was almost entirely transformed to silicon carbide or replaced by silcon while the anthracite grains were affected slightly less. The experiments in the sessile drop furnace showed that intrusion occurs mainly in the binder phase, but also as a topo chemical reaction on anthracite grains. As grain crushing would increase the surface area, it would lead to increased intrusion and increased amounts of conversion of the anthracite grains in the lining.

In addition to the conversion reaction caused by intrusion of silicon, it was observed that reaction also occurred due to the presence of SiO(g) in the furnace, converting the carbon lining to silicon carbide. This reaction accounts for the observed conversion in the samples without intrusion, and occurred near the surface or in the vicinity of cracks.

The intrusion also caused some expansion of the pre-existing cracks in the surface, which might lead to spalling. The cracks found in the samples in this experimental work were quite narrow, which limits the amount of intruded silicon and thus the potential for detrimental crack expansion and spalling. It was also observed that spalls of silicon carbide which had been formed from the carbide lining was found in the slag, completely detached from the lining. This could become detrimental for the lining.

6.2 Further work

Due to the vast range of the topic investigated in this work, there are several possible extensions of this thesis. The main objective of this thesis was to investigate the mechanisms of wear of carbon linings, and how these are influenced by installation technique, furnace content, temperature cycling and choice of furnace. The experiments were conducted in three different furnaces, with different temperature profiles and atmospheres. Many limitations were related to the experimental setup and choice of furnace.

First and foremost, it would be necessary to optimize the experimental setup in

terms of choice of furnace, atmosphere and temperature profile. The goal would be to keep the parameters as close to the industrial conditions as possible, and still keep the experiments small scale to allow CT investigation of the carbon lining samples before and after experiments. As previous experiments performed by Tangstad [38] showed that the choice of atmosphere influenced the degree of intrusion of silicon into carbon linings, it would be optimal to perform the experiments without shielding gas but in a relatively closed environment, allowing CO(g) and SiO(g) to form the gaseous environment. From this work it is also recommended to avoid the use of induction furnaces, as the induction forces seem to influence the intrusion into the lining. Temperature cycling gave the most extreme results in this work, and the lining in submerged arc furnaces does experience temperature variations during its lifetime. Further investigation of how the maximum temperature and temperature cycles influence lining wear should be conducted.

Four main mechanisms of wear was presented in this report: erosion, densification, chemical wear and spalling. Due to the stationary setup in the experimental work, erosion wear was not possible to inspect in this work. To include erosion investigation, future experiments could include rotation of the sample.

In this report, linings with three different types of binder were investigated, and different installation techniques and tools were tested on these pastes. It was determined that the choice of binder phase, installation technique and ramming tool affected the internal sample morphology, and further investigations on this topic could be performed. In this report, only carbon tamping pastes were investigated, but it would be possible to extend the range to prebaked blocks as well. As the focus on PAH free binders has increased, it would be very relevant to continue investigations of the eco binder.

The use of X-ray computed tomography (CT) as an investigation tool proved very useful, both when investigating the lining wear and especially when investigating the internal morphology of the carbon lining samples. For any further work concerning both the morphology and wear of carbon linings, this would be a recommended investigation method.

References

[1] Roskill. Silicon and ferrosilicon: Global industry markets and outlook. *14th edition*, 2014.

[2] SNE research. Metallugical grade-silicon (mg-si) manufacturing technique. `http://www.sneresearch.com/eng/info/show.php?c_id=3808`, 2012.

[3] Joalet Dalene Steenkamp. *Chemical wear of carbon-based refractory materials in a silicomanganese furnace tap-hole.* PhD thesis, University of Pretoria, 2014.

[4] Pieter Lamont. Carbon and graphite refractory lining system for submerged arc furnaces. Report, UCAR South Africa, 2004.

[5] Sofie Aursjø. Wear of carbon refractory materials in silicon furnaces. *NTNU*, 2015.

[6] Anders Schei, Johan K. Tuset, and Halvard Tveit. *Production of High Silicon Alloys.* Tapir forlag, Trondheim, 1998.

[7] R.I Scace and G.A Slack. *Silicon Carbide - A High Temperature Semiconductor.* Eds. O'Connor Press, London, 1960.

[8] V. M. Glazov and O. D. Shchelikov. Volume changes during melting and heating of silicon and germanium melts. *Thermophysical Properties of Materials*, 2000.

[9] Merete Tangstad. *Metal production in Norway.* Akademika publishing, Trondheim, Norway, 2013.

[10] Tom Miles. The boudouard equation. `http://www.gasifiers.bioenergylists.org/Boudouard_Equilibrium`, 2006.

[11] Sarina Bao, Merete Tangstad, Kai Tang, and Eli Ringdalen. Production of sio gas in the silicon process. *The thirteenth International Ferroalloys Congress*, 2013.

[12] D. Lynch. Winning the global race for solar silicon. *Journal of Materials Science*, 61:41–48, 2009.

[13] Merete Tangstad, Michal Ksiazek, and Jan Erlend Andersen. Zones and materials in the Si furnace. *Silicon for the Chemical and Solar Industry, XII*, 2014.

[14] P. Hloben. *Refractory Materials- Major Industrial Applications.* Rexxon, South Africa, 2000.

[15] P.L. Duncanson and J.D. Toth. The truths and myths of freeze lining technology for submerged arc furnaces. *Practical refractories*, pages 488–499, 2004.

[16] Hogne Linga and Ivar Skogland. *Fremstilling av karbonmaterialer.* Elektrokjemisk industri, Fagkurs, 1985.

[17] Morten Sørlie. Manufactured carbons - raw materials. Presentation, Elkem Aluminium AS.

[18] Morten Sørlie. Formulation and mixing. Presentation, Elkem Aluminium AS.

[19] Håvard Mølnås. Compability study of carbon-based refractory materials utilized in silicomanganese production furnaces. *NTNU*, 2011.

[20] Igor L. Shabalin. *Ultra-High Temperature Materials I.* Springer, New York, 2014.

[21] J.M. Neff. *Polycyclic aromatic hydrocarbons in the aquatic environment : sources, fates and biological effects.* Applied Science Publishers, 1979.

[22] D. Schulze. *Powders and Bulk Solids.* Springer, New York, 2008.

[23] Encyclopaedia Britannica. Fermi level. `http://academic.eb.com/EBchecked/topic/204779/Fermi-level`, 2016.

[24] M. Krokstad. Elektrisk resistivitet i industrielle SiC-lag. *NTNU*, 2014.

[25] Mari K. Næss. Active oxidation of liquid silicon: Experimental investigation of kinetics. *Oxidation of Metals, Issue 5*, pages 363–376, 2012.

[26] Beatrice Drevet and Nicolas Eustrathopoulos. Wetting of ceramics by molten silicon and silicon alloys: a review. *Journal of Materials Science, HTC 2012*, 47:8247–8260, 2012.

[27] Allibert et al. *Slag Atlas*. Stahleisen GmbH, 1995.

[28] Greiner L. Kammel R. Winterhager, H. *Forschungsberichte des Landes Nordrhein-Westfalen*. Westdeutscher Verlag, 1966.

[29] Thomas A. G. Barrett, L. R. *Glass Technol. 43*. 1959.

[30] T. Rosenqvist. *Prinsiples of extractive metallurgy, 2nd edition*. Tapir academic press, Trondheim, 2004.

[31] Mineralogical society of America. Mohs' scale of hardness. `http://www.minsocam.org/MSA/collectors_corner/article/mohs.htm`, 2014.

[32] American Federation of Mineralogical Societies. Mohs' scale of mineral hardness. `http://www.amfed.org/t_mohs.htm`.

[33] Wikipedia. Mohs' scale of mineral hardness. `http://en.wikipedia.org/wiki/Mohs_scale_of_mineral_hardness`, 2015.

[34] Encyclopaedia Britannica. Graphite. `http://academic.eb.com/EBchecked/topic/242042/graphite`, 2016.

[35] Encyclopaedia Britannica. Anthracite. `http://academic.eb.com/EBchecked/topic/27447/anthracite`, 2016.

[36] Jafar Safarian and Merete Tangstad. Wettability of silicon carbide by CaO-SiO_2 slags. 2009.

[37] Arjan Ciftja. *Solar silicon refining; Inclusion, settling, filtration, wetting*. PhD thesis, NTNU, 2009.

[38] Merete Tangstad. Intrusion of silicon and SiO_2 in three carbon lining materials. Presentation, NTNU/SINTEF, 2014.

[39] V. L. Yupko. The wetting of self-bonded polycrystalline silicon carbide by silicon. *Powder Metallurgy and Metal Ceramics*, 16:777–780, 1977.

[40] Jian Guo Li and Hans Hausner. Wetting and infiltration of graphite materials by molten silicon. *Scripta Metallurgica et Materiala*, 8:377–382, 1995.

[41] O. Malliart, V. Chaumat, and F. Hodaj. Wetting and interfacial interactions in the CaO–Al_2O_3–SiO_2/silicon carbide system. *Journal of Materials Science*, 2010.

[42] Stead Fast Engineers Pvt Ltd. Presentation on electric induction furnace by stead fast engineers pvt ltd. `https://www.youtube.com/watch?v=o1F9ojuawX4`, 2015.

[43] Encyclopaedia Britannica. Faraday's law of induction. `http://academic.eb.com/EBchecked/topic/201744/Faradays-law-of-induction`, 2016.

[44] McGraw-Hill Dictionary of Scientific and Technical Terms 6E. Resistance furnace. `http://encyclopedia2.thefreedictionary.com/Resistance+Furnace`, 2003.

[45] Rachel A. Powsner, Matthew R. Palmer, and Edward R Powsner. *Essentials of Nuclear Medicine Physics and Instrumentation (3rd Edition)*. John Wiley and Sons, 2013.

[46] Greg Michael. X-ray computed tomography. *Physiscs Education*, 2001.

[47] Donald Picard. Characterization of pre-baked carbon anode samples using X-ray computed tomography and porosity estimation. *Light metals 2012, TMS*, pages 1283–1288, 2012.

[48] J. Hjelen. *Scanning elektron-mikroskopi*. SINTEF Avdeling for metallurgi, Metallurgisk institutt NTH, 1986.

[49] JEOL. Electron probe micro analyzer. `http://www.jeol.co.jp/en/science/epma.html`, 2013.

Appendix A

Temperature profiles

Figure A.1 shows the temperature logs from experiments with sample V5, V6 and V7.

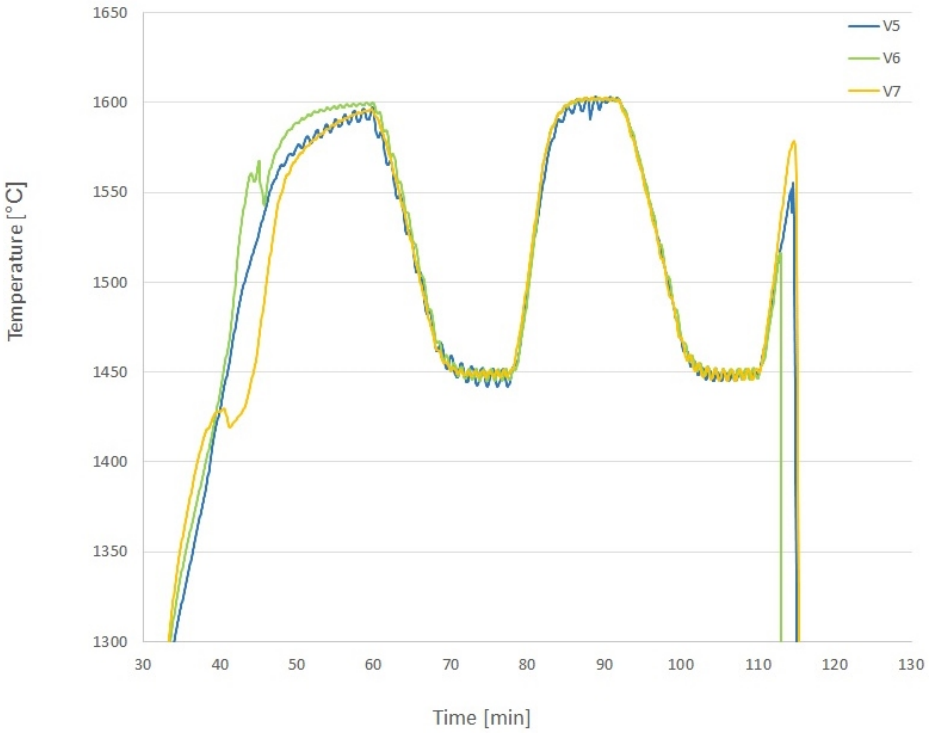

Figure A.1: Individual temperature logs from experiments with sample V5, V6 and V7.

Appendix B

EPMA analysis

The following appendix contains the point analyses performed on samples from all three furnaces. The analyses performed on the slags will be given in weight percent, wt%, to make comparison with the orgiginal slag composition (given in wt%) easier. All other analyses will be given in atomic percent, at%.

The analyses will be given in the order they appear in the report.

B.1 Induction furnace samples

B.1.1 Sample FS7

Table B.1 shows the analysis of the slag surrounding sample FS7. Three sets of analyzes were performed in the same area, and table B.1 shows every analysis separately as well as the average values of all three.

Table B.1: Analysis of slag surrounding sample FS7.

Element	An. 1 [wt%]	An. 2 [wt%]	An. 3 [wt%]	Ave. [wt%]
Al	8.033	8.083	8.119	8.078
O	39.849	40.034	40.006	39.963
Ca	17.729	18.012	18.25	17.997
C	2.651	2.753	2.679	2.694
Fe	0	0	0.016	0.005
Si	26.149	26.753	26.597	26.500

B.1.2 Sample V4

Table B.2 shows the analysis of the slag surrounding sample V4 in figure 4.31a. Three sets of analyzes were performed in the same area, and table B.2 shows every analysis separately as well as the average values of all three.

Table B.2: Analysis of slag surrounding sample V4 in figure 4.31a.

Element	An. 1 [wt%]	An. 2 [wt%]	An. 3 [wt%]	Ave. [wt%]
Al	8.119	8.585	7.605	8.103
O	25.526	27.368	23.936	25.61
Ca	10.864	11.659	10.659	11.061
C	8.728	6.751	9.286	8.255
Fe	0.03	0.01	0.021	0.002
Si	38.132	37.161	41.99	39.094

Table B.3 shows the analysis of the slag surrounding sample V4 in figure 4.31b. Three sets of analyzes were performed in the same area, and table B.3 shows every analysis separately as well as the average values of all three.

Table B.3: Analysis of slag surrounding sample V4 in figure 4.31b.

Element	An. 1 [wt%]	An. 2 [wt%]	An. 3 [wt%]	Ave. [wt%]
Al	9.349	10.818	8.495	9.554
O	37.265	36.86	35.633	36.586
Ca	16.014	15.884	15.39	15.763
C	3.899	3.666	5.858	4.474
Fe	0.015	0	0	0.005
Si	27.548	26.216	32.56	28.775

B.1.3 Sample V5

Table B.4 shows the analysis of the transformed area in figure 4.40a (point of analysis circled in red).

Table B.5 shows the analysis of the transformed area in figure 4.40b (point of analysis circled in red).

Table B.4: Analysis of transformed area in sample V5, highlighted in figure 4.40a.

Element	Analysis results [at%]
Al	6.1933
O	0.3036
Ca	0.0
C	46.4202
Fe	0.0413
Si	47.0416

Table B.5: Analysis of transformed area in sample V5, highlighted in figure 4.40b.

Element	Analysis results [at%]
Al	10.5974
O	11.1715
Ca	0.0066
C	37.0631
Fe	0.5767
Si	40.5847

B.1.4 Sample V6

Table B.6 shows the analysis of the transformed area in figure 4.49a (point of analysis circled in red).

Table B.6: Analysis of transformed area in sample V6, highlighted in figure 4.49a.

Element	Analysis results [at%]
Al	0.0172
O	0.0016
Ca	0.0066
C	51.1891
Fe	0.007
Si	48.4854

B.1.5 Sample V7

Table B.7 shows the analysis of the area circled in blue in figure 4.56, while table B.8 shows the analysis of the area circled in red in the same figure.

Table B.7: Analysis of transformed area in sample V7 circled in blue in figure 4.56.

Element	Analysis results [at%]
Al	0.5343
O	0.1604
Ca	0.0
C	48.1473
Fe	0.0017
Si	51.1563

Table B.8: Analysis of bright area in sample V7 circled in red in figure 4.56.

Element	Analysis results [at%]
Al	0.0
O	0.3532
Ca	0.0
C	10.8112
Fe	0.0132
Si	88.8181

B.2 Entech furnace experiments

Table B.9 shows the analysis of the layer surrounding the anthracite grains in sample FS4.

Table B.9: Overview of experiments performed in Entech resistance heated furnace

Element	Analysis results [at%]
Al	0.1029
O	1.7081
Ca	0.0086
C	54.2099
Fe	0.0058
Si	43.9646

B.3 Sessile drop experiments

B.3.1 Anthracite substrate

Analyses were performed on the SiC grains on the surface of the anthracite substrate, as well as in the formed SiC in the grain cracks, and of the silicon used as the sessile drop. Table B.10 shows the analysis of the SiC on the surface, while table B.11 shows the analysis of the SiC inside the grain cracks. Table B.12 shows the analysis of the silicon, which is the same silicon used for all the experiments in all three furnaces.

Table B.10: Analysis of SiC on surface of anthracite substrate.

Element	Analysis results [at%]
Al	0.0492
O	0.1607
Ca	0.0068
C	49.4724
Fe	0.0014
Si	50.3095

Table B.11: Analysis of SiC inside cracks in anthracite substrate.

Element	Analysis results [at%]
Al	0.0
O	0.3243
Ca	0.0
C	27.3646
Fe	0.0106
Si	72.3005

Table B.12: Analysis of silicon used in sessile drop experiments

Element	Analysis results [at%]
Al	0.0069
O	0.3765
Ca	0.0
C	12.5412
Fe	0.0072
Si	87.0681